Diffusion-Reaction-Models and their Application to Biological and Astrophysical Problems

I n a u g u r a l - D i s s e r t a t i o n

zur

Erlangung des Doktorgrades

der Mathematisch-Naturwissenschaftlichen Fakultät

der Universität zu Köln

vorgelegt von

Andrea Wolff

aus Köln

2011

Berichterstatter: Prof. Dr. Joachim Krug
Prof. Dr. Johannes Berg

Tag der mündlichen Prüfung: 27.01.2012

Zusammenfassung

In der vorliegenden Arbeit werden verschiedene Anwendungen von Reaktions-Diffusions-Modellen untersucht. Im ersten Teil dieser Arbeit untersuchen wir den Einfluß von Robustheit auf die Fitness von Populationen. Robustheit ist hier im Sinne von Toleranz einer gewissen Menge schädlicher Mutationen ohne Verlust der Fitness aufzufassen. Dabei konzentrieren wir uns auf einfache Organismen bzw. effektive Systeme, die durch die deterministischen Quasispeziesmodelle beschrieben werden können. Wir leiten analytische Ausdrücke für die Fitness solcher Populationen im Grenzwert langer Informationssequenzen (z.B. DNA) der Individuen her. Insbesondere erlaubt der von uns gewählte Zugang die Herleitung von Korrekturtermen für kurze Sequenzlängen, die die Übereinstimmung zwischen numerischen und analytischen Ergebnissen stark verbessern. Dies ist für Anwendungen von besonderer Bedeutung. Weiterhin beantworten wir die Frage, unter welchen Bedingungen eine höhere Toleranz gegenüber schädlichen Mutationen zu einer höheren Fitness der gesamten Population führt als eine höhere Fitness weniger Sequenztypen. Alle analytischen Ergebnisse werden durch numerische Lösungen verifiziert.

Den zweiten Teil dieser Doktorarbeit bildet die systematische Untersuchung des Einflusses von Unordnung auf die Reaktionsraten von diffundierenden Teilchen auf zweidimensionalen Oberflächen. Unordnung bezieht sich hier auf die Verteilung von Bindungsenergien, mit denen die Reaktionspartner auf der Oberfläche gebunden werden. Als Beispiel dient die elementare Reaktion der Bildung molekularen Wasserstoffs aus atomarem Wasserstoff $H + H \rightarrow H_2$ auf interstellaren Oberflächen. Wir können in dieser Arbeit die zuvor aufgestellte Vermutung, dass Unordnung in den Bindungsenergien auf der Oberfläche die Reaktionsrate stark erhöht, bestätigen und quantitative analytische Ergebnisse für verschiedenste Verteilungen der Bindungsenergien präsentieren. Es stellt sich heraus, daß der Fall binärer Unordung (zwei verschiedene Bindungsenergien) fundamental ist. Alle anderen untersuchten Systeme mit beliebigen (normierbaren) diskreten und kontinuierlichen Bindungsenergieverteilungen lassen sich auf den binären Fall abbilden. Wir können diese Abbildungsvorschriften explizit angeben. Alle analytischen Ergebnisse werden durch numerische Lösungen und kinetische Monte-Carlo-Simulationen bestätigt.

Abstract

In this thesis we study several problems from biophysics and astrophysics, which can be all be described by reaction-diffusion systems.

The first part of this thesis is concerned with biophysical quasispecies models. These are deterministic models, describing the interaction of mutations and selection (i.e. fitness advantage by adaption). We investigate the influence of robustness against deleterious mutations on the stationary states of these models. Here, robustness means that a certain number of mutations in the individual's information string is tolerated before the fitness of the individual is diminished. The equations of state for the quasispecies models can be represented by a reaction-diffusion equation for a special type of reaction term. We give analytic results for the robustness effect on the mean fitness of a population. These results become exact in the limit of infinite information-sequence length. By exploiting a mapping to a Schrödinger-type equation, we find correction terms for finite sequence length, essential for applications. The provided solutions allow to answer the question under what circumstances robustness is preferable to fitness, a question often referred to as *survival of the flattest*. Additionally, we investigate the occurence of the error threshold (a phase transition of the population's state) in a general class of epistatic fitness landscapes. We show that diminishing epistasis is necessary but not sufficient for the emergence of an error threshold. All analytic work is supported and verified by numerical studies.

In the second part we investigate diffusion-mediated reactions on two-dimensional surfaces drawing on the example of hydrogen formation on interstellar dust grains. The surfaces of these dust grains play an important role in molecule production in the interstellar medium, by acting as catalysts. We are interested in the influence of (quenched) surface disorder on the production rate of molecules. As model system, we study the not yet completely understood reaction $H + H \rightarrow H_2$ of hydrogen formation. We confirm the earlier proposed significant enhancement in the production rate of this process by disorder in the binding energies of the surface and moreover give analytic results for different distributions of binding energies. We identify the main mechanism leading to an enhanced production rate, enabling us to give temperature dependent mappings from systems with discrete and continuous binding energy distributions to effective systems with only a binary energy distribution. The analytical results on all models are confirmed by numerical solutions of the full rate equations as well as by kinetic Monte Carlo simulations.

Contents

General Introduction

The following work is set in the context of statistical physics and its applications, namely reaction-diffusion systems. Diffusion as such is the most prominent and fundamental transport mechanism in many physical systems, starting from Brownian motion itself [31], over mixing of heterogeneous gases or liquids to osmosis and many other examples. Even for systems, where the particles do not diffuse in the microscopic sense, it is possible that the overall system's behavior can be described by a diffusion equation. A prominent example is heat conduction in solids. We speak of reaction-diffusion systems, if the particles do not only diffusive through the system, but are also interacting. This involves active reactions of the particles to events like e.g. meeting another particle or encountering a special surface site. Typical interactions considered are of contact type, like pair annihilation, particle creation, nucleus formation, etc. The nonlinear time evolution equation for some quantity $u(\mathbf{r}, t)$, e.g. particle concentration, depending on space and time is

$$\partial_t u(\mathbf{r}, t) = D\nabla^2 u(\mathbf{r}, t) + R(u(\mathbf{r}, t)), \tag{1}$$

as introduced by Kolmogorov, Petrovskii, Piskunov [54] and Fisher [34]. This is the simplest general description of a one-component reaction-diffusion system. D is the diffusion coefficient (which can also be space-dependent) and the function $R(u(\mathbf{r}, t))$ encapsulates the reaction(s).

The exact structure of the reaction term determines whether a (closed) analytical solution exists. Often slight changes in the reaction term structure lead to a completely altered system behavior. We will come across these characteristics especially in the second part of this thesis.

Typical reaction terms investigated are of linear, non-linear and catalytic type. Linear reaction terms can describe processes like a particle becoming immobile, particle creation and spontaneous annihilation. Whenever a reaction involves more than one particle, the reaction term is non-linear. Prominent examples are pair annihilation, recombination, or nucleus formation. In catalytic reactions the product is only formed in the presence of a catalyst which is not chemically changed during the reaction. We investigate systems with linear reactions terms in the first part and with non-linear (and implicitly catalytic) reaction terms in the second part of this work.

As turned out over the years, reaction-diffusion systems are useful models to describe very different phenomena known from physics, chemistry and biology [8, 21]. In this thesis, we investigate two applications, the first exhibits its reaction-diffusion character on the level of the effective model description, the second is truely reactive and diffusive on the (microscopic) particle level. Though the

investigation of the dynamical properties of the systems to be introduced would be highly interesting, we focus on the stationary state properties throughout, as even there fundamental questions have not been solved, yet.

Robustness in quasispecies models: Quasispecies models are famous in biophysics and can be used to describe large populations of simple organisms like viruses or bacteria. The issue of robustness against deleterious mutations has been risen recently [26, 55]. Amongst other things it is concerned with understanding under which conditions a high tolerance of mutations is preferable to a higher offspring production rate of a few very well adapted individuals regarding the survival of the population. This is often referred to as "survival of the flattest". In this work, we derive analytical expressions for the populations mean fitness in landscapes with one plateau or with two competing plateaus. These results enable us to appraise recent results [39, 86] and to extend the existing mean field model solutions by finite size correction terms, crucial for applying the model to real systems. Our results have been published in [88].

Formation of H_2 on interstellar surfaces: Drawing on the example of hydrogen formation on interstellar dust grains, we investigate the influence of disorder on diffusion-mediated reactions on two-dimensional surfaces . As the most abundant element in space, H and H_2 are involved in an immense number of reactions and reaction networks that lead to the formation of complex molecules. Nevertheless, the fundamental formation of H_2 via $H + H \rightarrow H_2$ has not been fully understood so far. Due to the low temperatures and pressures in space, this reaction is not efficient for two atoms meeting in three-dimensional space. It has been agreed on that the surfaces of dust grains in the interstellar medium act as catalysts and H_2 is formed on these surfaces. Inspired by former work, we investigate in this thesis the influence of disorder in the surface's binding energies on the reaction rate of molecule formation. We identify a uniform mechanism facilitating a high reaction rate even in temperature regions where a system without disorder performs poorly. This part is based on the publications [89, 90] and contains further efforts on general discrete binding energy distributions and multiple-species systems.

More details on the connection between the applications and the framework of reaction-diffusion systems will be given after the detailed introduction to each of the systems at the beginning of the corresponding part of this thesis.
For our investigations the following methods are employed:

analytical treatment: The stationary reaction-diffusion equations for both applications are analyzed with emphasis on simplified effective equations that capture the essence of the system's behavior,

numerical treatment: Additional to the (effective) analytic solutions we also employ direct numerical solutions of the full (stationary) system in both parts of this work,

kinetic Monte Carlo simulations: In the second part of this work we also use simulations that capture the microscopic processes in detail. These simulations serve as a reference for both the analytical models and the direct numerical solutions.

Part I

Robustness in deterministic mutation-selection models

Chapter 1

Introduction

The branch of population genetics, which tries to describe biological evolution in terms of natural selection, nowadays referred to as Neo-Darwinism or 'modern synthesis', was founded in the 1920's by Fisher, Haldane and Wright (see [33, 42, 91] and references therein).

Studies revealed the high complexity of molecular processes like reproduction or gene expression. The question is still not answered, which of the conceivable interplays between the elementary processes on the molecular level like for example genetic drift, mutations, selection or recombination, are the most important ones for the evolution of a whole species.

Theoretical models for evolution can - due to the complexity of the processes - typically capture only a few aspects found in the experiments. An important class of models are the ones assuming mutation and selection mechanisms to be the most essential ones. Even if these mechanisms are not as essential as assumed, they play an important role and thus worth studying them in detail. The elementary processes found in these models can probably be used as case studies for models concerned with other aspects of evolutionary processes. For reviews about this topic see [3] or [27].

Here, we will restrict ourselves to mutation-selection models for the artificial case of infinite population sizes, the quasispecies models. That means influences like drift (due to fluctuations caused by finite population size) are neglected, which in turn provides us with some powerful possibilities of solving the emerging equations for the population's state. The two famous models concerned with the influence of mutation and selection on large populations are the Crow-Kimura model established 1965, [53, 50], and the Eigen model, invented 1971, [30].

Models: The Crow-Kimura (CK) and the Eigen model present the principal ideas of how mutations and reproduction can interfere in asexual, haploid organisms and in the regime of very large ("infinite") populations. One possibility is that mutations occur steadily due to permanent influence of the environment, captured by the Crow-Kimura model, the other is that mutations occur only during reproduction as copying errors, as decribed by the Eigen model. For that reason the Crow-Kimura model is also known as parallel model and the Eigen model as coupled model. The two models are deterministic models in the sense of neglecting fluctuations due to finite population size. Therefore, the obtained results are only asymptotically correct for real populations. Furthermore, the

CK-model, being a continuous time model, can be derived from the discrete time Eigen model via straightforward continuum limit in time (to first order). Though invented for another purpose, it turned out, that the Eigen model is adequate to describe bacteria under strongly controlled environmental conditions. We will present this model together with the Crow-Kimura model in chapter 2. The Crow-Kimura model can be used to describe the evolution of virus populations, which is used in the development of drugs against viral diseases. For more details about the context of the Crow-Kimura model see e.g. [53, 50].

Fitness landscapes: The crucial additional ingredient needed in both models is the fitness landscape. It assigns to each information sequence (e.g. DNA or RNA sequence) the expected number of offspring an individual with this sequence produces. Thus it provides information on the selection. In principle, this fitness landscape has to be measured for real populations in fixed environments, but this is a highly complicated issue. Hence, different simple and more complex shapes of fitness landscapes have been proposed and investigated theoretically, starting with Eigens sharp-peak landscape [30], where only one sequence has a better fitness than all others. A theoretical analysis is, for example, concerned with the qualitative and quantitative shape of the equilibrium population distribution, occurring phase transitions between qualitative different distributions, scaling behavior for infinitely long sequences, etc. Some cases can be solved analytically, but for most of them, one has to rely on numerical methods. Examples of important landscapes are the mentioned sharp-peak landscape, the Fujiyama landscape, the plateau landscape, rugged fitness landscapes or epistatic landscapes. For a review about all mentioned landscapes see [51]. A discussion about how and to what extent these kinds of landscapes can be be inferred from experiments can be found in [85]. For several of these landscapes, experimental evidence exists [17, 10, 87, 15].

In this thesis, we are concerned with the class of epistatic fitness landscapes, especially with the most extreme variant, the plateau-shaped landscape. In the latter, a high fitness value is assigned to all sequences that differ from the best-adapted one only by a defined maximal number of sites. All other sequences have a very low fitness. A central question we adress is under which conditions and to what extend a broader plateau is preferable to a higher fitness value, regarding the mean fitness of the whole population. To answer this question it is first necessary to understand the fitness effect of one plateau on a quasispecies population.

Connection to the framework of reaction-diffusion models: To apply the general reaction-diffusion equation (1) to a specific problem, the reaction term has to be specified. Like Fisher and Kolmogorov applied the specific form of $R(u) = u(1-u)$ in (1) to describe gene spreading in a population, in [29] Ebeling et al. consider the class of reaction terms $R(u) = w(x,u)u(x,t)$ with arbitrary real function w. Their main application is a generalization of Fisher's classical population genetics model [33]. They show in detail that the generalized Fisher model can be regained from the reaction-diffusion equation (1) by their choice of the reaction term. Now, the Eigen model, whose continuous time version — the Crow-Kimura model — we study in this thesis, is the space-discretized version of Fisher's model. In this sense, the evolution models investigated here, belong to the great class of phenomena that can be described by reaction-diffusion models. In particular, Ebeling et al. derive a Schrödinger type equation for the time behavior of their system's solution (eq. (3.5) in [29]),

which is of exactly the same shape as equations (3.7) and (3.11) we provide in chapter 3 for the mean fitness of the population.

Outline

In the first section of chapter 2 we start with the explanation of the basic biological concepts and continue in section 2.2 with the definition of the Eigen and the Crow-Kimura model. Having understood the basic principles, we introduce and exemplify the notion of fitness landscapes in section 2.3 and specify the term of the error threshold in section 2.4. Equipped with this knowledge, we review a popular method of solving the dynamical equations of the Eigen model and the Crow-Kimura model for the equilibrium state, in the limit of infinite sequences, called maximum principle, in section 2.5. The knowledge presented in the whole chapter 2 is well known in the field and provides the background for our analysis starting in chapter 3 with the calculation of the equilibrium state of a population in a plateau-shaped fitness landscape (also called mesa landscape) for finite sequence length. We calculate finite sequence length corrections to the maximum principle, thereby improving the accordance of analytical and numerical results significantly. For the calculations we exploit an analogy to quantum mechanics and map the systems equation of state to a Schrödinger equation. All results are confirmed by numerics in section 3.5. After this comprehensive analysis of fitness landscapes with one mesa, we turn in chapter 4 to the competition between selection and robustness, also called survival of the flattest. The so far derived results are used to answer the question in which cases more robustness is preferable to higher selection values. We find that for finite sequence lengths, a broader but smaller fitness plateau can maintain a population at large mutation rates, where a higher but narrower plateau already fails. In the limit of infinite sequence length and fixed plateau widths, the higher plateau always provides the highest fitness for the population. We provide a formula for the critical sequence length, beyond which only the higher plateau can maintain a localized population. Additionally, the notion of the ancestral population is introduced and discussed for mesa-shaped fitness landscapes with two plateaus. Before drawing a final conclusion in chapter 6 we discuss the occurrence of the error threshold in a general epistatic landscape in chapter 5, thereby improving a previous result [86].

Chapter 2

Basic principles

In this chapter we introduce the basic concepts and notions of population genetics and dynamics needed. We focus on so-called deterministic mutation-selection-models for haploid asexual species, the quasispecies models. Haploid means that each individual of the species contains only one string of information (e.g. the DNA or RNA string). Asexual means that each individual can produce offspring autonomously, e.g. via cell division, and deterministic refers to an infinite population size. So we are in a context that allows for description of large populations of bacteria and viruses, but not higher developed organisms. Due to their simplicity, these quasispecies models can serve as toy models to find e.g. the characteristics of a certain fitness landscape.

2.1 Terms and definitions

As indicated in the introduction (chapter 1), we can characterize the individuals of the considered species by the string they carry. This string $\sigma = (s_1, .., s_L)$, of length L contains letters $s_i \in \mathcal{A}$ which are taken from an alphabet $\mathcal{A}$ of size $|\mathcal{A}| \geq 2$. In classical population genetics this string is just the DNA or RNA of an individual, so the alphabet $\mathcal{A}$ is of size four and there are 4^L possible sequences which form the sequence space [1]. In the simplest case the two letters A and G and the letters C and T (U) are pooled respectively as A and G are purins and C and T (U) are pyrimidines. These are to some extent exchangeable. Then we get an alphabet consisting of 2 letters $\mathcal{A} = \{+1, -1\}$ and 2^L possible sequences. If we connect all sequences of the set of all possible sequences in such a way, that a connection is made between all sequences that differ only by one site, we get the sequence space with the topology of a hypercube, an illustration of which can be seen in figure 2.1.

As is known from evolutionary biology, individuals well-adapted to their environment have the best chance to produce a large number of offspring, thereby passing on their information sequence. The fraction of not well-adapted individuals is diminished over time, dies out or survives only by mutation effects, as the individuals produce less offspring. If we assume that an information

[1] Depending on the posed question also other information strings can be taken to characterize the individuals. For example it can be the information of the gene configuration of the individual (which allele of a certain gene this individual has).

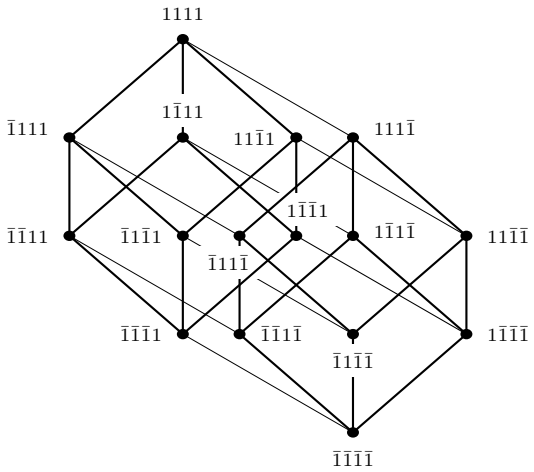

Figure 2.1: Illustration of the sequence space for binary sequences of length four with an alphabet consisting of ± 1. The letter -1 is abbreviated $\bar{1}$ in the picture. The sequence space has a hypercubic topology.

string $\sigma = (s_1, .., s_L)$ characterizes the individuals, a quantifying degree of adaptation should be connected with each of the possible sequences. This degree of adaptation is usually called the fitness and its value is connected to the effective number of offspring an individual produces per unit time. In the context of population genetics the fitness is usually assigned to the genotype instead of the phenotype because the connection between the two is complicated and mostly unknown[2].

We assume the generations of the considered population to be non-overlapping and the generation time to be normalized to one. Then we can describe the evolution of this species by a discrete time model where the time takes discrete values $1, 2...$, according to the actual generation. For a discrete time model the fitness F_σ then is the expected number of offspring an individual with sequence σ produces. It is also called the Wrightian fitness. We can now perform a continuum limit in time, corresponding to the limit of small generation time $\Delta t \to 0$, such that the total amount of offspring produced in a finite time span is constant. Then the number of offspring is reduced, when the individuals' lives are shorter, and we also have to perform a continuum time limit in the fitness function F_σ. We write

$$F_\sigma \equiv e^{w_\sigma \Delta t} \tag{2.1}$$

and call w_σ the *Malthusian fitness*. Sending the generation time Δt to zero, we find to first order in time

$$F_\sigma \equiv e^{w_\sigma \Delta t} \approx 1 + w_\sigma \Delta t \ , \quad \text{for} \quad \Delta t \to 0 \ . \tag{2.2}$$

[2] All individuals with a certain sequence σ^* belong to the same genotype. The phenotype comprises all genotypes that produce the same characteristic traits of individuals. The mapping from geno- to phenotype is thus typically from many to one. A simple example is the formation of amino acids by triplets of the nucleotides. There are 20 amino acids but $4^3 = 64$ possible combinations of three nucleotides (of which there are four different ones). So several combinations of nucleotides lead to the production of the same protein.

The Malthusian fitness is the important quantity for a continuous time model, like the Wrightian fitness is for the discrete time models. Equation (2.2) reflects the idea of reduced offspring for smaller generation times. As next step, we also want to include the effect of mutations either due to the environment or due to copying errors during reproduction. On the level of genes and nucleotides a mutation changes a sequence into another one, for example by changing single sites. This basic type of mutation is called point mutation. We concentrate in this work on point mutations only. If we assume that the mutation probability μ is uniform throughout the whole sequence and is the same for all letters in the alphabet, we can write down the mutation probability for an abitrary sequence σ to mutate into another arbitrary sequence σ' as

$$Q_{\sigma\sigma'} = \left(\frac{\mu}{|\mathcal{A}|-1}\right)^{k(\sigma,\sigma')} (1-\mu)^{L-k(\sigma,\sigma')} \ . \tag{2.3}$$

The first factor accounts for the probability that the differing sites are mutated into each other, while the second factor represents the probability that the other, already matching sites do not mutate. Here

$$k(\sigma,\sigma') = \frac{1}{2}(L - \sum_{i=1}^{L} s_i s'_i) \tag{2.4}$$

is the *Hamming distance* of the two sequences σ and σ', which is just the number of different sites. The mutation probability $Q_{\sigma\sigma'}$ is the same for all sequences σ' which have Hamming distance k to sequence σ. The number N_k of sequences with the same Hamming distance to sequence σ is

$$N_k = \binom{L}{k}(|\mathcal{A}|-1)^k \ . \tag{2.5}$$

$Q_{\sigma\sigma'}$ is a real probability as $\sum_\sigma Q_{\sigma\sigma'} = 1$. This normalization condition simply states that the sequence σ' mutates to some other sequence — or stays the same. When performing the continuous time limit we need to change from mutation probabilities to mutation rates $\eta_{\sigma\sigma'}$. This is done by

$$Q_{\sigma\sigma'} \approx \delta_{\sigma,\sigma'} + \eta_{\sigma\sigma'} \cdot \Delta t, \quad \text{for} \quad \Delta t \to 0 \ . \tag{2.6}$$

If we denote the mutation rate per letter by $\tilde{\mu}$ and set $\mu = \tilde{\mu}\Delta t$ then

$$\eta_{\sigma\sigma'} = \begin{cases} 0 & , \ k(\sigma,\sigma') > 1 \\ \tilde{\mu} & , \ k(\sigma,\sigma') = 1 \\ -\tilde{\mu}L & , \ k(\sigma,\sigma') = 0 \end{cases} \tag{2.7}$$

The normalization condition reads $\sum_\sigma \eta_{\sigma\sigma'} = 0$. A review about the topic of mutation and selection can e.g. be found in [3].

A special class of fitness landscapes are the so-called *permutation-invariant* fitness landscapes, in which only the number of mutations away from the wild type sequence σ_o and not their position is important for a sequence's fitness. In mathematical terms, this means $w_\sigma = w_{k(\sigma,\sigma_o)}$. Though being a simplification, permutation-invariant fitness landscapes are applicable to relevant systems, like to the binding energies of proteins to binding sites in the regulatory region of a gene [39].

2.2 Models

2.2.1 Eigen model

To describe the evolution of the population, we need to specify the interplay between the different ingredients. Here we take into account only mutations occurring as copying errors during reproduction and deterministic evolution[3]. For finite generation time this situation is described by the Eigen model [30]. In consequence, the fraction of individuals $P_\sigma(t)$ carrying sequence σ at time t evolves to the next generation according to

$$P_\sigma(t+1) = \frac{\sum_{\sigma'} Q_{\sigma\sigma'} F_{\sigma'} P_{\sigma'}(t)}{\sum_{\sigma'} F_{\sigma'} P_{\sigma'}(t)} \ . \tag{2.8}$$

$\Sigma_{\sigma'}$ runs over all possible sequences and for binary sequences $Q_{\sigma\sigma'}$ is given by

$$Q_{\sigma\sigma'} = \mu^{k(\sigma,\sigma')}(1-\mu)^{L-k(\sigma,\sigma')} \ . \tag{2.9}$$

Again $k(\sigma,\sigma')$ is the Hamming distance between the sequences σ and σ'. We notice the fact, that the model is invariant under multiplication of the fitness by a constant factor $F_\sigma \to C \cdot F_\sigma$. The equations can be linearized by changing to an unnormalized population distribution $Z_\sigma(t)$ via [51]

$$Z_\sigma(t) = P_\sigma(t) \prod_{\tau=0}^{t-1} \sum_{\sigma'} F_{\sigma'} P_{\sigma'}(\tau), \tag{2.10}$$

at the cost of non-locality in time. We then arrive at the linear equations

$$Z(\sigma, t+1) = \sum_{\sigma'} Q_{\sigma\sigma'} F_{\sigma'} Z_{\sigma'}(t) \ . \tag{2.11}$$

This linearized version is easier to solve, when calculating stationary states. By renormalization of the result $Z^*(\sigma)$, we regain the normalized population distribution $P^*(\sigma)$. But for convenience we will in the following work with a continuous time model, the Crow-Kimura model, which can be inferred from (2.8) by the limit generation time $\Delta t \to 0$ as shown below.

2.2.2 Crow-Kimura model

To derive the proper continuous time evolution from the discrete time model (2.8), we use (2.2) and (2.6) to paraphrase the dynamics for short generation time Δt. Writing $P_\sigma(t+\Delta t) \approx P_\sigma(t) + [d_t P_\sigma(t)]\Delta t$, we find

$$d_t P_\sigma(t) = (w_\sigma - \bar{w})\, P_\sigma(t) + \sum_{\sigma'} \eta_{\sigma\sigma'} P_{\sigma'}(t). \tag{2.12}$$

Therein $\bar{w}$ is defined through $\bar{w} = \Sigma_{\sigma'} w_{\sigma'} P_{\sigma'}(t)$. Now we assume the (Malthusian) fitness to be a function w_k only of the Hamming distance k to the optimal sequence at $k = 0$. Then, surpressing the time dependence, renaming the point mutation rate $\tilde{\mu} \to \mu$ and using (2.7), we can rewrite (2.12) to the final and here needed formulation of the Crow-Kimura model

$$d_t P_k = (w_k - \bar{w})P_k + \mu(k+1)P_{k+1} + \mu(L-k+1)P_{k-1} - \mu L P_k, \tag{2.13}$$

[3] achieved by assuming infinite population size

with $1 \leq k \leq L-1$. For $k = 0$ and $k = L$ the equations obviously have to be modified. Still, the deterministic character of this equation is justified by an infinitely large population. The nonlinearity introduced by the mean (malthusian) fitness $\bar{w}(t) = \sum_k w_k P_k$ can be eliminated by passing again to unnormalized population variables via the transformation [51, 80]

$$Z_\sigma(t) = P_\sigma(t) \cdot \exp\left(\sum_{\sigma'} \int_0^t d\tau P_{\sigma'}(\tau)\right). \tag{2.14}$$

The resulting linearized CK-model for the case of fitness landscapes only depending on the Hamming distance then reads

$$d_t Z_k(t) = (w_k - \mu L) Z_k(t) + \mu(k+1) Z_{k+1}(t) + \mu(L-k+1) Z_{k-1}(t). \tag{2.15}$$

From the solution of this linearized set of equations, the normalized solution can be reconstructed via

$$P_k(t) = \frac{Z_k(t)}{\sum_{k'} Z_{k'}(t)}. \tag{2.16}$$

In the following we will be concerned with the equilibrium states of (2.13), or rather (2.15). The stationary states can be found by the separation ansatz

$$P_k(t) = \mathrm{e}^{\lambda t} P_k^*. \tag{2.17}$$

implying the largest of all possible eigenvalues $\Lambda = \max \lambda$ to dominate the behavior of the system in the long-time limit. In the corresponding eigenvalue equation

$$\begin{aligned} \Lambda P_k^* &= (w_k - \mu L) P_k^* + \mu(k+1) P_{k+1}^* + \mu(L-k+1) P_{k-1}^* \\ &=: \mathbf{M}_{k,k'} P_{k'}^* \qquad \forall k = 0, ..., L \\ \Leftrightarrow \Lambda \mathbf{P}^* &= \mathbf{M} \mathbf{P}^* \end{aligned} \tag{2.18}$$

the $L \times L$ fitness-mutation-matrix $\mathbf{M}$ only consists of real non-negative entries. So the Perron-Frobenius theorem is applicable here, ensuring the existence of an unique, positive, and real largest eigenvalue Λ, and a corresponding principal eigenvector $\mathbf{P}^*$ that only has non-negative entries. This eigenvalue Λ is equal to the long-time limit of the mean population fitness $\bar{w}$, as can be seen by inserting the stationarity condition $P_k(t) = P_k^*$ into (2.13) using (2.18), and it is the main quantity of interest in this work. The CK-model is invariant under additive shifts of the fitness, $w_k \to w_k + c$, as counterpart to the Eigen model.

In figure 2.2 the equilibrium population P_k^* of the CK-model is shown as function of the mutation rate per letter μ for a single peak landscape $w_k = \delta_{k,0}$ and a sequence length of $L = 100$. With growing mutation rate, the population becomes uniformly distributed in sequence space, a phenomenon called error threshold, which will be discussed in the next section.

We will work with the Crow-Kimura model for the rest of this first part, as the continuous time formulation is more convenient to handle and the derived results are qualitatively also valid for the Eigen model.

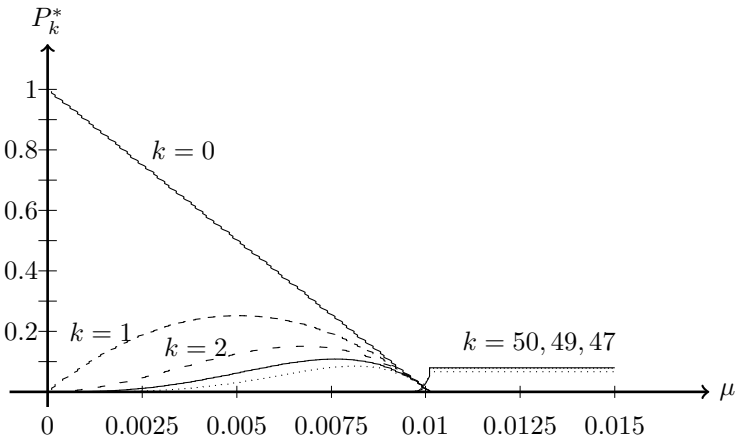

Figure 2.2: Part of the equilibrium population distribution of the quasispecies population in a sharp-peak landscape $w(k) = \delta_{k,0}$ with sequence length $L = 100$. Shown are the normalized population fractions P_k^* for different Hamming distances k. Some very important ones are labeled in the picture. The data is obtained numerically, as described in section 3.5.

2.3 Fitness landscapes and robustness

The still missing ingredient of our population model is the fitness landscape. These landscapes typically serve as toy functions, in the hope, that the model captures some important aspects of reality. In the last section, we already introduced one important class of fitness functions, the permutation invariant landscapes. To this class — to which we will stick in this work — belong several famous landscapes, like the *sharp-peak landscape*, introduced by Eigen [30]

$$w_k = w_0 \delta_{k,0}, \qquad w_0 > 0, \tag{2.19}$$

where only the master sequence has a high fitness. This reflects an extreme kind of epistasis (see below). It is applicable, if e.g. the environment sets very strong conditions on the population. In the *Fujiyama* (or multiplicative) landscape

$$w_k = w_0 - b \cdot k \qquad , w_0, b > 0 \tag{2.20}$$

every mutation away from the master sequence reduces the fitness by the same amount, while in *epistatic* landscapes like [86]

$$w_k = w_0 - b \cdot k^\alpha \qquad , w_0, b, \alpha > 0 \tag{2.21}$$

the reduction depends on the number of already occured mutations. Depending on the epistatic factor α every additional mutation away from the master sequence is punished more ($\alpha > 1$) or less ($\alpha < 1$) than the previous one. We will discuss the case of epistatic landscapes in detail in chapter 5. In these two latter types of landscapes, mutations are non-lethal (in the way which will be discussed in sec. 2.4 below) but lead to a reduction of offspring. In the corresponding populations we typically find mutational variety and the width of the population

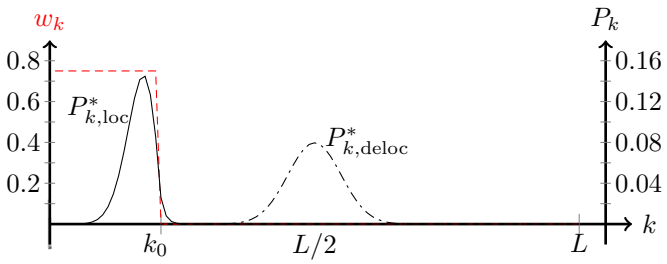

Figure 2.3: Equilibrium population distribution for the localized $P_{k,\mathrm{loc}}$ and delocalized $P^*_{k,\mathrm{deloc}}$ population distribution, as function of the Hamming distance k in a plateau-shaped fitness landscape with a plateau width k_0. The left y-axis belongs to the fitness (dashed line), the right y-axis to the population distributions P^*_k. We see the localized population to reside mainly at the edge of the plateau as due to the mapping from sequence to Hamming space, the number of sequences there is larger than at $k = 0$. The delocalized population is normally distributed around the Hamming distance $L/2$.

distribution (in Hamming space) depends on the mutation rate, as well as on the parameters of the landscape.

Coming back to our concerns, we want to discuss the effects of robustness on a population. This is a concept of central importance in current evolutionary theory [26, 55]. Here we address specifically *mutational robustness*, which we take to imply the stability of some biological function with respect to mutations away from the optimal genotype. To be precise, suppose the genotype is encoded by a sequence of length L, and the number of mismatches with respect to the optimal genotype is denoted by k. Robustness is then quantified by the maximum number of mismatches k_0, that can be tolerated before the fitness of the individual drops significantly below that of the optimal genotype at $k = 0$. This situation arises e.g. in the evolution of regularity motifs, where the fitness is a function of the binding affinity to the regulatory protein [39, 9]. This *mesa*-shaped fitness function is the simplification of a Fermi function at low temperatures, which in turn appears e.g. in simple thermodynamic models for the binding probability of a transcription factor to a regulatory region. Assuming that the fitness is independent of k both for $k \leq k_0$ and for $k > k_0$, the fitness landscape is parametrized by the width k_0 and height w_0 of the mesa [68]. In figure 2.3, a (permutation invariant) mesa-shaped fitness landscape and the corresponding localized and delocalized population distribution in Hamming space are depicted. In the following we will especially analyze this type of mesa landscapes and come later on to the more general case of epistatic landscapes. We use the terms mesa and plateau landscape interchangeably.

2.4 Error threshold

Depending on the shape of the fitness function and the mutation rate per letter μ, in quasispecies models a localization-delocalization phase transition, also called *error threshold* can occur. At this threshold the population undergoes a transition from a localized state around the fittest sequence(s) to a population homogeneously spread in sequence space (which corresponds to a binomial distri-

bution in Hamming space). For a population this transition can be interpreted as insensitivity towards changes in fitness or as the extinction of the (real) finite population to which the model is applied to.

To analyze any transition in which the mean Hamming distance of a population changes[4], the population averaged "magnetization" M, defined by

$$M = 1 - 2\langle x\rangle \in [-1, 1] \text{ with } \langle x\rangle = \frac{1}{L}\sum_{k=0}^{L} kP_k^*, \tag{2.22}$$

is a convenient though not fundamental quantity — the principal eigenvalue Λ of (2.18) is the fundamental quantity determining P_k^*. If the whole population only consists of master sequences ($k = 0$ by definition), the magnetization is $M = 1$. If only the inverse master sequence is present, the magnetization becomes $M = -1$. For a uniform distribution in sequence space (delocalized population) the magnetization is $M = 0$. Thus we can in most cases distinguish the qualitatively different states a population assumes under different mutation rates (except the mentioned pathologic cases), by considering the population averaged magnetization M as a function of μ. There are some special cases, where only the observation of the magnetization becoming zero is not sufficient, like in the case of the Fujiyama (or multiplicative) landscape, where the population remains localized but its average Hamming distance is — with growing mutation rate — continuously shifted towards $k = L/2$. Then we have to retreat to the analysis of the quality of change of either the population mean fitness $\Lambda(\mu)$ or the magnetization.

To obtain meaningful results in the limit $L \to \infty$, the mutation probability has to be scaled to zero accordingly, $\mu \to 0$, [5]. Another possible scaling — we do not adopt here — is to scale the fitness $\propto L$. For most fitness landscapes a scaling with $\mu L = \text{const.}$ is appropriate, but the right scaling can often only be obtained from the calculation of the critical mutation rate (error threshold) μ_{tr} itself. An example for a landscape where the scaling $\mu L = \text{const}$ is inappropriate is the epistatic landscape which will be discussed in chapter 5.

The order of the phase transition is somewhat delicate to estimate. The intricacy lies in the sequence of performing limits. As we here will frequently use numerics to confirm our analyical results, we always work with finite sequence lengths. So, the limit of infinite sequence length is the last one to be performed. For finite sequences we see the error threshold to resemble a second order phase transition. For this reason, we will here consider the error threshold to be of second order. When estimating the order of the transition after performing the infinite sequence length limit, the error threshold will be of first order, as the order parameter performs a discontinuous jump from $M = 1$ at $\mu = 0$ to $M = 0$ at $\mu \neq 0$. Though we have to point out here, that the error threshold, in the sense of a proper physical phase transition only exists in the limit $L \to \infty$. This discussion is also taken up in the paper by Tarazona [79] in the context of a treatment of the models as Ising chains. Nevertheless, other opinions on the order of the error threshold and which order parameter should be taken exist. For a different view on the topic see e.g. [44].

[4] pathologic cases like a (changing) population distribution symmetric to $x = 1/2$ are not covered!

[5] otherwise the mutation probability per sequence would diverge

2.5 The maximum principle

So far, we have presented the basic ingredients and how they enter into the models. Now we turn to finding the equilibrium state and the growth rate of a population in a given environment (represented by the fitness function). Therefore we have to solve the set of equations (2.18). To its solution, a considerable body of work has already been devoted for large L. If, in addition to the scaling constraints on μ, the fitness landscape w_k is assumed to depend only on the *relative* number of mismatches, such that

$$w_k \to f(x), \quad x = k/L, \tag{2.23}$$

then for $L \to \infty$, the principal eigenvalue in (2.18) is given by the solution of a one-dimensional variational problem as [44, 2, 74, 67, 73, 4]

$$\Lambda = \max_{x\in[0,1]} \{f(x) - \gamma[1 - 2\sqrt{x(1-x)}]\}, \tag{2.24}$$

where $\gamma = \mu L$. Moreover, if $f(x)$ is differentiable the leading order correction to (2.24) takes the form [67, 73]

$$\Delta\Lambda = \frac{\gamma}{2L\sqrt{x_c - x_c^2}}[1 - \sqrt{1 - 2f''(x^*)(x_c - x_c^2)^{3/2}/\gamma}], \tag{2.25}$$

where x_c is the value at which the maximum in (2.24) is attained. Therefore, we need other methods when analyzing the main features of robustness using a mesa-shaped fitness landscape of the form

$$w_k = \begin{cases} w_0 > 0 & : \quad 0 \le k \le k_0 \\ 0 & : \quad k > k_0, \end{cases} , \tag{2.26}$$

as w_k is not differentiable any more. Here w_0 denotes the selective advantage of the functional phenotype and k_0 is the number of tolerable mismatches. For scaling landscapes (2.23), here realized by

$$f(x) = w_0\Theta(x - x_0), \tag{2.27}$$

where $\Theta(x)$ is the Heaviside function and $x_0 = k_0/L$, at least the maximum principle can be applied ($x_0 < 1/2$) to yield

$$\Lambda = \begin{cases} w_0 - \gamma(1 - 2\sqrt{x_0(1-x_0)}) & , w_0 > w_0^c \\ 0 & , w_0 < w_0^c \end{cases} \tag{2.28}$$

with $w_0^c = \gamma(1 - 2\sqrt{x_0(1-x_0)})$. The value w_0^c of the selective advantage marks the location of the error threshold at which the population delocalizes from the fitness plateau and the location x_c of the maximum in (2.24) jumps from $x_c = x_0$ to $x_c = 1/2$.

To calculate the leading order correction $\Delta\Lambda$ to the maximum principle for finite sequence length in the next chapter, we will clarify and use an analogy to quantum mechanics, thereby rederiving the maximum principle (2.24), and we will show that $\Delta\Lambda$ is of order $L^{-2/3}$ or $L^{-1/2}$ rather than L^{-1} in the case of the pure maximum principle for scaling landscapes.

Chapter 3

Continuum limit in Hamming space

We want to solve the problem of finding the influences and limits of robustness in deterministic mutation-selection models. Robustness is implemented as a plateau-shaped fitness function into the Crow-Kimura model as introduced above. Based on the existing approaches, we clarify the connections between these different accesses and use a formal analogy to quantum mechanics to finally solve the issue of mutational robustness. Therefore, we first derive a description of the CK-model in a continuous Hamming space. Then we are able to find a finite size correction in harmonic approximation and beyond, using an analogy to quantum mechanics. Here we can connect to the work of Gerland and Hwa [39]. As reference method, we study the system by means of direct numerical calculations and find the analytical results verified.

3.1 Analytical derivation in harmonic approximation

A natural ansatz to analyzing (2.18) for large sequence lengths L is a continuum limit in Hamming space, that is in the index k. Therefore, we introduce the small parameter $\epsilon = 1/L$ and replace the population variable P_k by a function

$$\phi(x) = \lim_{L\to\infty} P_{xL}. \tag{3.1}$$

Furthermore we assume the fitness to be of the general form (2.23). By expanding the finite differences in (2.18) up to second order in ϵ, we get a differential equation of second order,

$$f\phi - \epsilon\gamma \frac{d}{dx}\left[(1-2x)\phi\right] + \frac{\epsilon^2\gamma}{2}\frac{d^2}{dx^2}\phi = \Lambda\phi, \tag{3.2}$$

which is a stationary drift-diffusion equation. By changing back to the unscaled variable $k = Lx$, we can see, that the equation is identical to the one obtained by Gerland and Hwa [39]. Nevertheless, we will see that x is the proper variable to perform the continuum limit, not the least because it fulfills the mathematical constraint of a compact support.

In order to solve equation (3.2) it is advantageous to eliminate the first-order drift term, which can be done by the transformation

$$\phi(x) = \sqrt{\phi_0(x)}\psi(x), \tag{3.3}$$

with

$$\phi_0(x) \propto \exp[-(1-2x)^2/(2\epsilon)]. \tag{3.4}$$

It is easy to see, why this transformation symmetrizes the linear operator in (3.2). In the absense of selection, $f = 0$, the principal eigenvalue in (3.2) is $\Lambda = 0$, and the corresponding (right) eigenvalue is a Gaussian centered at $x = 1/2$ and thus just given by (3.4). This Gaussian is the central limit approximation of the binomial distribution

$$P_k^0 = 2^{-L}\binom{L}{k}, \tag{3.5}$$

which solves (2.13) for $w_k = 0$ $(\forall k)$ and $\Lambda = 0$. It is well known that the central limit approximation of (3.5) is valid in a region of size $\sqrt{L}$ around $k = L/2$, but becomes imprecise for deviations of order L.

The theory of large deviations provides an improved approximation by the ansatz

$$P_k \propto \exp(-Lu(x)) \tag{3.6}$$

with $u(x)$ being the large deviations function. This ansatz, which has been recently suggested for this problem by Saakian [74], will be explained in more detail in Appendix A.1.

And though we have just shown that the drift-diffusion approximation is only accurate near $x = 1/2$, the center of the Hamming space, we will stick to this approach, as it allows a fundamental understanding of the problem. First, we can make contact with the work of Gerland and Hwa and second can we reformulate the eigenvalue problem in the language of standard quantum mechanics. The well developed formalism of quantum mechanics then allows to extend the solution of the eigenvalue problem beyond the second order approximation made in equation (3.2).

But coming back to solving the drift-diffusion equation (3.2), inserting (3.3) leads to the equation

$$-\frac{\epsilon^2\gamma}{2}\frac{d^2}{dx^2}\psi + V(x)\psi = -(\Lambda - \epsilon\gamma)\psi, \tag{3.7}$$

with

$$V(x) = \frac{\gamma}{2}(1-2x)^2 - f(x). \tag{3.8}$$

A sketch of $V(x)$ for different values of γ and a mesa-shaped fitness landscape (2.27) can be found in Fig 3.1.

Using standard quantum mechanics, we can interpret (3.7) as the stationary Schrödinger equation for a particle of mass $1/\gamma$ exposed to the effective potential (3.8) and energy eigenvalue $-(\Lambda - \epsilon\gamma)$ in one dimension and space representation.

The potential is the superposition of a harmonic oscillator centered at $x = 1/2$ and the negative fitness landscape. The qualitatively different cases are depicted in figure 3.1. As pointed out in [68], the inverse sequence length ϵ plays the role of Planck's constant $\hbar$, which implies that the case of interest is the *semiclassical*

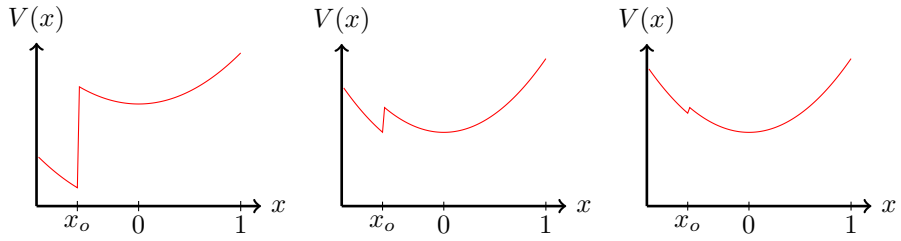

Figure 3.1: Sketch of the effective potential $V(x)$ (3.8) for different values of the mutation rate γ. For small mutation rates (figure on the left), the population is localized on the plateau. At the critical mutation rate γ_c (figure in the middle) the ground state is degenerate and thus allows for a transition of the population from a localized (minimum at $x = x_0$) to a delocalized (minimum at $x = 0$) state and vice versa. And for large mutation rates (figure on the right) the population is delocalized.

limit of the quantum mechanical problem. In particular, for $\epsilon \to 0$ the ground state energy $-\Lambda$ becomes equal to the minimum of the effective potential. We thus arrive at the variational principle

$$\Lambda = \max_{x\in[0,1]} [f(x) - \frac{\gamma}{2}(1-2x)^2], \tag{3.9}$$

which is precisely the *harmonic approximation* of the (exact) relation (2.24). In the perspective of quantum mechanics, the error threshold corresponds to a shift between different local minima of $V(x)$, which become degenerate at the transition point. The transition is generally of first order, in the sense that the location x_c of the global minimum jumps discontinuously. Within the harmonic approximation the transition occurs at

$$w_0^c = \frac{\gamma}{2}(1-2x_0)^2 \approx \frac{\gamma}{2}\left(1 - \frac{4k_0}{L}\right) \tag{3.10}$$

for $x_0 = k_0/L \ll 1$, following the argumentation of section 2.5.

3.2 Extension of the harmonic approximation

The so-far used harmonic approximation around $x = 1/2$ breaks down near the boundaries $x = 0$ and $x = 1$. However, to access the regime $1 \ll k_0 \ll L$, an accurate treatment of the region of small $x \ll 1$ is clearly necessary, especially, since we want to connect to the work of Gerland and Hwa [39] who obtain a seemingly contradictory result for the critical plateau needed for a localized population. The quantum mechanical treatment can be extended such that it becomes quantitatively valid over the whole interval $0 \le x \le 1$. Based on the considerations of [73], we then arrive at the modified Schrödinger equation (see appendix A.1 for a derivation)

$$-\epsilon^2\gamma\sqrt{x(1-x)}\frac{d^2}{dx^2}\psi + \left[\gamma(1-2\sqrt{x(1-x)}) - f(x)\right]\psi = -\Lambda\psi, \tag{3.11}$$

which differs from (3.7) in two respects. First, the potential (3.8) is replaced by

$$V_{\text{full}}(x) = \gamma(1-2\sqrt{x(1-x)}) - f(x). \tag{3.12}$$

In the asymptotic limit $\epsilon \to 0$ the principal eigenvalue is given by minimizing V_{full}, which exactly recovers the maximum principle (2.24). Second, the mass of the quantum particle described by (3.11) becomes position dependent,

$$m(x) \mathrel{\widehat{=}} \left(2\gamma\sqrt{x(1-x)}\right)^{-1}, \tag{3.13}$$

which replaces the simple identification $m \mathrel{\widehat{=}} 1/\gamma$ in the harmonic case.

3.3 Finite sequence length corrections

From the considerations of sections 3.1 and 3.2, we can infer correction terms to (2.24) for finite sequence lengths. Within the harmonic approximation, for finite but large sequence lengths $\epsilon = 1/L \ll 1$ we have to include quantum corrections to the classical limit solution (3.9). Assuming a smooth fitness function $f(x)$, the ground state wave function is localized near the minimum x_c of the effective potential, and the shift in the ground state energy can be computed by a harmonic approximation of $V(x)$,

$$V(x) \approx V(x_c) + \frac{1}{2}V''(x_c)(x-x_c)^2 = V(x_c) + \frac{1}{2}[4\gamma - f''(x_c)](x-x_c)^2. \tag{3.14}$$

Identifying $1/\gamma$ with the mass m of the quantum particle and comparing the correction term to the potential of a harmonic oscillator $V_{\text{har}} = m\omega^2 x^2/2$, we find the frequency of the oscillator to be

$$\omega = 2\gamma\sqrt{1 - f''(x_c)/4\gamma}. \tag{3.15}$$

By further exploiting this analogy, we find the ground state energy contribution of the correction term to be

$$E_0 = \frac{\hbar\omega}{2} \cong \frac{\epsilon\omega}{2} = \epsilon\gamma\sqrt{1 - f''(x_c)/4\gamma}. \tag{3.16}$$

Re-inserting the results into (3.7), we get an expression for the leading order correction to Λ:

$$\left[-\frac{\epsilon^2\gamma}{2}\frac{d^2}{dx^2}\psi + V(x_c)\psi\right] = -(\Lambda - \epsilon\gamma + \frac{1}{2}\epsilon\omega)\psi \tag{3.17}$$

$$=: -(\Lambda + \Delta\Lambda)\psi. \tag{3.18}$$

The correction term

$$\Delta\Lambda = \frac{\gamma}{L}[1 - \sqrt{1 - f''(x_c)/4\gamma}] \tag{3.19}$$

coincides with (2.25) evaluated for $x_c \approx 1/2$. Analogously, the width ξ of the wave function can be estimated via $\xi = \sqrt{\hbar/(2m\omega)}$ to be[1]

$$\xi = \sqrt{\gamma\epsilon/2\omega} = \frac{\sqrt{\epsilon\gamma}}{[8\sqrt{1 - f''(x_c)/4\gamma}]^{1/4}}. \tag{3.20}$$

[1] Note that, because of the factor $\sqrt{\phi_0}$ in (3.3), this is not equal to the width of the stationary population distribution.

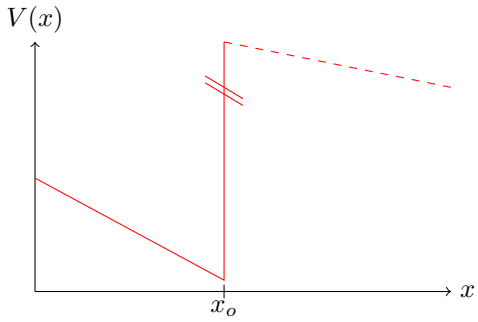

Figure 3.2: Sketch of the effective potential $V(x)$ near $x_c = x_0$. The slope left of the step is to first order given by $-a = V'(x_0)$. The height of the step is w_0, which can — for small ϵ — be considered as effectively infinite, since the kinetic energy of the particle is linear in ϵ.

In the case of the mesa landscape (2.27), the potential near $x_c = x_0$ consists of a linear ramp of slope

$$-a = V'(x_0) = 2\gamma(2x_0 - 1) < 0 \tag{3.21}$$

followed by a jump of height w_0, see figure 3.2 . For small ϵ, the jump can be considered as effectively infinite (as the kinetic energy of the particle is then very small since being linear in ϵ) and we retrieve the well-known 1d-quantum mechanical ground state problem of a particle in a negatively sloped potential terminated by an infinitely high wall. The solution, provided by the Airy function, is standard textbook material, e.g. [71] and we obtain for our problem the prediction

$$\Delta\Lambda = z_1(\hbar^2/2m)^{1/3}a^{2/3} = 2^{1/3}z_1\gamma(1-2x_0)^{2/3}L^{-2/3} + \mathcal{O}(L^{-1}), \tag{3.22}$$

where $z_1 \approx -2.33811...$ is the first zero of the Airy function. The scaling $\Delta\Lambda \sim L^{-2/3}$ was already noted in [68]. Again, the width of the wave function can be estimated and is of the order

$$\xi \sim (\hbar^2/ma)^{1/3} \sim \epsilon^{2/3} \tag{3.23}$$

in this case. These considerations can also be applied to the extended solution of equation (3.11) in section 3.2. Inserting (3.12) and (3.13) into the expression (3.22) for the finite size correction yields

$$\Delta\Lambda = 2^{-1/3}z_1\epsilon^{-2/3}\gamma(1-2x_0)^{2/3}[x_0(1-x_0)]^{-1/6}. \tag{3.24}$$

For fixed x_0 this still scales as $\epsilon^{2/3} = L^{-2/3}$, but when taking $L \to \infty$ at fixed k_0, such that $x_0 \to 0$, we find instead that

$$\Delta\Lambda \to 2^{-1/3}z_1\gamma x_0^{-1/6}\epsilon^{2/3} = 2^{-1/3}z_1\gamma k_0^{-1/6}L^{-1/2}. \tag{3.25}$$

3.4 Connection to former results

3.4.1 Review

A recent study on mesa-shaped fitness landscapes with finite sequence length was done by Gerland and Hwa (GH) [39]. They approach the problem by assuming from the outset $1 \ll k_0 \ll L$. So the maximal number of non-lethal mismatches is small compared to the sequence length. Then they perform the limit of infinitely long sequences $L \to \infty$ and focus on the region $k \ll L$ at the same time, while keeping the Hamming distance k as the variable in which the limit is performed. As an intermediate result they recover eq. (3.2) (in terms of k), but then neglect the contribution $2k/L$ (corresponding to $2x$) in the drift term. As a result the drift term becomes constant for all k.

In the localized regime, the stationary population distribution is of the form

$$\phi(k) \quad = \quad e^k \psi(k) \tag{3.26}$$

in terms of the Hamming distance k. But the potential of the corresponding Schrödinger equation to (3.7) is given by $-\gamma/2 \cdot f(x)$. Due to the 'zoomed in' view on the system, the error threshold manifests itself in the non-normalizability of the solution or in other words, when $\psi(x)$ decays as $e^{-x/\epsilon} = e^{-k}$. This is also the point, where the assumption of sufficient slow variation of $\psi(k)$ on the scale of k (needed for the continuum limit) is violated. Then for a broad fitness plateau $k_0 \gg 1$, GH find a critical plateau height of

$$w_0^c = \frac{\gamma}{2}\left(1 + \frac{\pi^2}{k_0^2}\right). \tag{3.27}$$

This result clearly shows a dependence on the absolute number of allowed mismatches k_0, but is independent of the sequence length L, apparently in contrast to (3.10).

3.4.2 Comparison

To understand the role and applicability of our results and the one of GH,we have to take a closer look on the validity of both approaches. For didactical reasons we start on the level of the harmonic approximation (sec. 3.1) and then extend the comparison to the improved solution (sec. 3.2). The harmonic approximation solution (3.10) is valid for large k_0 and breaks down, when the width of the wave function ξ becomes comparable to the potential well provided by the effective potential $V(x)$. In the case of the mesa landscape, this is tantamount to

$$\xi \sim x_0, \tag{3.28}$$

which leads to

$$k_0 \sim \epsilon^{-1/3} = L^{1/3} \tag{3.29}$$

using (3.23) and $x_0 = \epsilon k_0$. If we consider short plateaus with $k_0 \ll L^{1/3}$, the ground state energy of the corresponding wave function can be estimated to

$$E_0 \sim \frac{\hbar^2}{md^2} \sim \frac{\epsilon^2\gamma}{x_0^2} \sim \frac{\gamma}{k_0^2}, \tag{3.30}$$

where d is the width of the confinement potential (in our case x_0). This contribution exceeds the harmonic contribution $\sim k_0/L$ in (3.10) usually by far. So in the case $x_0 \to 0$, the most important correction to the 'classical ground state energy' (3.9)

$$\Lambda = w_0 - \frac{\gamma}{2} \tag{3.31}$$

is a *negative* contribution $\sim \gamma/k_0^2$. This in turn leads to an increase of w_0^c, as qualitatively seen in (3.27). But the range of application of (3.27) is very small. In the case of smooth fitness landscapes, the harmonic approximation already breaks down at $k_0 \sim L^{1/2}$, due to the central limit approximation. Nevertheless, the energy contribution of the wave function $\sim \gamma/k_0^2$ dominates the $\gamma k_0/L$-term in (3.10) only, if $k_0 \ll L^{1/3}$. Hence, the GH regime is in this case not visible.

But since the harmonic approximation is not valid in the interesting region of broad but relative small plateaus, $k_0, L \gg 1$, $x_0 \ll 1$, we will now improve our solution and refine the just made conclusions made about the GH regime.

Within the improved solution of section 3.2, mass and slope now diverge as $m, a \sim x_0^{-1/2}$ for $x_0 \to 0$. So, the width of the wave function scales as

$$\xi \sim (\hbar^2/ma)^{1/3} \sim (\epsilon^2 x_0)^{1/3} = \epsilon k_0^{1/3}, \tag{3.32}$$

instead of $\xi \sim x_0$ in the harmonic approximation. Consequently, the breakdown condition $\xi \gg \epsilon k_0$ of the semiclassical approximation is never satiesfied and the "quantum confinement regime" discussed just before does in fact not exist. For the finite size corrections we expect equation (3.24) to be valid for all k, L, as long as $k_0, L \gg 1$.

3.5 Numerics

To test the analytical predictions derived in the preceding sections, we have carried out a detailed numerical study of the dependence of Λ and w_0^c on k_0, L and γ. In the first part of this section we discuss the method used to obtain the numerical data presented in the second part.

3.5.1 Numerical method

For the calculation of numerical values for the mean fitness Λ or the critical plateau height w_0^c it is necessary to calculate the equilibrium state of the population described by (2.13) or in other words, the largest eigenvalue of the matrix defined by (2.18) and the corresponding principal eigenvector P^*. An iteration of (2.13) does in most cases not lead to the equilibrium state in acceptable time, as the convergence is very slow.

For the calculations we used `Matlab` and the included subroutines, especially the `LAPACK` package, since it is best suited for large and sparse matrices. To achieve short calculation times, we symmetrized the original set of stationary equations (2.18) via the transformation

$$
\begin{aligned}
P_k &\rightarrow \Pi_{k,k}^{-1} \cdot P_k, && (3.33)\\
M_{k+1,k} &\rightarrow \Pi_{k+1,k+1}^{-1} M_{k+1,k} \Pi_{k,k}, && (3.34)\\
\Pi_{k,k} &= \sqrt{\binom{L}{k}}, && (3.35)
\end{aligned}
$$

which is exactly the discrete transformation analogous to the symmetrization operation (3.3) of the analytic ansatz (see also Appendix A). In doing so, we arrive at the following eigenvalue equation

$$
\begin{aligned}
\Lambda P_k^{*,\mathrm{sym}} &= (w_k - \gamma) P_k^{*,\mathrm{sym}} + \mu\sqrt{(L-k)(k+1)}(P_{k+1}^{*,\mathrm{sym}} + P_{k-1}^{*,\mathrm{sym}})\\
&=: \Sigma_{k'} M_{kk'}^{\mathrm{sym}} P_{k'}^{*,\mathrm{sym}} \qquad ,\forall k \in \{0,...,L\} \qquad (3.36)\\
\Leftrightarrow \Lambda \mathbf{P}^{*,\mathrm{sym}} &= \mathbf{M}^{\mathrm{sym}} \mathbf{P}^{*,\mathrm{sym}}.
\end{aligned}
$$

First we test the accuracy of the method by calculating the sensitivity of the fitness-mutation matrix to pertubations, by determining the condition number of the fitness-mutation matrix $\mathbf{M}^{\mathrm{sym}}$. The condition number of a matrix is defined as the product of the largest singular values of the matrix itself and its inverse. The values are obtained from singular decomposition of the matrix. The smaller the condition number is, the more stable the matrix behaves towards small pertubations of the matrix elements. We find that the system is stable for small mutation rates but becomes unstable for $\mu \to \frac{1}{2}$. For small mutation rates between zero and the error threshold μ_{tr} we find numbers of the order of 10^1 to 10^3. For $\mu = \frac{1}{2}$ the condition number diverges. For more information on the condition number and singular-value decomposition we refer to Appendix B.

To find the dependence of Λ or w_0^c on k_0, L or γ, we carried out the calculation of Λ or w_0 for each set of parameters independently. The price for this independent data is the not arbitrarily high density of data points in the plots. Thus in many plots the numerical curve is a bit stepped.

To obtain the critical values of the plateau height w_0^c, or the mutation rate μ, the order parameter M (see equation (2.22)) is calculated for each set of parameters. The average of the two values of w_0 or μ next to the qualitative change of M then give the desired critical value.

3.5.2 Results

We extensively tested the analytical predictions versus the numerical results. Here we only show some representative examples of these. In figure 3.3 two examples for the dependence of Λ on the plateau width k_0 are depicted. The prediction of the asymptotic maximum principle (2.24) reproduces the qualitative behavior of the numerical data but significantly overestimates the value of Λ. The $L^{-2/3}$ finite size correction (3.22) derived in the harmonic approximation improves the comparison, but quantitative agreement is achieved only using the refined expression (3.24), which is proportional to $L^{-1/2}$.

Figure 3.4 shows a similar comparison for the critical plateau height w_0^c. Here the prediction (3.27) of GH is also included and seen to match the numerical outcome only poorly, whereas the maximum principle result with the finite size correction (3.24) produces excellent agreement.

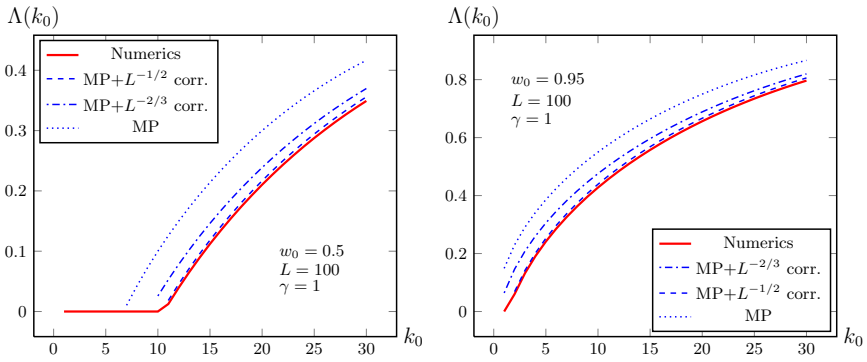

Figure 3.3: Growth rate Λ as a function of the plateau width k_0 for two values of the plateau height $w_0 = 0.5, 0.95$. The sequence length is $L = 100$ and the mutation rate per sequence is $\gamma = 1$. The solution of the maximum principle together with the $L^{-1/2}$-correction term (including the position-dependent mass) provides the best agreement with the numerics. The numerical values of the growth rate have been obtained by (numerical) calculation of the largest eigenvalue of the matrix defined by equation (2.18), c.f. subsection 3.5.1.

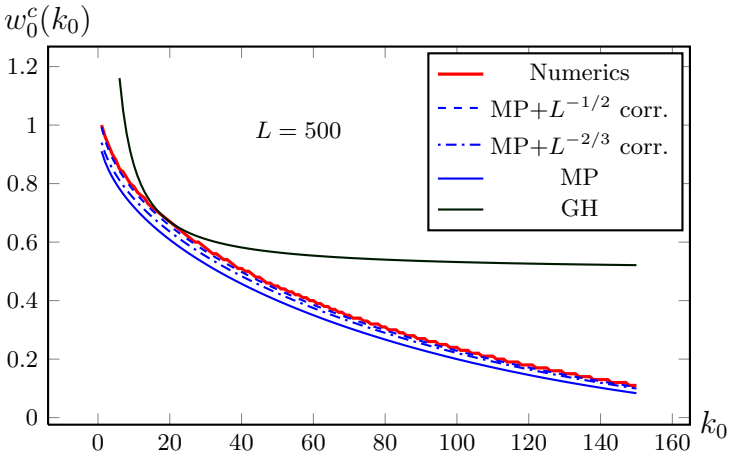

Figure 3.4: Critical plateau height w_o^c as a function of the plateau width k_0. The sequence length is $L = 500$ the mutation rate per sequence $\gamma = 1$. The solution of the maximum principle together with the $L^{-1/2}$-correction term provides the best overall agreement with the numerics. With increasing the plateau width k_0, the $L^{-2/3}$ and $L^{-1/2}$-corrections approach each other. The prediction by GH matches the numerics very poorly and does not reflect the qualitative behavior of $w_0^c(k_0)$ in contrast to the other solutions. The analytical solution for the maximum principle (and correction term) has been obtained by equating the two solutions of (2.28) and solving for w_0^c. The numerical values have been obtained via calculation of the average magnetization M of the population and determining the plateau height, where M jumps from finite value to zero. See page 14 for a detailed discussion of M and subsection 3.5.1 for a discussion of the numerical method.

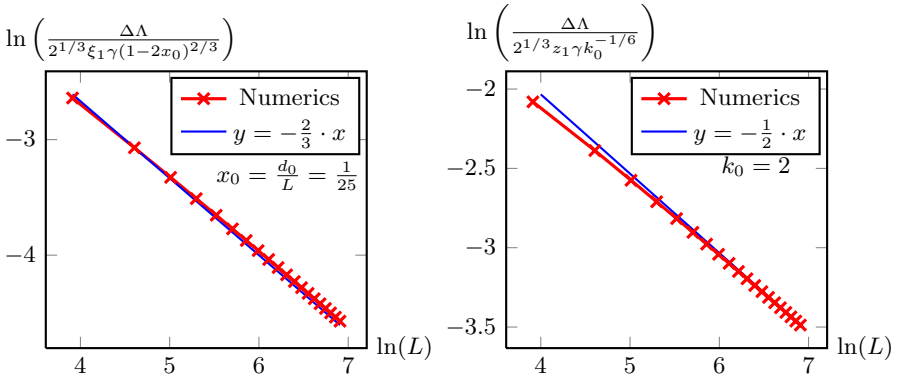

Figure 3.5: Illustration of the power of the sequence length in the correction term for fixed relative and absolute plateau width. $\Delta\Lambda$ has to be understood as the numerical value for the growth rate Λ_{num} less the value obtained by the maximal principle, eq. (2.24). For fixed relative plateau width, as well as for fixed absolute width, the numerics show the same exponent of the sequence length as the corresponding analytical result.

Finally, in the left picture of figure 3.5 we verify that the finite size correction $\Delta\Lambda$ indeed varies as $L^{-2/3}$ when L is increased at fixed *relative* plateau width x_0. The right figure shows the corresponding $L^{-1/2}$ dependence for fixed *absolute* plateau width k_0. Altogether, we find the analytical propositions affirmed.

Hereby, we stop the discussion of fitness landscape with one plateau and continue with the question, to what extend a robust species is superior to a species with higher fitness but less tolerance for mutations, using the analytical results obtained in this chapter.

Chapter 4

Fitness landscapes with competing plateaus

4.1 The selection transition

We now apply the analytical theory to the phenomenon of the survival of the flattest as explained in the introduction (chapter 1). We want to find out to what extent robustness (in the sense of plateau width) outcompetes selection (fitness of a Hamming class) — for finite sequence lengths and in the limit $L \to \infty$.

In the literature this question has already been discussed to some extent by Schuster and Swetina [75]. The question can be answered by investigating a fitness landscape consisting of two fitness plateaus at the opposing ends of the Hamming space (see figure 4.1). As was shown in [75], for small μ the interference between the two plateaus is negligible when they are separated by a few mutational distances. The stationary state of the system is therefore to a very good approximation determined by the comparison between the population growth rates associated with each of the two plateaus in isolation. In [17] experimental evidence for the existence of similar fitness landscapes and the interplay of fitness and mutation rate in virus populations is given.

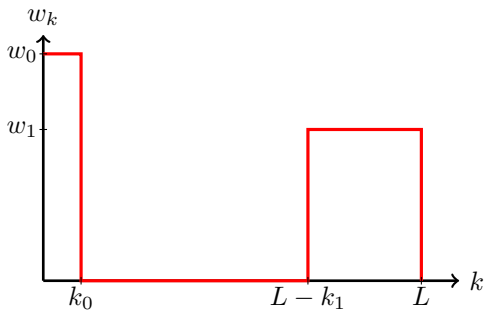

Figure 4.1: Illustration of a fitness landscape with two plateaus. This type of landscape is used to investigate the influence of height and (relative) broadness of the plateaus on the population fitness Λ.

For the CK model (and the Eigen model as well), observing the mean Hamming distance of the population[1] as function of the mutation rate and for fixed sequence length, we find two types of transitions. The first one is a jump of the population from the higher to the broader plateau, which we will refer to as the *selection transition* [79] taking place at a mutation rate μ_s. The second transition is the well-known error threshold taking place at μ_{tr}, where the population becomes uniformly spread in sequence space.

The selection transition is a sharp transition, even for finite sequence lengths, while the error threshold is a continuous transition for finite sequence lengths and becomes sharp only in the limit $L \to \infty$. Both transitions are illustrated in the left figure of 4.2. With growing sequence length, both critical rates μ_s and μ_{tr} become smaller and approach each other, until, at a critical sequence length L^*, they reach the same value and the selection transition vanishes. For all larger sequence lengths, the population directly delocalizes from the high, narrow plateau, as can be seen in the right figure of 4.2.

Using the maximum principle this behavior can be understood quite easily. By evaluation and comparison of (2.24) on both plateaus we find the selection threshold as the mutation rate, at which the population mean fitnesses for both plateaus are equal:

$$\mu_s = \frac{w_0 - w_1}{2\left(\sqrt{k_1 L - k_1^2} - \sqrt{k_0 L - k_0^2}\right)} \approx \frac{w_0 - w_1}{2(\sqrt{k_1} - \sqrt{k_0})} L^{-1/2}. \tag{4.1}$$

We assumed $k_0, k_1 \ll L$ in the last step. Quite analogously, for each plateau the error threshold μ_{tr}^i, $i = 0, 1$ is obtained by the vanishing of the corresponding eigenvalue Λ_i (a delocalized population has an eigenvalue of zero), yielding

$$\mu_{tr}^{(i)} = \frac{w_i}{L\left(1 - 2\sqrt{k_i L - k_i^2}\right)} \approx \frac{w_i}{1 - 2\sqrt{k_i/L}} L^{-1}. \tag{4.2}$$

The error threshold observed in the population is then the smaller of both values. Since the error threshold decreases faster with growing sequence length, than the selection threshold, the error threshold of the high plateau will be encountered before the selection threshold for sufficiently long sequences, implying the selection threshold to be no longer observable. The critical sequence length L^* at which the selection threshold disappears, can be calculated by equating the expressions (4.1) and (4.2)

$$L^* \approx \frac{4(w_0\sqrt{k_1} - w_1\sqrt{k_0})^2}{(w_0 - w_1)^2}, \tag{4.3}$$

where we used the approximated expressions.

For comparison with the former work of Swetina & Schuster and Tarazona [75, 79], we used a fitness landscape with short plateaus $k_0 = 1$ and $k_1 = 2$, and relative fitness values $w_1/w_0 = 0.9$, for which (4.3) gives a critical sequence length of $L_a^* \approx 106$. Our numerical calculations shown in the left figure of 4.3 reveal a significant underestimation of $L_n^* \approx 285$, which is not notably improved by using the full finite sequence corrections for the principal eigenvalues derived in section 3.2. But this is not surprising, as in the continuum approach of chapter 3

[1] or the eigenvector corresponding to the equilibrium state of the population

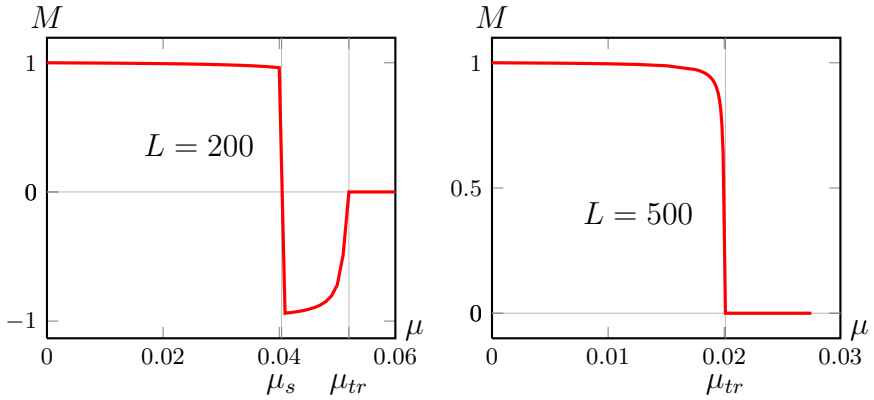

Figure 4.2: Order parameter M as function of the mutation rate μ per site for a fitness landscape with a high plateau at $k = 0$ and a broad plateau at $k = L$. For short sequence lengths one can observe a hopping of the population from the higher to the broader plateau and then a delocalization (left picture). For long sequences, one only observes the delocalization transition from the higher fitness plateau (right picture). The hopping between the plateaus we call the *selection transition*. It takes place at mutation rate μ_s. The delocalization transition, also called error threshold, takes place at a mutation rate μ_{tr}. The underlying fitness landscape is $w_k = 10 \cdot \Theta(0 - k) + 9 \cdot \Theta(k - (L - 1))$.

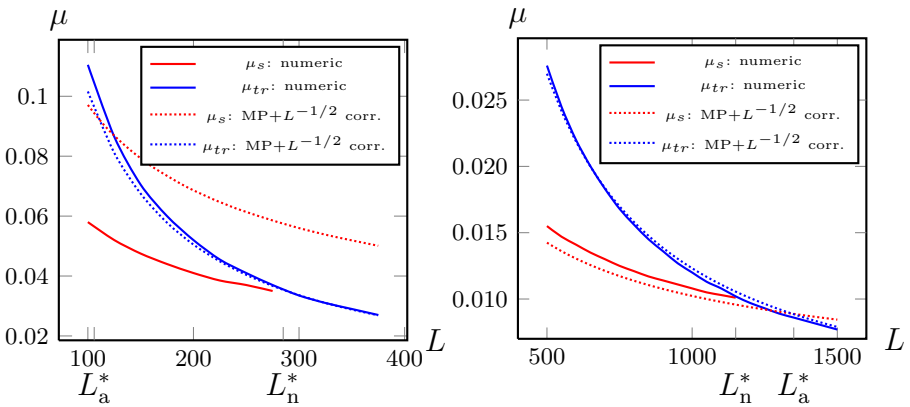

Figure 4.3: Critical mutation rate μ_s of the selection transition and μ_{tr} of the error threshold for the fitness landscape $w_k = 10 \cdot \Theta(0 - k) + 9 \cdot \Theta(k - (L + 1 - 2))$ (left figure) and $w_k = 10 \cdot \Theta(10 - 1 - k) + 9 \cdot \Theta(k - (L + 1 - 20))$ (right figure) as functions of the sequence length. The two lines cross at a critical sequence length L^*. The selection transition is observed only for sequence lengths smaller than L^*. The numerical data are compared to analytic predictions based on the maximum principle including the $L^{-1/2}$-correction term. As before, the numerical values have been obtained by calculating the magnetization of the population and determining for each sequence length the mutation rate where the magnetization jumps from a finite value to zero. The difference between the numerical and analytical values, especially of μ_s, are much smaller for longer sequences and broader plateaus, as well as the relative error between L^*_{a} and L^*_{n}.

$k_i \gg 1$ was assumed and we cannot expect quantitative accuracy for plateau widths of order unity. We also carried out calculations for other relative and absolute heights as well as different plateau widths, especially broader plateaus. Representatively shown in the right figure of 4.3 are the results for a landscape with ten times broader plateaus, namely $k_0 = 10$ and $k_1 = 20$, and the same absolute fitness values. Here we see, a much better agreement between numerical and analytically predicted values for μ_s and μ_{tr}, leading to a smaller relative error on the prediction of L^*.

To complete this discussion, we mention that for scaling fitness landscapes (in the sense $x_0 = k_0/L = \text{const.}$ and $x_1 = k_1/L = \text{const.}$ for $L \to \infty$), the selection transition as well as the error threshold are maintained at fixed values $\gamma_s = \mu_s L$ and $\gamma_{tr} = \mu_{tr} L$ for $L \to \infty$ [74].

Simulations performed with digital organisms [87], show the outcompetition of a high but narrow fitness peak by a smaller but broader fitness area also for more rounded fitness peaks.

4.2 The ancestral distribution

In addition to the equilibrium population distribution P_k^* $(t \to \infty)$, we can also consider the *ancestral distribution*, the equilibrium distribution of the backward time process, first introduced by Hermisson, Baake and others [44, 4] in the context of branching models. The ancestral distribution **a** contains the information on the origin of the observed equilibrium population and is obtained as the product of left and right eigenvectors, P^{**} and P^* respectively, of the mutation-selection matrix defined through (2.18). The probability, that a randomly picked individual at time t stems from an ancestor of type k ($\forall k = 1, .., L$) at time $t - \tau$ is in the limits $t \to \infty$ and $\tau \to \infty$ (performed in that order) given by $a_k = P_k^{**} \cdot P_k^*$ and is the distribution of ancestors weighted by the offspring they produce. Figure 4.4 depicts the idea.

Application to the fitness landscape with two competing peaks, shows that the ancestral population is either located on one or the other of the plateaus or delocalized (uniformly distributed in sequence space). Though, in contrast to the equilibrium population, the transitions between these states are all sharp even for finite sequence length, as illustrated in figure 4.5. The continuous transition of the equilibrium population at the error threshold is caused by the mutational pressure driving the population from the plateau to larger Hamming distances. And the stronger the pressure, the more does the population "leak out" from the plateau, a fact also found in experiments [17]. Yet, the population is mainly supported by the individuals on the plateau, since they produce the most offspring and maintain the population localized. Only, when eventually the mutational pressure becomes too strong and the equilibrium population delocalizes, the ancestral distribution is formed by the Hamming classes comprising the most sequences, so the ones around $k = L/2$.

To complete this discussion, we want to mention the connection of our work to the language of Ising chains and two-dimensional Ising models. As becomes clear in [79], the ancestral distribution is the same as the bulk distribution and the equilibrium distribution becomes the distribution of the surface layer. The "leakage effect" in the equilibrium population at the error threshold is also known as surface wetting in terms of two-dimensional Ising models [79].

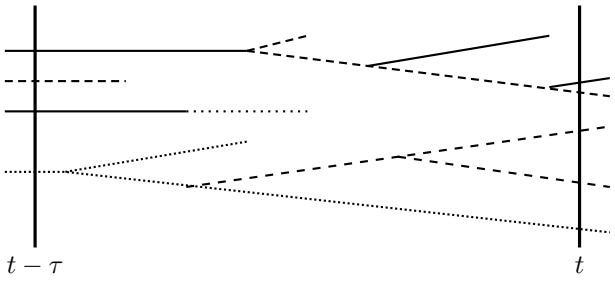

Figure 4.4: Sketch of the time evolution of an asexual population. Each line corresponds to one individual. Different genotypes are indicated by different line styles. At branching points offspring is produced and ending lines symbolize the death of an individual. Time is measured horizontally from left to right. The right eigenvector $\mathbf{P}^*$ of the mutation-selection matrix $\mathbf{M}$ (2.18) for $t \to \infty$ gives the equilibrium population distribution, while the left eigenvector $\mathbf{P}^{**}$ of $\mathbf{M}$ for $t, \tau \to \infty$ gives the distribution of ancestors weighted by their offspring. The ancestral distribution is the product of both (normalized) eigenvectors in the sense $a_k \sim P_k^* \cdot P_k^{**}$, $\forall k = 1, ..., L$.

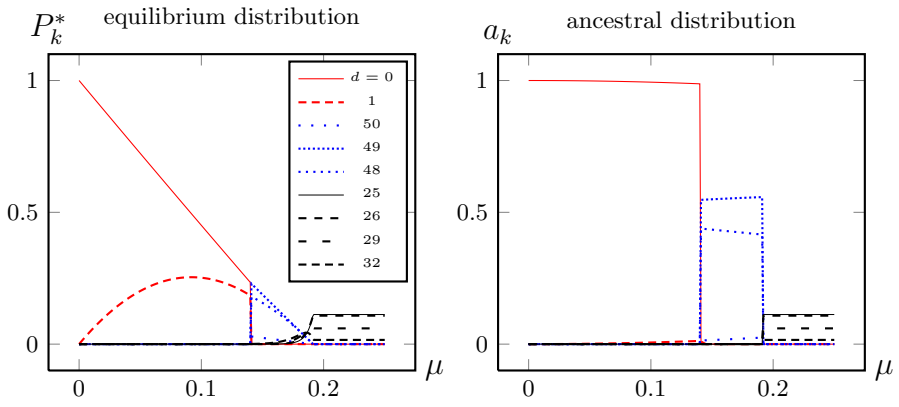

Figure 4.5: The dominant entries of the equilibrium and ancestral population distribution of the Crow-Kimura model as function of the mutation rate per site, calculated numerically. The underlying fitness landscape is the same two-plateau landscape used in Figs.4.2 and 4.3. As sequence length we chose $L = 50$. Occupation fractions are plotted only for the most populated Hamming classes. The two distributions undergo phase transitions at the same mutation rates, but at the error threshold the ancestral distribution undergoes a discontinuous transition, while for the equilibrium distribution the transition is continuous.

Chapter 5

Error threshold in epistatic fitness landscapes

So far, we have discussed robustness of phenotypes using plateau-shaped fitness landscapes, which are a special case of the class of epistatic fitness functions. We now discuss the latter in a more general framework. The original meaning of epistasis concerns the interaction between genes, namely the action of one gene blocking the action of another gene [7]. This definition was broadened by Fisher [35] to describe any form of gene interaction. Here, we mean by epistasis the non-linear dependence of the fitness function on the number of mismatches k [70]. Every additional mismatch is penalized harder (synergistic epistasis of deleterious mutations) or less hard (diminishing epistasis) than the previous one. The focus lies on the effect of epistasis on the existence of an error threshold.

Following Wiehe [86] we consider the following class of permutation invariant (Malthusian) epistatic fitness functions

$$w_k = w_0 - bk^\alpha, \tag{5.1}$$

where k is again the Hamming distance to the master sequence and $b > 0$ can be regarded as a selection coefficient. The epistatic factor α tunes the landscape. $\alpha > 1$ and $\alpha < 1$ produces landscapes with synergistic and diminishing epistasis, respectively. For $\alpha \to 0$ (5.1) reduces to the sharp-peak landscape $w_k = w_0 - b(1 - \delta_{k,0})$.

It is well known that an error threshold exists for $\alpha \to 0$, but not for $\alpha = 1$ [51]. For $\alpha = 1$ we recover the multiplicative or Fujiyama landscape, that can be solved analytically and though the magnetization of the population can reach zero, it does not undergo neither a discontinuous nor a delocalization transition, as well as the growth rate Λ itself. Neglecting backward mutations, Wiehe argued in [86] that an error threshold emerges whenever $\alpha < 1$.

In the following we show that, based on the maximum principle (2.24), the critical value of the epistasis exponent below which an error threshold develops is in fact $\alpha = 1/2$. For larger values of α we do not observe an error threshold.

As before, we work in the scaling limit $L \to \infty$ and $\mu \to 0$ with the mutation rate per sequence $\gamma = \mu L = \text{const}$. Next we change variables from k to x, so we can apply the maximum principle

$$w_k = f(x) = w_0 - \tilde{b}x^\alpha, \tag{5.2}$$

with $\tilde{b} = bL^\alpha$ and the usual $x = k/L$. The limit $L \to \infty$ should be combined with $b \to 0$, such that $\tilde{b} = \text{const}$. We are thus considering a situation where both the mutation rate per site and the selection forces are small. Applying the maximum principle (2.24) to this landscape, the mean fitness Λ of the population in the equilibrium state is given by

$$\begin{aligned}\Lambda &= \max_{x\in[0,1]} \{w_0 - \tilde{b}x^\alpha - \gamma[1 - 2\sqrt{x(1-x)}]\} \\ &=: \max_{x\in[0,1]} \lambda(x),\end{aligned} \tag{5.3}$$

where $\lambda(x)$ is the function that has to be maximized.

By setting $d\lambda/dx = 0$, we find the conditions under which the maximum of $\lambda(x)$ is attained *inside* the interval $x \in [0, 1]$, which leads to

$$\alpha x^{\alpha-1/2}\sqrt{1-x} = \frac{\gamma}{\tilde{b}}(1-2x). \tag{5.4}$$

The right hand side is a simple linear function of x, dropping from $\gamma/\tilde{b}$ at $x = 0$ to $-\gamma/\tilde{b}$ at $x = 1$. On the left hand side we find for $\alpha > 1/2$ a function, that vanishes at the endpoints $x = 0, 1$ and is positive-valued in-between, with slope zero at $x = 0$, infinite slope at $x = 1$ and a left-right turning point that only vanishes for $\alpha = 3/2$. The intersection x_c of the left and right hand side functions varies smoothly with $\gamma/\tilde{b}$ from $x_c = 0$ for $\gamma/\tilde{b} = 0$ to $x_c = 1/2$ for $\gamma/\tilde{b} \to \infty$. Since the left hand side is always positive-valued, we do not find an intersection with $x_c > 1/2$. Due to the smooth variation of the solution x_c with x, no error threshold (jumping) occurs for *any* value of $\gamma/\tilde{b}$.

For $\alpha < 1/2$, the exponent $\alpha - 1/2$ becomes negative and thus the left handed side diverges (to $+\infty$) additionally at $x = 0$. So, for (sufficiently) small $\gamma/\tilde{b}$ there is no solution of (5.4) and the maximum of $\lambda(x)$ has to be located on the boundary. The function $\lambda(x)$ itself is — for small $\gamma/\tilde{b}$ — monotonically decreasing, so its maximum is found at $x = 0$ over a range of small $\gamma/\tilde{b}$. With increasing $\gamma/\tilde{b}$, $\lambda(x)$ develops a local maximum inside $(0, 1)$ which finally exceeds the value at $\lambda(x = 0) = w_0 - \gamma$. This is, where the population jumps from $x = 0$ to $x_c \in (0, 1)$ discontinuously and we discover an error threshold. At which value of $\gamma/\tilde{b}$ the error threshold occurs clearly depends on the epistatic factor α, so we write

$$\frac{\gamma}{\tilde{b}} = g(\alpha) \tag{5.5}$$

where g is some (not further specified) function of the epistatic factor. From this relation we can recover the same scaling of the error threshold with sequence length as [86]

$$\mu_{tr} = \frac{\gamma_{tr}}{L} = g(\alpha)\tilde{b}L^{-1} = g(\alpha)bL^{\alpha-1}. \tag{5.6}$$

We can say a bit more about the characteristics of $g(\alpha)$. For the sharp-peak landscape $\alpha \to 0$, we know the error threshold to occur at $\gamma/\tilde{b} = 1$, so $g(\alpha = 0) = 1$. To find $g(\alpha = 1/2)$, we evaluate $\lambda(x)$ at $\alpha = 1/2$ and for $x \approx 0$:

$$\lambda(x) = w_0 - \gamma + \sqrt{x}(2\gamma\sqrt{1-x} - \tilde{b}) \approx w_0 - \gamma + \sqrt{x}(2\gamma - \tilde{b}) - \gamma x^{3/2}. \tag{5.7}$$

Reconciling $d\lambda/dx = 0$ for $x \approx 0$, we find $\gamma/\tilde{b} \approx 1/2$, leading to $g(\alpha = 1/2) = 1/2$. In the vicinity of $g(\alpha = 1/2) = 1/2$, for $\gamma/\tilde{b} \gtrsim 1/2$ and $0 < x \ll 1$, we can solve

$d\lambda/dx = 0$ and find $x_c = 2/3(2 - \tilde{b}/\gamma)$, which moves smoothly away from $x_c = 0$ at $\gamma/\tilde{b} = 1/2$.

Summing up, the population is localized at $x = 0$ for $\alpha < 1/2$ and small $\gamma/\tilde{b}$ until $\alpha = 1/2$ and $\gamma/\tilde{b} < 1/2$. For $\alpha < 1/2$ and large enough $\gamma/\tilde{b}$, $\lambda(x)$ develops a local maximum at $x_c > 0$ and eventually the population undergoes a discontinuous transition (error threshold) from $x_c = 0$ to $x_c > 0$. At $\alpha = 1/2$ this behaviour changes in the sense that here at $\gamma/\tilde{b} = 1/2$ the population is located at $x_c = 0$ and moves away continuously from there with growing $\gamma/\tilde{b}$, while for $\gamma/\tilde{b} < 1/2$ the population is located at $x_c = 0$ since $d\lambda/dx = 0$ has no solution in $(0, 1)$. For $\alpha > 1/2$ the population is always located at some x_c, that changes continuously with the parameters. So we find an error threshold for $\alpha < 1/2$ and $\gamma/\tilde{b} = g(\alpha)$. This behavior terminates at $\alpha = 1/2 = \gamma/\tilde{b}$, where the transition becomes smooth. This point can be interpreted as the critical endpoint terminating the discontinuous phase transitions occurring for $\alpha < 1/2$.

The specialty of the value $\alpha = 1/2$ is due to the fact, that here the leading order behavior of the fitness function (5.3) for small x is the same as of the entropic term $\sqrt{x(1-x)}$ in the maximum principle (2.24), namely $\sqrt{x}$.

The analytically derived behavior is fully confirmed by our numerical calculations. In figure 5.1 the existence of an error threshold for $\alpha < 1/2$ and its absence for $\alpha > 1/2$ is illustrated by displaying the magnetization M of the population as function of the mutation rate per sequence γ. For $\alpha < 1/2$ the magnetization shows a discontinuous jump, while for $\alpha > 1/2$ the magnetization is a smooth function of γ. The full phase diagram is depicted in figure 5.2. Here the error threshold in the sense of $\gamma/\tilde{b}$ is shown as function $g(\alpha)$ and varies nicely between $g(0) = 1$ and $g(1/2) = 1/2$. The deviations from theory in figure 5.2 are due to the finite sequence length calculations and become smaller with growing sequence length.

Since a similar term appears also for general alphabet sizes (see A.3), the considerations of this section hold in that case as well. Here we finish the discussion on robustness in mutation-selection models and conclude our findings in the next chapter.

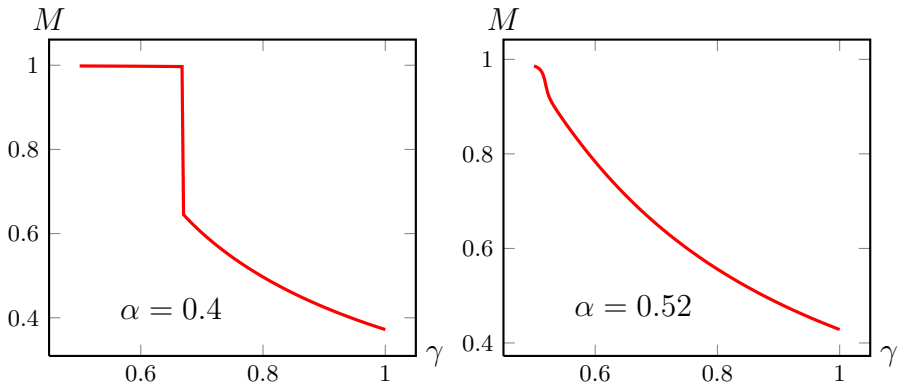

Figure 5.1: Magnetization as a function of mutation rate for the fitness landscape (5.1) with epistasis exponent $\alpha = 0.4$ and $\alpha = 0.52$, respectively. For $\alpha = 0.4$ the magnetization undergoes a discontinuous jump, whereas for $\alpha = 0.52$, it changes smoothly. The shown values of α have been chosen in order to show the qualitative difference of $M(\gamma)$ for $\alpha < 1/2$ and $\alpha > 1/2$. The numerical estimation of critical value of α_c. where the error threshold vanishes is estimated to $\alpha_c = 1/2$ within the bounds of the numerical stepsize. Calculations have been done for a sequence length of $L = 500$.

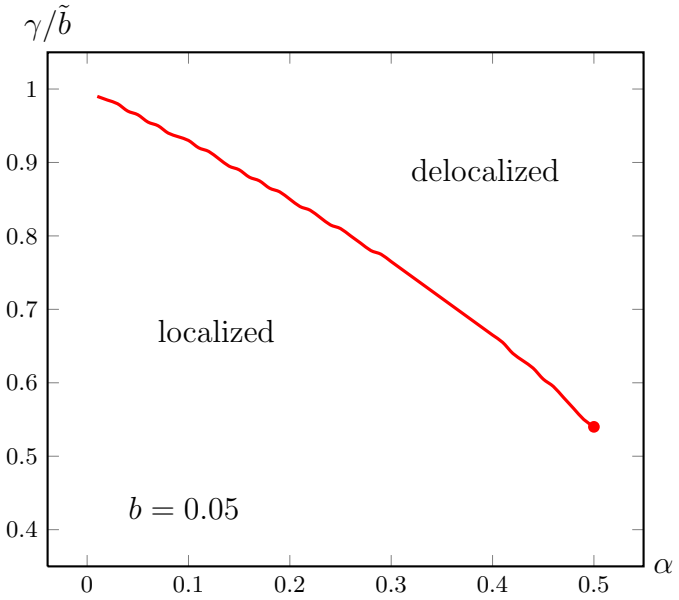

Figure 5.2: Numerically determined phase diagram for the epistatic fitness landscape (5.1). At the thick line the population undergoes a first order phase transition from a state localized at $x_c = 0$ (below the line) to a delocalized state $x_c > 0$ (above the line). This line terminates in a second order phase transition at $\alpha = 1/2$. The deviation from the prediction $\gamma/\tilde{b} = g(1/2) = 1/2$ at $\alpha = 1/2$ is due to finite sequence length corrections. For all larger values of the epistasis exponent, $\alpha > 1/2$, the population changes smoothly. Calculations have been performed for a sequence lengths of $L = 750$. The stair-like character of the line is only due to the numerical step size.

Chapter 6

Summary

We investigated a special aspect of population genetics, namely the concept of robustness against deleterious mutations in the context of quasispecies models. The concept itself has been studied previously within the framework of regulatory motifs [39, 9]. The model we used is the continuous time Crow-Kimura model, a deterministic model for large haploid and asexual populations. We analyzed the stationary state properties of such populations in epistatic fitness landscapes for sequences consisting of two letters. These fitness landscapes, especially the mesa landscape (an extreme kind of epistasis), are used to model robustness of phenotypes against deleterious mutations. In these landscapes the mastersequence and a certain amount of its neighboring sequences (in terms of the Hamming distance) have a high fitness value compared to all other sequences. Previous approaches provide a solution in the limit of infinitely long sequences as well as a first order correction term for smooth fitness landscapes [73, 74, 67, 79, 59].

Using an analogy to quantum mechanics, we were able to derive a correction term to the maximum principle for finite sequence lengths as well as for non-smooth landscapes, significantly improving the agreement between numerical calculations and the analytical predictions.

During the derivation of the correction terms, we reviewed two existing approaches [39, 44, 74] with different predictions for the plateau problem and clarified the reason for their discrepancy by expanding the approach [39] beyond the harmonic approximation. In particular, we could show, that the regime predicted by Gerland and Hwa [39] is not applicable to any finite size system.

The central result of our analysis is, that the relative number of mismatches $x_0 = k_0/L$ that could be tolerated by the population is the relevant parameter for the fitness effect of mutational robustness. We provide accurate expressions for its quantitative evaluation.

Having solved the problem for one fitness plateau, we tackled the problem of the optimal plateau shape providing the best mean fitness to a population under the influence of a given mutation rate. Therefore, we introduced a fitness landscape with two differently shaped plateaus, following the spirit of [75], and found an analogy to the error threshold, the so-called selection threshold, describing the jump of the population from the higher to the broader mesa with growing mutation rate. Due to the scaling with sequence length L, we showed, that this transition vanishes in the limit $L \to \infty$, if the plateau widths are *not* scaled with L.

In the last chapter 5 we discussed a more general family of epistatic landscapes with respect to the existence of the error threshold. Based on the results of [44, 4] we were able to improve on the results of [86] and showed that diminishing epistasis ($\alpha < 1$ in the fitness function (5.1)) is not a sufficient condition for an error threshold to occur, but rather $\alpha = 1/2$ marks the threshold.

With the fitness landscapes investigated here, we were able to clarify the essential characteristics of the "fitness landscape ingredients" epistasis, fitness plateau and different shapes of plateaus concerning the error threshold and highest mean fitness of a population described by quasispecies models.

Experimental evidence for all these ingredients to appear in real populations [17, 10, 15] and digital organisms [87] has been given.

Part II

Molecule formation on interstellar dust grain surfaces with quenched disorder

Chapter 7

Introduction

In space, simple and complex molecules are mainly produced in the molecular clouds of the interstellar medium. By interstellar medium (ISM) the matter in between the star systems is meant, which includes atoms, molecules and ions as gas and as well as dust. The denser parts of the ISM are called molecular clouds. In their younger age, they form stable clouds of matter usually far from thermal equilibrium, but when the cloud is massive enough and the gas pressure cannot sustain the gas, the clouds (or parts of a cloud) will undergo a gravitational collapse, finally leading to the formation of new stars.

Depending on the local temperature of the cloud and the presence of radiation (starlight), gas phase or surface processes are dominant for molecule formation. In the outskirts of the clouds, the temperature and the gas density are low, so here in general particles do not recombine by collisions in the gas phase. Instead the main process for molecule formation involves the surfaces of dust grains, as will be specified in the next paragraph. Particles impinging on these surfaces can overcome the activation energy needed for molecule formation with the help of the surface acting as a catalyst. A review on the early state-of-the-art can be found in [25].

The most abundant element is hydrogen in atomic as well as molecular form. About 90% of the ISM is made up by hydrogen. As such it is involved in many reactions and reaction networks leading to the formation of more complex molecules. Still the simplest reaction $H + H \rightarrow H_2$, occurring in the gas phase and on the surfaces, has not been completely understood yet. It has been known that the formation of molecular hydrogen from atomic hydrogen is far too inefficient in the gas phase [40] to explain the observed abundances at the measured cloud temperatures. Instead it is the most important surface reaction [48] with an underlying scenario of atoms impinging onto the grain surface, diffusing on this surface and — if meeting another atom before desorption — reacting with it to form a molecule [46, 47, 48]. Clearly, the (physical) binding strength offered to an atom by the surface has an impact on the production of molecules. Most relevant for our considerations of surface processes is the physisorption of atoms on the surface (van der Waals interaction). For chemically bound particles, also called chemisorbed, processes are believed to take place 'in' the matrix of the surface rather than 'on' the surface.

EXPERIMENTS: The quantitative predictions of models clearly depend on many parameters of gas and surface, like their temperature, gas composition,

grain geometry, porosity of the surface, size distribution of the grains, etc. Apart from observational data, we have no further information of the exact structure of interstellar dust grains.

Some questions regarding the influence of structure, porosity and other factors may be answered by laboratory experiments. While investigations of such surface features are notoriously difficult, thermodynamic and kinetic parameters of the whole surface can be determined by experiments. The most popular type of such experiments is *temperature-programmed desorption* (TPD), which will now be described briefly. In these experiments one puts a surface of a desired material composition and surface structure into a ultra-high vacuum (UHV) chamber that is cooled to very low temperature (using a Helium cryostat). Then at a fixed temperature, typically ≤ 30 K, the surface is exposed to atom beams of the elements of interest (very often this involves H and D atoms). Afterwards, the actual desorption phase starts. The surface sample is heated up linearly, which causes the deposited atoms (or formed molecules) to desorb from the surface. The emerging gas is aspirated and the constituents are determined by mass spectroscopy. By this kind of experiment the activation energy barriers for diffusion and desorption of the atoms and molecules can be estimated.

Materials found to be of astrophysical relevance are olivines (silicates) and amorphous carbon [52], as well as different sorts of ices, especially water and CO ice [23, 49]. These ices appear in the cloud regions where water or methanol is formed on the surfaces but cannot evaporate due to the low temperatures and missing other mechanisms (e.g. photodesorption) [23, 49].

Disorder - Experiments and observations: Hollenbach and Salpeter [47] argued already in the early seventies that disorder (in the binding and hopping energies) on the grain surfaces is needed to explain the observed quantities of molecular hydrogen. This is by now accepted in the astrochemical community [43]. The reasoning is, that even a few enhanced adsorption sites will increase the coverage of the grain by binding particles for a longer time and thus the highly mobile particles on the more shallow sites can find them and react.

Though from TPD experiments, complete binding energy distributions cannot be estimated reliably, several evidences for distributions of binding and hopping energies have been given. In their work on H_2 formation on surfaces covered with non-porous ice, Buch [16] and Hixson [45] give evidence for distributions of potential minima (binding energies in our terminology) and for a diffusion energy barrier distribution that can be approximated by a gaussian distribution. Cazeaux and Thielens [19] consider a surface with a combination of physisorption and chemisorption sites, which can be comprised to a system with effectively two different binding energies. We will study such a system as the simplest system with disorder in chapter 9.

As will be shown in this work, the distribution of binding energies of the underlying surface ("energy landscape") has indeed crucial impact on the molecule formation. We systematically investigate the influence of different (effective) binding (and diffusion) energy distributions on the efficiency in molecule formation of this surface.

The surfaces resulting from assigning different energies in one or another manner to its sites can be thought of as to display all sorts of geometrical or energetical features a surface could be equipped with. Examples are different materials on certain sites, surface steps, holes, other arrangements of sites, blocked sites e.g. by other molecules, etc.

Connection to the general framework of reaction-diffusion systems: In this part diffusion has to be understood in its original meaning of particle movement (here in two dimensions). The time scale of diffusion mediates or limits the encounter probability of particles. Upon meeting of two particles on the surface a reaction occurs immediately, namely the formation of a dimer (and its leaving of the system). Thus, the description through a reaction-diffusion system arises naturally. The appropriate reaction terms will be specified in chapters 9, 10, 11, and 12 for each of the examined systems, separately. The special ingredient to these systems is the spatial confinement, as the number of sites on the surface is finite and periodic boundary conditions are employed. We expect the presented results to be relevant for general systems with diffusion-mediated reactions.

Outline

After an introduction to the relevant notions in chapter 8, we will review the results on homogeneous systems. Then in chapter 9, we examine systematically the influence of disorder in the binding energies, starting from a system with binary disorder. We use a rate equation approach for a fundamental understanding of the problem and KMC simulations to verify our results. The main result is, that the interplay between the sites with different binding energies maintains a high efficiency of the system even at temperatures where the corresponding homogeneous systems perform poorly. Afterwards, we give a generalization to systems with discrete distributions of binding energies by means of simulations and a rate equation analysis in chapter 10. We can define a temperature-dependent mapping from discrete distributions to an effective binary system using rate equations. This is highly convenient to compute the system's efficiency regarding applications. A rate-equation-independent treatment of these systems will be provided after the discussion of systems with continuous distributions of binding energies in chapter 11. Here we can define a mapping from the system with the continuous distribution to an effective binary system, improving the understanding remarkably. This mapping only depends on the temperature and the continuous distribution itself. Since every (finite) realization of a system with an underlying continuous binding energy distribution comprises only a finite number of different binding energies, the application of the found mapping to the case of discrete distributions is straightforward. Before concluding on our work, we take a brief look on systems with two reactant species in chapter 12. The formation of molecules more complex than e.g. molecular hydrogen involves reactions between different particle species. In principle, these systems are accessible (and solvable) by a rate equations approach. Nevertheless, even for a simple generic system, we cannot provide a closed analytical solution for all temperatures. Only the energetically degenerated case can be fully understood by analytical means.

Chapter 8

The model

8.1 Basic principles

We study the simplest possible reaction of a single particle species forming dimers occurring in the ISM, the reaction $H + H \rightarrow H_2$. In this thesis we investigate the influence of rate disorder (on the surface) on this reaction. Hence, our system consists of one single-particle species and a surface. We think of this surface as a lattice of binding sites on which the particles forming the gas phase above can impinge onto. Throughout this work, we will assume the lattice to be a two-dimensional square lattice with S sites and periodic boundary conditions.[1] An illustration of the system and its implementation can be found in figures 8.1 and 8.2.

Each of the lattice sites i is characterized by a binding energy E_{W_i} specific for the type of particles. Particles from the gas can only stick to empty lattice sites. If a site is already occupied, the particle is rejected — this is known in surface chemistry as *Langmuir-Hinshelwood rejection* (LH-rejection) [57]. Furthermore, we assume the incoming particle flux per lattice site f to be constant and uniform for all lattice sites.

Once landed on the surface, the particles can explore the lattice by hopping between neighboring sites. The hopping rates a_s are undirected and only depend on the current particle position. In addition, particles can desorb from a site with rate W_s. In this model, both rates a_s and W_s depend on the binding energy at the particle position. We assume the rates a and W to be thermally activated

$$\begin{aligned} W_s &= \nu \, \mathrm{e}^{-\frac{E_{W_s}}{k_B T}}, \\ a_s &= \nu \, \mathrm{e}^{-\frac{E_{a_s}}{k_B T}}, \end{aligned} \tag{8.1}$$

with the attempt frequency ν, which is simply the vibrational frequency of the particle. In the following we set $k_B = 1$ and measure all energies in units of temperature. When two particles meet on the surface (by one particle hopping onto an already occupied site), they react and form a dimer which leaves the

[1] In [63, 65], the influence of the surface topology, shape and dimension on the efficiency of a homogeneous system has been analyzed in detail. As turns out, the impact of the disorder introduced in the following is much bigger than of the other factors mentioned before. Hence we concentrate on the disorder effects and keep the rest of the system as simple as possible.

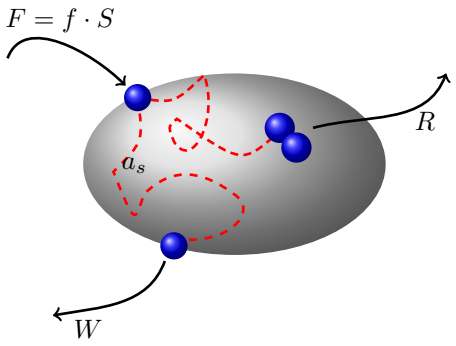

Figure 8.1: Schematic view of the dimer formation model. Atoms impinge with a homogeneous flux f per site, of which there are S on the whole surface, leading to a total flux of $F = f \cdot S$ from the surrounding gas onto the surface. The atoms can explore the surface by hopping with a (in general) site-dependent rate a_s and either leave the surface as single particle with (site-dependent) desorption rate W or — upon meeting another atom — react with it and leave the surface as part of a dimer with recombination rate R (global quantity). The estimation of R is the main task of this part of our work.

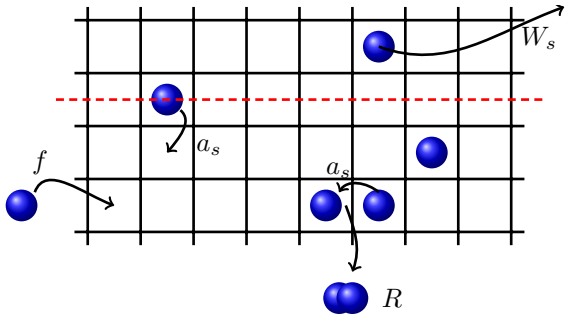

Figure 8.2: Implementation of the general model described by figure 8.1 and in chapter 8. Throughout this work, we assume the binding sites to have a coordination number of four. The influence of different coordination numbers on the efficiency has been investigated in [63] and will be of minor importance for our analysis. The red line indicates an exemplary cut, that will be used to sketch the particular binding energy landscape considered in the following chapters, see figures 9.1, 10.1, 11.1.

surface immediately. Since we are interested in stationary state properties of the system, the immediate leaving of the dimer needs not to be understood literally. If in a real system dimers stay on the surface for a typical time span, these sites are blocked for other particles. But the number of blocked sites is roughly constant and we can interpret S as the effective number of sites available to the particles. The quantity characterizing the system's state, is the efficiency η of the system, that is the ratio of particles that react on the surface and the total number of impinging particles. For its analytical and numerical evaluation, we make use of rate equations and kinetic Monte Carlo simulations, which will both be introduced in the next section 8.2.

To get a physically meaningful description, the system should be able to relax to its equilibrium state when the incoming particle flux is switched off. So we impose *detailed balance* to hold, which is equivalent to a vanishing net flux between any two nearest-neighbor sites. Let p_s be the probability to find a particle at site s. Then the stationary gain-loss equation for p_s is given by

$$(a_s + W_s)p_s = f + \sum_{s' \text{ nn of } s} \frac{a_{s'}}{z} p_{s'}, \tag{8.2}$$

where z is the coordination number of the lattice. The left-handed site accounts for the particle loss at site s by hopping to neighboring sites or desorption, the right-handed site describes the particle gain at site s by incoming particle flux and hopping from the nearest-neighbor sites. The demand for detailed balance is then expressed by

$$p_s \frac{a_s}{z} = p_{s'} \frac{a_{s'}}{z} \tag{8.3}$$

for the nearest neighbors s and s'. Inserting this condition into the stationary gain-loss equation (8.2) yields $p_s = f/W_s$ and by re-insertion into the detailed balance condition (8.3) we arrive at

$$\frac{W_s}{a_s} = \frac{W_{s'}}{a_{s'}}. \tag{8.4}$$

For a regular and fully connected lattice like the one considered here, this clearly implies $W_s/a_s = \text{const}$ for all sites s.

In the following we will use rate equations to estimate a system's efficiency analytically. Rate equations are gain-loss equations for the change in the number of particles on the lattice, and cover incoming particles due to the flux f, losing particles by desorption and losing particles through reactions. They do not cover topological or spatial effects and thus they only provide an appropriate analytical treatment if the system and the incoming particle flux are large enough. Deviations occur especially for small system sizes and very low incoming flux [11]. Such systems can for example be investigated by employing master equations.

For the model system of H_2 formation, we can compute the flux of H-atoms from the gas onto a grains surface. Assuming a temperature of the surrounding gas of $T_{\text{gas}} = 100K$ and a density $\rho_{\text{H,gas}} = 10/\text{cm}^3$ of H atoms in the gas phase, this defines the average velocity $v_{\text{H,gas}}$ of the particles:

$$v_{\text{H,gas}} = \sqrt{\frac{8T_{\text{gas}}}{\pi m_{\text{H}}}}. \tag{8.5}$$

In order to obtain meaningful results for possible applications, we will employ amorphous carbon as the standard surface, which is believed to be relevant in

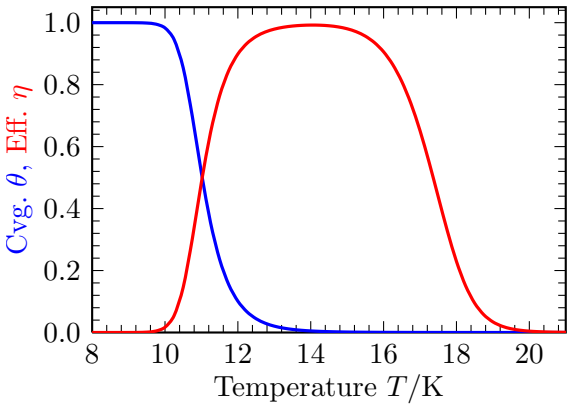

Figure 8.3: Coverage θ (blue) and efficiency η (red) as functions of temperature T, in the homogeneous model described by a rate equation. Parameters are chosen for an amorphous carbon surface.

the astrophysical context. The binding and hopping energies are then given by $E_W = 658$ K and $E_a = 511$ K [52]. From the density of sites on the surface $\rho_{\text{sites}} = 2 \cdot 10^{14}/\text{cm}^2$ we can then (approximately) compute the total flux (per grain) F and the flux onto each site of the grain f

$$\begin{aligned} F &= \rho_{\text{H,gas}} v_{\text{H,gas}} \cdot \pi R^2, \\ f &= \frac{F}{S} = \frac{\rho_{\text{H,gas}} \cdot v_{\text{H,gas}}}{4\rho_{\text{sites}}} \end{aligned} \tag{8.6}$$

where πR^2 is the cross section of the (spherical) grain and perfect sticking of the H-atoms on the grain is assumed. For the standard parameters of an amorphous carbon grain, the flux per site amounts to $f = 7.3 \times 10^{-9}/s$. For the attempt frequency we adopt $\nu = 10^{12}/\text{s}$, which has become the standard value for the attempt frequency in surface science.[2] Combining the above this defines a reaction-diffusion system in a spatially confined region.

8.2 Review: the homogeneous system

Systems with a homogeneous surface have been studied by means of rate equations [11, 52, 14], the master equation [41, 14], and moment equations [60, 6]. All these approaches have their advantages, disadvantages and limits. The general problem of homogenous systems is that astrophysical observations suggest a much broader temperature window of high efficiency than can be provided by any homogeneous system employing the parameters from laboratory experiments [46]. It has become apparant that disorder can enhance the efficiency dramatically [46]. Before tackling the problem of disorder, we give a short review on the analysis of homogeneous systems, with an emphasis on the tools and methods we will employ afterwards.

[2] The typical vibrational frequencies of adatoms or molecules range from roughly 10^{12} Hz to approximately 10^{14} Hz.

8.2.1 Analytical Results

As we want to concentrate on the effects of disorder, we analyze large systems with sufficiently high fluxes, thereby avoiding strong fluctuations produced by small grains, distorted lattices or small fluxes. While for the small grains a master equation or moment equations approach is necessary, the rate equation approach suffices for our purposes.

In the homogeneous system only one binding (and thus one hopping energy) is offered to the particles. The hopping and desorption rates are the same for all lattice sites and of the form (8.1)

$$\begin{aligned} W_s &= W = \nu\, \mathrm{e}^{-\frac{E_W}{T}}, \\ a_s &= a = \nu\, \mathrm{e}^{-\frac{E_a}{T}}\ . \end{aligned} \tag{8.7}$$

The dependence of the efficiency on the temperature $\eta(T)$ is known for this kind of system [41, 14] and illustrated together with the surface coverage in figure 8.3. The surface coverage — as the name suggests — is defined by the ratio $\theta = \langle N\rangle/S$, where $\langle N\rangle$ is the mean particle number in the system. The rate equation for the mean particle number $\langle N\rangle$ in this system reads

$$d_t\langle N\rangle = f(S - \langle N\rangle) - W\langle N\rangle - 2A\langle N\rangle^2 \tag{8.8}$$

where $A = a/S$ is the (approximated) sweeping rate[3] [76]. The terms on the right hand side correspond to gaining particles due to the constant influx on empty sites, losing particles by desorption and losing particles by reactions, respectively. The last term of the right-hand side shows the fundamental assumption of the rate equation approach: the reaction rate is proportional to the square of the mean number of the reactants and the discreteness as well as fluctuations of the particle number are neglected. Therefore,

$$R = A\langle N\rangle^2, \tag{8.9}$$

called reaction or production rate of the system, is *not* given by $A\langle N(N-1)\rangle$, which would be the correct average number of pairs in the system. Both expressions agree if and only if $\langle N^2\rangle - \langle N\rangle^2 = \langle N\rangle$, or in other words, if N is distributed according to the Poisson distribution. On small grains this equality of variance and mean is violated because the confinement of particles on the surface enhances the probability of two atoms to meet. In this work, we want to treat rate disorder and thus consider only large systems to exclude these other effects from the system. Therefore, we will abbreviate the notation by setting

$$N := \langle N\rangle, \tag{8.10}$$

so N now denotes the *average* particle number on the grain.

The efficiency of the system in the stationary state can then be computed via its definition

$$\eta \equiv \frac{2R}{fS} = 1 - \frac{(W+f)^2}{4fa}\left(\sqrt{1 + \frac{8fa}{(W+f)^2}} - 1\right), \tag{8.11}$$

[3] see 9.4.1 for a more detailed discussion on the choice of the sweeping rate in the presence of disorder

where the factor 2 in the definition accounts for the fact that two particles are needed to form one dimer. Qualitatively, at low temperatures, the particles are almost immobile (due to the temperature activated rates) and thus they do not meet other particles on the lattice. The coverage of the lattice is very high. With growing temperature, the hopping process becomes activated and particles can diffuse on the surface. This leads to more encounters and a rising efficiency. Increasing the temperature even more, the particles tend to desorb before they meet each other and so, the efficiency decreases, as well as the lattice coverage. The characteristic temperatures for the three regimes can be estimated within the rate equation approach [14]. Specifically,

$$T^{\text{low}} = \frac{E_a}{\ln(\nu/f)} \tag{8.12}$$

is the temperature derived from $f = a$, below which the particles arrive faster than they hop. A lot of particles are rejected by the LH mechanism and the efficiency of the system is low. At high temperatures

$$T^{\text{up}} = \frac{2E_W - E_a}{\ln(\nu/f)}, \tag{8.13}$$

determined by $f/W = W/a$, marks the characteristic value above which particles typically desorb before encountering another particle. So for $T > T^{\text{up}}$ the efficiency and the coverage are low. The temperature of maximum efficiency, determined by $f = W$, is given by the average of these two bounds and reads

$$T^{\max} = \frac{E_W}{\ln(\nu/f)}. \tag{8.14}$$

If the binding energy E_W is increased, the efficiency maximum is shifted towards higher temperatures, and the shift is directly proportional to the change in binding energy. The width of the efficiency peak $T^{\text{up}} - T^{\text{low}}$ stays the same, as it only depends on the (material-specific) difference $E_W - E_a$: For two equal lattices that are equipped either with binding energy E_{W_1} or E_{W_2} (differing by $\Delta E = E_{W_2} - E_{W_1}$), the temperatures of maximal efficiency are related via

$$T_2^{\max} = T_1^{\max} \cdot \left(1 + \frac{\Delta E}{E_{W_1}}\right). \tag{8.15}$$

In the next chapter we will begin to systematically introduce disorder into the system. We expect to obtain a much broader efficiency window, enabling a better alignment of model predictions and astrophysical observations.

For simplicity, we will always consider only one grain surface at a time and use the following expressions interchangeably throughout: particle/atom, dimer/molecule, surface/grain/lattice.

8.2.2 Kinetic Monte Carlo simulations

In [63], a code for Kinetic Monte Carlo (KMC) simulations was developed and presented. This code provides the basis for all simulations presented in this thesis. Therefore, we briefly review how it works.

As the Kinetic Monte Carlo (KMC) simulations serve as a reference for our analytical and numerical analysis, we need a thoroughly tested algorithm. We

use the standard algorithm as reviewed e.g. in [84], implemented by Lohmar [63]. In his thesis, he shows in detail how and that the code works as intended. Here, we concentrate on a review of the basic algorithm and the newly added features needed in the next chapters.

The standard KMC algorithm proceeds as follows: the particles are treated as continuous time random walkers with standard exponential waiting time distributions. In each step of the simulation, the possible elementary processes and their associated rates are evaluated from the current system configuration. Then a random number is drawn and compared to the normalized partial sums of the actual process rates. Thereby the process to be executed is determined. Then the simulation time is advanced by the inverse of the total sum of all rates and the system configuration is updated according to the process chosen by the random number.

The code is written in `Fortran95` and parallel computing of the simplest type is used. That is, for each set of parameters a separate job is started on one processor of the institute's high performance cluster, leading to the parallel simulation of up to 200 parameter sets.

The KMC simulations are tailored to handle disorder, as they keep track of every single particle and enable detailed modeling of the binding energy distribution. Especially for the simulations with quenched disorder, averaging out the realization dependence is an important issue. We handle this by averaging over enough realizations; typically 20 are sufficient. In addition to the nearest-neighbor hopping described above, another type of dynamics called 'longhop' dynamics is implemented. It is suited for comparison with the rate equation results: particles can not only hop to their neighboring sites, but to all sites of the lattice with equal probability (not distance dependent). This kind of dynamics switches off all spatial correlations between the sites and thus is best suited for a comparison with the rate equation results.

Furthermore, the energy landscapes are now generated separately from the simulations and are fed into the program. Thus, detailed modeling of the energy landscape and investigation of the spatial correlations is possible and will be made use of especially in chapters 9 and 11.

Chapter 9

Binary disorder in binding energies

As first step in our treatment of disordered surfaces, we start with the simplest form of rate disorder, realized by a binary binding energy distribution. Each lattice site corresponds to either a standard (shallow) site, or to a strong-binding (deep) site, with an enhanced binding energy. The homogeneous systems of either shallow or deep sites, show temperature windows of high efficiency that will typically be separated by a gap, as implied by the considerations of section 8.2.1. The natural question arising is, whether a system obtained by mixing these two types of sites still exhibits two separated efficiency peaks, or whether the efficiency is also high for intermediate system temperatures in-between the two peaks. If so, the next question would be, under which conditions this behavior occurs.

In this chapter, we first clarify the setting (section 9.1). In the following section 9.2 we provide a qualitative picture in which we identify three temperature regimes and describe the relevant processes for each of them. Then we give a systematic description and analysis of the extensive KMC simulations, which includes a study of spatial correlations in the (quenched) disorder in section 9.3. Afterwards, in section 9.4 we present a simple but accurate rate equation model and derive an expression for the efficiency in the interesting regime of intermediate temperatures.

9.1 Setting

Like described in chapter 8 the grain's surface is modeled by a quadratic grid with side lengths $L_1 = L_2 = L = \sqrt{S}$ and periodic boundary conditions. For the standard sites (or type-1 sites) we adopt the energy values of amorphous carbon [52]. We will vary the binding energy (and the hopping energy accordingly) of the second type of sites, the deep or type-2 sites, and to be consistent, the rates are still thermally activated like for the standard sites. Also here we want to ensure detailed balance on the surface such that the system can equilibrate for vanishing incoming particle flux. The simplest way to achieve this is by choosing

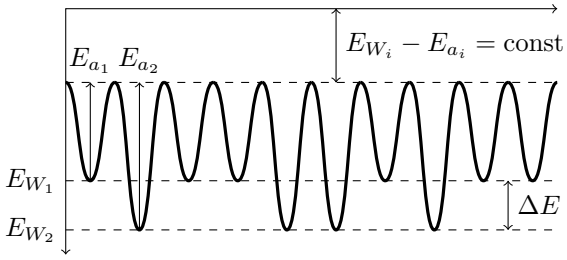

Figure 9.1: One-dimensional cut through the energy landscape of our model, as introduced in figure 8.2.

the rates according to (8.3)

$$W_1/a_1 = W_2/a_2 \tag{9.1}$$

which is equivalent to

$$E_{W_1} - E_{a_1} = E_{W_2} - E_{a_2} = \text{const}. \tag{9.2}$$

Then, the number of sites a particle visits before desorption becomes independent of the disorder. We imply $E_{W_2} > E_{W_1}$ throughout. A sketch of a one-dimensional cut (as introduced in figure 8.2) through such an energy landscape is depicted in figure 9.1.

Note that although we implemented detailed balance (the necessary property of systems in equilibrium) into the system on the level of binding and hopping rates, the whole system is *not* in equilibrium. Single particles enter the system by impinging on the lattice sites and leave the system either as single particles or — more importantly — as part of a molecule. Thus we have a net particle flow through the system. In the stationary state which we consider in this thesis, the particle influx and outflux are of same absolute value, so particles do not accumulate on the grain. In mathematical terms, this is called a system in non-equilibrium stationary state (NESS).

9.2 Qualitative Discussion

We consider the binary square lattice introduced in the last section 9.1 with the two binding energies E_{W_1} and E_{W_2}. The binding energies are assigned to the sites in a random way. For a particle on a shallow site, there is a typical length (number of hops) to reach a strong-binding site. This lengths obviously depends on the number of deep sites in the system and shortens when more of these sites are in the system. At low temperatures, around $T_1^{\max}$, particles can only diffuse on (and desorb from) shallow sites. A particle impinging on or hopping onto a deep site will not leave this site by hopping or desorption, since the binding energy is so high. Thus, recombinations can only take place on shallow sites, or on occupied deep sites, that have a neighboring shallow site from which particles can hop onto the deep site. At very high temperatures around $T_2^{\max}$, particles diffuse, desorb and recombine only on the deep sites, while particles on shallow sites desorb so quick, that no other process will take place. But at intermediate

temperatures $T_1^{\max} < T < T_2^{\max}$ this picture changes. Particles on deep sites are nearly immobile and do not desorb either, while particles on shallow sites tend to desorb too quickly to recombine on shallow sites. But if they find a deep site within their short range of exploration before desorbing, they are stuck on the surface and can recombine, if another particle hops onto this same site. So at intermediate temperatures, we expect the strong-binding sites to act as traps for the particles diffusing on the shallow sites. The random walk with traps has been studied extensively [66, 32]. To leading order, the number of steps a random walker has to perform before encountering a trap is given by

$$\langle n \rangle \approx \frac{1}{\pi} \frac{1}{S_2} S \ln S, \tag{9.3}$$

where S_2 is the total number of traps on a lattice with coordination number four and a total number of sites S. So the typical trapping length is

$$\ell_{\text{trap}} = \sqrt{\langle n \rangle}. \tag{9.4}$$

For a random walker on shallow sites, we find on the other hand a random walk length of [65]

$$\ell_{\text{rw}} = \sqrt{\frac{a_1}{W_1}} \tag{9.5}$$

before desorption. These two processes of trapping and desorption from shallow sites now compete with each other. While the former is a function of the number of traps (or deep sites), the latter is a function of the lattice temperature T. On average, for $\ell_{\text{rw}} > \ell_{\text{trap}}$, a particles is trapped before it can desorb. So we expect the trapping mechanism to be successful and to lead to a high efficiency of the system, up to the temperature, where both lengths are equal, given a fixed number of deep sites S_2.

Putting everything together, we find three temperature regimes. The low temperatures, where only particles on shallow sites are active, the intermediate temperatures, where particles behave like random walker on a lattice with traps, and the high temperatures, where particles become mobile on the deep sites. In the next step, we will check this picture by KMC simulations.

9.3 Kinetic Monte Carlo Simulations

In order to test our predictions, we carried out extensive kinetic Monte Carlo simulations.

For a given realization, we wait for the system to reach the steady state before we measure the efficiency over 10^6 impingements. We used a square lattice of $S = 100 \times 100$ sites. The flux per site is taken to be $f = 7.3 \times 10^{-9}$ s^{-1} [12], as explained before. We choose the standard attempt frequency $\nu = 10^{12}$ s^{-1}. With each site we associate either the standard binding energy $E_{W_1} = 658$ K, as found for hydrogen atoms on amorphous carbon [52], or an enhanced energy $E_{W_2} = E_{W_1} + \Delta E$ with $\Delta E = 250$, 750 or 1500 K. The activation energy for hopping reads $E_{a_1} = 511$ K or $E_{a_2} = E_{a_1} + \Delta E$, respectively.

For each case, we estimate the efficiency as function of the temperature $\eta(T)$ and as function of the relative frequency of deep sites $\eta(S_2/S)$. To learn more about the spatial influence of the efficiency, we do these calculations for up to

four different ways of distributing the binding energies among the lattice sites. For the case of nearest-neighbor hopping dynamics, we either assign the energies *randomly* to each site with the probabilities p_1 and $p_2 = 1 - p_1$, or we arrange the strong-binding sites in a regular *sublattice*, or we concentrate them in a single square *cluster*. The probabilities in the case of random assignment have to be understood in the sense, that S_2 is binomially distributed with parameter p_2. The resulting fluctuations of the individual realizations are eliminated by averaging over 20 realizations for every set of parameters considered. Therefore, in the following, we identify S_i/S with p_i. To compare with rate equations, that will be introduced in section 9.4, and have already been discussed in section 8.2.1 for the homogeneous system, we adopt another kind of dynamics, we will call the *'longhop'* case. Here, particles can hop from any site of the lattice to any other site, making the system effectively zero-dimensional and thereby switching off any spatial correlations. As rate equations do not account for spatial correlations, this simulation dynamic is best suited for a comparison.

Our KMC results are shown in figure 9.2. For each of the three different values of ΔE, we simulated systems with 1, 4, 10, 25 and 50% of strong-binding sites. In the case of random energy assignment (blue marks) — probably the most relevant case for applications — we see for each series of each value ΔE the predicted bridging of the intermediate temperature regime, as soon as the number of strong-binding sites is large enough. This is in accordance with the considerations of section 9.2, since the trapping length ℓ_{trap} has to be smaller than the random walk length ℓ_{rw} for all intermediate temperatures. For better visualization we also plotted T^{eq} (green bar), the temperature where $\ell_{\mathrm{rw}} = \ell_{\mathrm{trap}}$, and see, that as soon as $T^{\mathrm{eq}} > T_2^{\mathrm{max}}$, the efficiency is virtually constant for the intermediate temperatures. These observations hold at least up to $\Delta E = 3000$ K (figure 9.3), which is the largest value of ΔE that we have considered; beyond this energy scale one enters the regime of chemisorption, which is not our focus in this work.

The bigger the differences of the binding energies, the more strong-binding sites are needed to form a genuine plateau, where the efficiency does not depend on the temperature. This conforms to the ideas of Sec. 9.2; when the deep-site peak is shifted to higher temperatures, T^{eq} has to increase to warrant the formation of a plateau. This is achieved by increasing the deep-site fraction. The variance of the efficiency between different realizations of random landscapes was found to be negligible throughout. For the simulations with longhop dynamics, we found the efficiency to vary as much. As spatial correlations cannot play a role here, we conclude, that these fluctuations are entirely due to fluctuations in the absolute number of deep sites S_2 in every realization.

Still considering the nearest-neighbor hopping case, we find that the sublattice distributions performs slightly better than the random assignment. This is not astonishing since the sublattice optimizes the distance between the traps. In the random case, small clusters of strong-binding sites can occur, in which a single trap is less efficient. In an alternative picture we can say, that the capture zones of individual deep sites typically overlap, and the sublattice minimizes this overlap.

For the arrangement of all strong-binding sites into one single cluster, we find for all temperature and any frequency of deep sites no bridging any more. The performance gets even worse, when the system size is increased (cf. figure 9.4). For high frequencies of either shallow or strong-binding sites, only one restricted

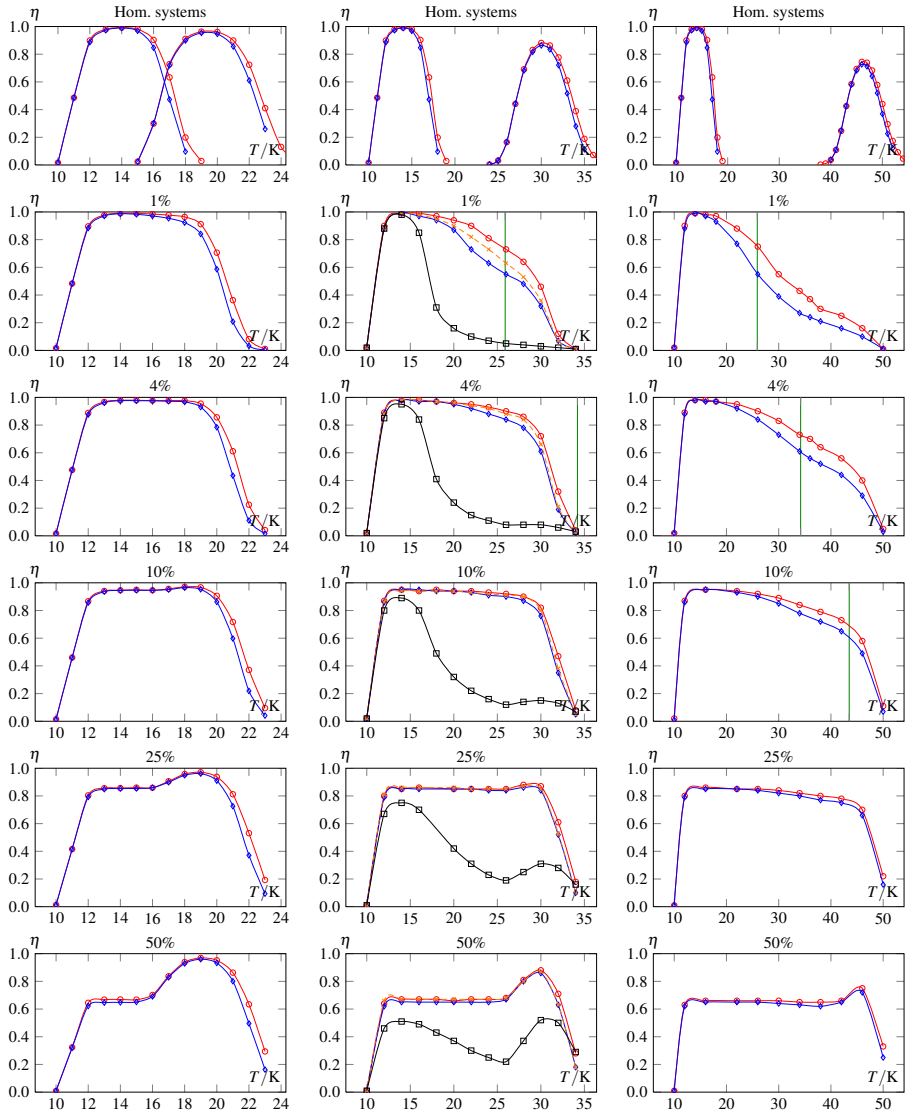

Figure 9.2: Efficiency versus temperature for various fractions of deep sites. Left column $\Delta E = 250$ K, middle $\Delta E = 750$ K, right $\Delta E = 1500$ K. Randomly assigned energies (blue line, diamonds), longhop dynamics (red line, circles). Only for $\Delta E = 750$ K: sublattice (orange dashed line, crosses), and cluster (black line, squares). Vertical green line at T^{eq}. The first row shows the results for homogeneous systems of only standard or only deep sites, respectively.

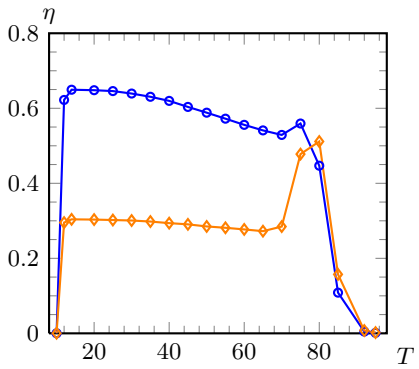

Figure 9.3: Simulation data with nearest-neighbor hopping: Efficiency as function of temperature for $\Delta E = 3000$ K. Shown are 50% of deep sites (blue, circles) and 80% of deep sites (orange, diamonds). The bridging still sets on, but a lot of deep sites are needed. This is in accordance with the results of sections 9.3.1 and 9.4.3.

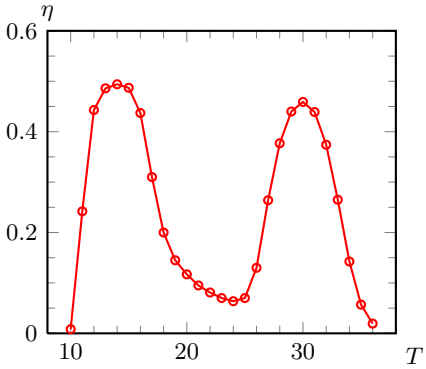

Figure 9.4: Simulation results for a cluster formation on a surface with $S = 500 \times 500$ sites and 50% of deep sites and $\Delta E = 750$K. In the intermediate temperature regime the efficiency nearly drops to zero and shows no "bridging" effect — in contrast to the well-mixed cases.

peak emerges, while for intermediate frequencies of strong and shallow sites two nearly separated peaks appear. This strongly indicates, that the hypothesis of the random walker on a lattice with traps scenario holds true. The efficiency does not drop to zero in the intermediate temperature regime, because an exchange between shallow and deep sites takes place along the boundary of the cluster. However, since the proportion of boundary length compared to the overall system size scales as $L/L^2 = \sqrt{S}^{-1}$, the fraction of boundary sites decreases with increasing S, and correspondingly the suppression of the efficiency in this regime becomes even more pronounced for larger systems. This is in contrast to the well-mixed case, where a finite fraction of sites are boundary sites (see below).

Considering now the longhop dynamics simulations, we first verified, that the simulation results are indeed independent of the way of distributing binding energies on the surface. Therefore we checked, that the results on the sublattice and a cluster landscape coincide. The efficiency under longhop dynamics outperforms even the sublattice results for nearest-neighbor hopping, where distances for the walkers are minimized. The reason lies in the finite probability to reach a trap in *every* hopping step. We will further analyze the longhop case when discussing rate equations in section 9.4.

9.3.1 Quantitative analysis of KMC results

In addition to our qualitative explanations, we analytically and numerically examine the dependence of the plateau efficiency value on the number of deep wells. First we note that for our choice of parameters, the efficiency value at $T_1^{\max} \approx 14$ K always corresponds to the plateau value. From the results for $\Delta E = 750$ K shown in figure 9.5 we infer that the way of distributing the

strong-binding sites is of crucial importance. In the case of a single square cluster of deep wells, the efficiency decreases linearly as $1 - S_2/S$, while for the random distribution the efficiency first decreases more slowly (for less than 50% of strong-binding sites) and faster to the end (more than 50%). We propose that this effect is related to the border length between shallow and deep sites, and use this connection to derive an empirical formula for the plateau efficiency.

First we present an analytical expression of the plateau efficiency for the case $S_2/S \ll 1$. Afterwards, we fit the simulation data to gain a results for all values of S_2/S.

The efficiency of the whole surface η is composed of three parts: the efficiency on the shallow sites η_{shallow}, on the deep sites η_{deep}, and on the border between shallow and deep sites η_{border}

$$\eta = \eta_{\text{shallow}} + \eta_{\text{deep}} + \eta_{\text{border}}. \tag{9.6}$$

At the temperature $T = 14K$, the deep sites are inactive in the sense that we can neglect hopping of atoms from a deep site, once they encountered one, so $\eta_{\text{deep}} = 0$. On the other hand, molecules are very effectively produced on shallow sites with an efficiency of $\eta_{\text{shallow}} = S_1/S = 1 - S_2/S$ since this is the fraction of the surface that is covered by shallow sites. This behavior is shown by the simulations on the cluster surface[1]. We are left with the calculation of the contribution from the border between shallow and deep sites. For randomly distributed deep wells, we calculate the border length L as function of S_2/S (cf. figure 9.6). We find a shallow site next to a deep site with probability $(S_2/S)(1 - S_2/S)$. Since the orientation of the pair does not matter, we gain an additional factor of 2. Furthermore we have $2S$ possibilities to place such a pair of sites on a square lattice with S sites and periodic boundary conditions. So we find the following expression for the border length between shallow and deep sites

$$L = 4S \cdot \frac{S_2}{S}\left(1 - \frac{S_2}{S}\right), \tag{9.7}$$

leading to a surface coverage of L/S. For calculation of the efficiency, this fraction has to be diminished by a factor of two, since only every second particle jumping on a deep site produces a molecule. Furthermore — assuming that the fraction of deep sites is sufficiently small — only one of four equally possible hopping processes leads to recombination on the border, so we arrive at $\eta_{\text{border}} = L/(2 \cdot 4 \cdot S)$

Summing up all terms, we obtain the total efficiency of the surface

$$\begin{aligned} \eta &= 1 - \frac{S_2}{S} + 0 + \frac{4SS_2/S(1 - S_2/S)}{8S} \\ &= \left(1 - \frac{S_2}{S}\right)\left(1 + \frac{S_2}{2S}\right) \\ &\approx 1 - \frac{S_2}{2S}, \end{aligned} \tag{9.8}$$

with approximation in first order of $S_2/S \ll 1$ This formula will also be derived from the rate equations model in section 9.4.3, thus confirming the above reasoning.

[1] the contribution from the border can be neglected in this case

For larger fractions of deep sites this argumentation has to be refined because with growing density the deep sites begin to compete for surface particles. This leads to an enhancement of the number of hopping processes at the border that result in molecule formation (more than one out of four hopping directions leads to recombination on the border), but more deep sites are surrounded by only other deep sites and thus do not contribute to the border length. So far, this factor can only be determined numerically. From the numerical examinations we know that the difference $\Delta\eta = \eta_{\text{random}} - \eta_{\text{cluster}} \equiv \eta_{\text{border}}$ is only due to the border between shallow and deep sites. The efficiency η_{border} constitutes of three factors, the ratio of border length to site number L/S, the ratio of hopping processes leading to molecule formation to the total number of hopping processes from shallow to deep sites $1/2$, and the ratio of the number hopping processes on the border to the number of all possible hopping processes $1/4$ (for a small fraction of deep sites). The only component of η_{border} changing with the fraction of deep sites is the ratio of hopping processes on the border compared to all possible hopping processes. When more deep sites are present on the grain, more than one out of four possible hopping directions leads to the encounter of a deep site, and the ratio of the two becomes bigger. By a numerical fit, we can gain information on that ratio. Fitting the efficiency difference $\Delta\eta$ to a multiple of the border length yields

$$\Delta\eta = C \cdot L, \tag{9.9}$$

with $C = (1.487 \pm 0.019) \times 10^{-5}$ or

$$\eta_{\text{random}} \approx \left(1 - \frac{S_2}{S}\right) \cdot \left(1 + (0.595 \pm 0.008)\frac{S_2}{S}\right) \tag{9.10}$$

for the empirical plateau efficiency value[2]. Now we can solve for the ratio of hopping directions on the border to all hopping directories, r_{p}, and find

$$r_{\text{p}} = 2SC = 0.2974 \pm 0.0038. \tag{9.11}$$

Comparing to the value of $1/4$ for the case $S_2/S \ll 1$, we find the predicted growth of r_{p} for larger values of S_2/S. This means very roughly, that on average 1.2 instead of only 1 out of the four hopping directions leads to a trapping of the particle on a deep site. As can be seen from figure 9.6, the fit is not perfect, so there is a variation in r_{p} with varying fraction S_2/S.

In addition to this fitting, we actually counted the border length for $125 \cdot 20 = 2500$ surfaces with varying fractions of deep sites between 0% and 100%. The analysis indeed showed that in

$$r_{\text{p}} \approx 0.366 \pm 0.006 \tag{9.12}$$

cases a hop from a shallow site results in an encounter of a deep site, which is quite close to the extrapolated value of 0.2974 ± 0.0038 from the numerical curve fitting (9.11).

This concludes the discussion of the KMC simulations. From the simulations and the qualitative and quantitative discussions, we have inferred the basic mechanisms, governing the behavior of a surface with binary disorder. In the next section we use rate equations to treat the system and gain further insight into details.

[2]The quality of the fit $\Delta\eta \propto L$ for KMC results underlines the role of the border length, and this corroborates our picture that the dominant reaction process on the plateau is by hopping from standard to deep sites.

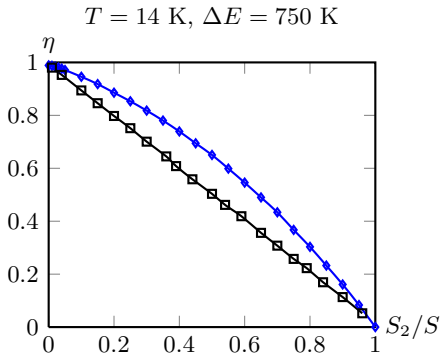

Figure 9.5: Efficiency as function of the deep-site fraction for $T = 14$ K and $\Delta E = 750$ K, for clustered deep sites (black, squares, η_{cluster}) and randomly assigned energies (blue, diamonds, η_{random}).

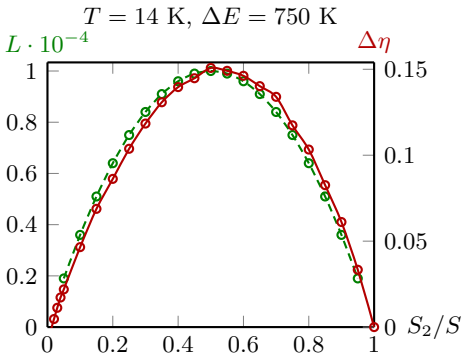

Figure 9.6: Border length L (green dashed line, left axis) and efficiency difference $\Delta\eta$ (dark red, right axis), as function of deep-site fraction. Vertical axis scaling taken from data fit.

9.4 Rate Equation Model

The applicability of a rate equation approach and its limits have already been discussed in section 8.2.

In previous work [22], KMC simulations on surfaces with varying roughness have been performed and a rate equation model was used to check the consistency of the landscape model with surfaces considered astrophysically relevant and examined in the laboratory.

We use this approach to support the findings of our KMC simulations and to deepen our qualitative understanding of the system's behavior and derive a set of equations for the total particle number N_i on each type of sites. The processes to be taken into account are, incoming flux on empty sites, desorption and reaction. While the first two can be written down straightforwardly, the reaction rates have to be determined carefully, since they are not an elemental process. We denote this so-far undetermined rate by A_i for sites of type i. The rate equations then take the form [69, 22]

$$\begin{aligned}\frac{\mathrm{d}N_1}{\mathrm{d}t} &= f(S_1 - N_1) - W_1 N_1 - A_1 N_1 (S_2 - N_2) - A_1 N_1 N_2 \\ &\quad - 2A_1 N_1^2 + A_2 N_2 (S_1 - N_1) - A_2 N_1 N_2, \\ \frac{\mathrm{d}N_2}{\mathrm{d}t} &= f(S_2 - N_2) - W_2 N_2 - A_2 N_2 (S_1 - N_1) - A_2 N_1 N_2 \\ &\quad - 2A_2 N_2^2 + A_1 N_1 (S_2 - N_2) - A_1 N_1 N_2.\end{aligned} \tag{9.13}$$

Here the first two contributions cater for the impingement flux with rejection and the desorption of particles. For clarity we separated the remaining terms. The next two terms describe leaving to a site of the opposite type (either to an empty or to an occupied site). Then we account for reactions inside one population due to hops between sites of the same type, removing two atoms. The remaining two contributions describe gaining a particle by a hop from the other site type, and finally, losing one particle due to the reaction with a particle coming from the other population.

It should be mentioned again that in the rate equation treatment, the total particle numbers N_i are continuous and especially can drop below unity. Thus, we must not replace the reaction term $2A_iN_i^2$ for 'homogeneous' reactions by the — on first sight more intuitive — term $2A_iN_i(N_i-1)$, as the reaction term then could become negative. As mentioned in the introductory section 8.2.1 for the homogeneous system and argued in detail in [89], the assumption that the reaction rate can be written as above is at the heart of the rate equation approach. Equations (9.13) are easily derived from the full master equation using this assumption in the forms $\langle N_i(N_i-1)\rangle \approx N_i^2$ and $\langle N_1N_2\rangle \approx N_1N_2$ (where the expectation is over the joint probability distribution $P(N_1,N_2)$ and the r.h.s. N_i's are already the mean values as above).

From the reaction terms, we can infer the recombination rate and efficiency of the system. Adding up all terms proportional to the A_i in $\mathrm{d}N/\mathrm{d}t = \mathrm{d}N_1/\mathrm{d}t + \mathrm{d}N_2/\mathrm{d}t$, pure hopping terms (not leading to a reaction) cancel. Accounting for the fact that each reaction consumes two particles, the rate with which particles are removed from the system by reaction amounts to

$$2R = 2A_1N_1^2 + 2A_2N_2^2 + 2(A_1+A_2)N_1N_2, \tag{9.14}$$

which can be simplified to $2R = 2(A_1N_1 + A_2N_2)(N_1+N_2)$. Relating this to the particle influx $f(S_1+S_2) = fS$ gives the efficiency $\eta = 2R/(fS)$.

9.4.1 The reaction rate coefficient

The reaction rate coefficient is a crucial quantity in all of the aforementioned approaches (master, rate and moment equations). Typically, it is approximated by the choice $A = a/S$ [76], also we adopt. This choice neglects back-diffusion and the competition between a reaction of particles and the prior desorption of one of the potential reactants. In [64, 65] a proper definition and evaluation of A was given and it was argued, that this choice should be implemented into all approaches, including rate equations. Nevertheless, we will stick with the choice $A = a/S$ throughout this work, since the situation with disorder is different. In all zero-dimensional approaches like master equation or rate equations, spatial structure cannot be included properly. When dealing with disorder and heterogeneous systems, there will be site type correlations that will be neglected *additionally* to the correlations in the particle residence probabilities. Then we have to assume, that a particle can reach any site from any other site within one hop, to be consistent. In particular, it hops to a site of type i with probability S_i/S, and it meets a particle on an i-site with probability N_i/S. The conventional choice $A_i \approx a_i/S$ thus arises naturally if we use rate equations to describe a system with site disorder, and we adopt this choice in the following. For a system with quenched spatial structure and nearest-neighbor hops only, this description corresponds most closely to the well-mixed case.

9.4.2 Comparison with KMC simulations

The rate equations (9.13) are exactly solvable at steady state by finding the real positive root of a third-order polynomial. However, the results are cumbersome and less than illuminating. We therefore directly opted for a numerical solver throughout.

Results on the validity of rate equations to describe the model in the homogeneous case have shown that confinement to a finite surface renders the discreteness of particles and fluctuations in the particle number important [81, 14, 56, 13, 64, 58]. Consequently, the mean-field approach of rate equations considerably overestimates the recombination efficiency in small systems.

In contrast, we find that the rate equations for the binary system reproduce the outcome of extensive KMC (longhop) simulations for a wide parameter range of practical relevance to excellent accuracy (see figure 9.7). The reasons for this slightly surprising result are as follows. First, since we present our results as functions of temperature and parameters are thermally activated, we typically have rather steep rises or declines. As noted in prior work [64], even factors of two or three in the efficiency do not have to appear substantial then. This hardly explains the observed accuracy in itself, especially on plateaus and moderate peaks for η considerably smaller than unity. Second, since we are interested in the behavior when there is a substantial number of particles in our system, the effects of discreteness and of fluctuations in this particle number are strongly reduced. Third, the confinement of particles to a finite surface is also far less important than for the homogeneous system, because the majority of these particles is trapped in deep wells in the regimes of most interest, anyway. Finally, we cannot preclude completely that differences might be more pronounced for smaller system sizes or activation energies of different type.

9.4.3 Plateau efficiency

One of the central questions of this chapter concerns the bridging of the two efficiency peaks belonging to the homogeneous systems of either type of sites. We found a convincing explanation of the occurrence of the plateau and the qualitative picture developed in section 9.3 also led to a crude estimation of the plateau efficiency, which we want to specify now. To arrive at an analytic expression comparably simple to equation (9.8), we need to simplify the full rate equation model using some observations: figure 9.7 shows that whenever a plateau emerges in the efficiency, practically all recombinations are due to hops between the two types of sites — as already argued in section 9.3. Only, when the concentration of deep sites is low and the efficiency is close to unity, the lower temperature end of the plateau also includes a substantial contribution from recombination on standard sites. At the high-temperature end of the efficiency window, any contribution from reactions on deep sites happens in the narrow temperature window around $T_2^{\max}$ and results in an efficiency peak additional to the plateau value.

To calculate the plateau efficiency by means of rate equations, we can therefore concentrate on the reaction between the two populations. With denoting standard sites by type 1, we can clearly state $A_1 \gg A_2$ and neglect all terms proportional to A_2 since they are small compared to their A_1 counterparts. But we keep all the flux and desorption terms. We clearly can leave out the reactions $A_2 N_1 N_2 \ll A_1 N_1 N_2$ and have to remove the hopping term $\propto A_2$ for consistency. Furthermore, we can neglect the homogeneous recombination (inside the N_i

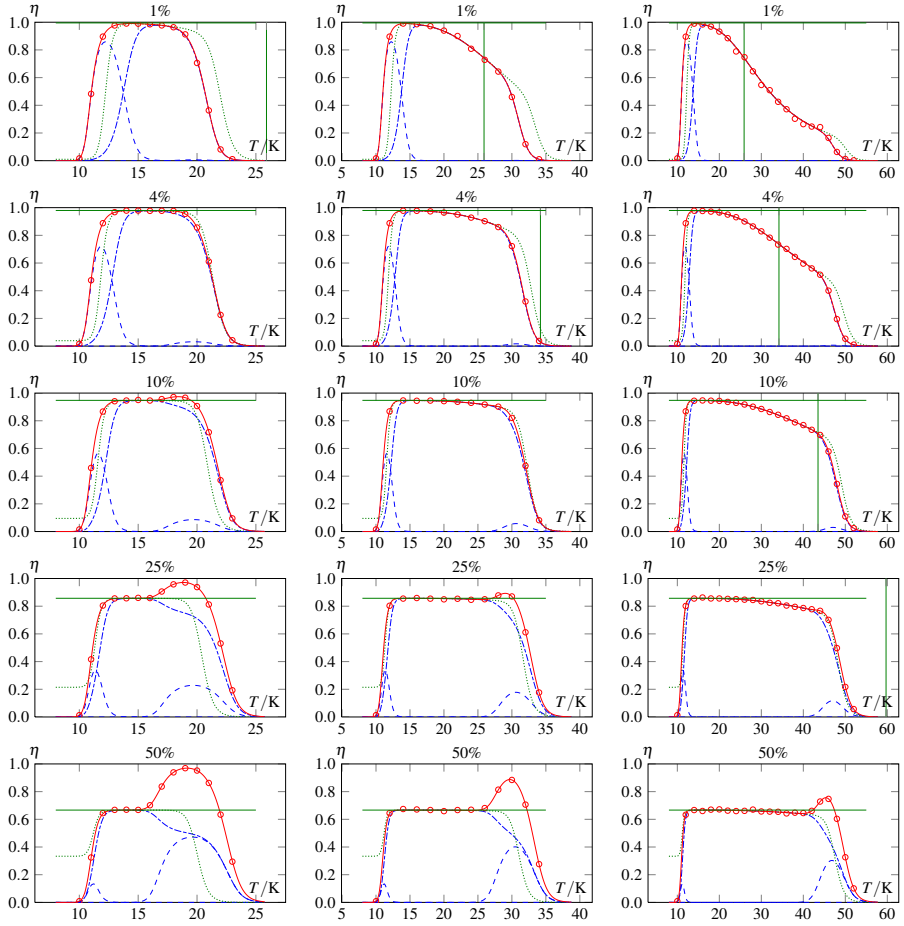

Figure 9.7: Efficiency versus temperature for various fractions of deep sites. Left column $\Delta E = 250$ K, middle $\Delta E = 750$ K, right $\Delta E = 1500$ K. Red circles: KMC longhop results (see section 9.3). Red lines the numerical solution of rate equations with standard $A_i = a_i/S$ (solid), blue lines contributions by reaction on the 1- and 2-sites (dashed), and by switching between the types (dot-dashed). Dotted green lines show the results of the plateau model (9.17), and green horizontal line the simple (9.18). Vertical green line at T^{eq}.

populations). This leads to the simplified steady-state equations

$$\begin{aligned} 0 &= f(S_1 - N_1) - W_1 N_1 - A_1 N_1 S_2, \\ 0 &= f(S_2 - N_2) - W_2 N_2 + A_1 N_1 S_2 - 2A_1 N_1 N_2, \end{aligned} \tag{9.15}$$

which yield an efficiency

$$\eta_\mathrm{p} = \frac{2A_1 N_1 N_2}{fS} = \frac{2fA_1 S_1 S_2 (V_1 + A_1 S)}{S(V_1 + A_1 S_2)[V_2(V_1 + A_1 S_2) + 2fA_1 S_1]}, \tag{9.16}$$

where $V_i = W_i + f$. Instead of directly evaluating this expression at a temperature right on the plateau, we notice that we can make two more assumptions in this case. We can neglect desorption from the type-2, so that $V_2 = f$, and together with $A_1 = a_1/S$, the simplified equation (9.16) reduces to

$$\eta_\mathrm{p} = \frac{2(S_1/S)(S_2/S)(1 + V_1/a_1)}{(V_1/a_1 + S_2/S)(1 + V_1/a_1 + S_1/S)}. \tag{9.17}$$

Then, $V_1/a_1 \ll S_2/S < 1$ holds on the plateau and for a reasonable fraction of deep sites S_2/S, yielding

$$\eta_\mathrm{p} \approx \frac{2}{S/S_1 + 1}. \tag{9.18}$$

This expression for the plateau efficiency does not depend on any energy scale and nicely agrees with equation (9.8) from the quantitative KMC analysis. The agreement with the simulations and the full rate equation results is excellent (cf. figure 9.7). This result is valid whenever conditions for plateau formation are fulfilled (i.e., if ΔE is large enough to separate the homogeneous-system peaks, and if there are enough deep wells if ΔE is fairly large).

We have to check the validity of the above made approximations. In Section 9.3 we found the peak temperature of the standard sites T_1^max to always belong to the plateau. By definition it does lie right beyond the low-temperature rise to the shallow site peak and yet this temperature is minimal enough not to be under an influence of the peak separation ΔE. At $T = T_1^\mathrm{max}$, $V_1 = W_1 + f = 2f$ and $V_2 = W_2 + f = f[(f/\nu)^{\Delta E/E_{W_1}} + 1]$. Reasonably, $f/\nu \ll 1$, while the smallest interesting $\Delta E \sim E_{W_1} - E_{a_1}$, such that the ratio $\Delta E/E_{W_1}$ is not excessively smaller than unity. This justifies the approximation $V_2 \approx f$, eliminating ΔE from the game, as suggested by figure 9.7. We now check the order of $V_1/a_1 = 2f/a_1 = 2(f/\nu)^{(E_{W_1} - E_{a_1})/E_{W_1}}$. The exponent is about 0.22 for amorphous carbon, and with the corresponding standard flux we have $V_1/a_1 \approx 6.3 \times 10^{-5}$ (cf. section. 9.3). This is negligible compared to any interesting deep-well fraction S_2/S ($\geq 1\%$), which completes the argument for equation (9.18). (We checked that this holds at least equally well for the standard olivine parameters [52].)

If we anticipate from the beginning, what terms can be neglected, this result can also be inferred from even further simplified rate equations. An intuitive explanation for the system's behavior is given in the following.

We consider the system in a steady state. So all particles entering the system, have to leave it. Entering the system can happen by impingement on a shallow or a deep site. Leaving the system only takes place on deep sites either by LH-rejection or by reaction with an incoming particle from a shallow site. So the rate at which particles from type-1 sites arrive at each type-2 site is given

by fS_1/S_2. Thus the rate at which particles leave from the type-2 sites at a rate $2fS_1/S_2 \cdot N_2$ since two particles are needed for each reaction. Alternatively, particles leave the system by LH-rejection (which can be considered as another desorption process on the level of rates) at a rate fN_2. The efficiency of the surface now is the fraction of particles leaving the system by reaction, normalized by the total rate of leaving the system (by LH-rejection or reaction). This yields

$$\eta_\mathrm{p} = \frac{2S_1}{2S_1 + S_2}, \tag{9.19}$$

which coincides with equation (9.18). We note that equation (9.19) can be rewritten as

$$\eta_\mathrm{p} = \frac{1 - S_2/S}{1 - S_2/(2S)} \approx \left(1 - \frac{S_2}{S}\right)\left(1 + \frac{S_2}{2S}\right) \tag{9.20}$$

for $S_2/S \ll 1$, which then results in precisely the form of the empirical relation (9.8).

9.5 Conclusions

In this chapter we studied a lattice with a binary binding energy distribution and its influence on dimer formation from single particles impinging the surface. The mixing of the shallow and deep sites leads to a high efficiency even in regions where the corresponding homogeneous systems do not perform well at all. We explicitly identified the mechanism supporting the high efficiency in this intermediate temperature region, namely shallow sites catering for particle mobility and funneling the particles into the deep sites that act as particle traps and thus facilitate molecule formation. The identification was done by comparing KMC simulations of surfaces with well-mixed types of sites to surfaces with the same amounts of each type of site but deep sites arranged in a cluster, thereby minimizing the border between shallow and deep sites, leading to a significant reduction of the efficiency in the intermediate temperature regime (section 9.3). The (numerical) rate equation solutions (section 9.4) corroborate this picture. Our findings nicely coincide with the model predictions of [19], who observed the formation of hydrogen on a surface with physisorption and chemisorption sites and found that for high temperatures the dominant process is $\mathrm{H}_\mathrm{chemis.} + \mathrm{H}_\mathrm{chemis.} \rightarrow \mathrm{H}_2$ while for low temperatures (physisorbed atoms still mobile) $\mathrm{H}_\mathrm{physis.} + \mathrm{H}_\mathrm{chemis.} \rightarrow \mathrm{H}_2$ dominates. As the mechanism leading to the enhancement of the temperature window of high efficiency is quite fundamental, we expect it to hold true also for other distributions of binding energies, which we will turn to in the next two chapters.

Chapter 10

Discrete distributions of binding energies

In view of possible applications it is useful to understand not only systems with binary disorder but discrete distributions in general. Different types of materials forming a grain surface, as well as surface features like steps, corners and holes, will automatically lead to some kind of discrete binding energy distribution.

With the central result of the former chapter in mind, we now consider discrete binding energy distributions, starting with a ternary system. For the analysis, rate equations and KMC simulations are used in the same spirit as before. We will discover the mechanism identified in the binary disorder case of sites either serving as traps or providing particle mobility on the surface, to be of central importance again. Later on in chapter 11 we will introduce a mapping from continuous distributions to an effective binary system and apply this mapping also to general discrete binding distributions. We start with a treatment of the ternary system by means of rate equations in section 10.1.1. Our findings are confirmed by KMC simulations in section 10.1.2. Finally we extend the results of the ternary system to discrete binding energy distributions with arbitrarily many types of sites in section 10.2 and discuss the limits of this approach in section 10.3.

10.1 Mapping of a ternary to a binary system

In chapter 9 we showed how the simplest case of disorder in the binding energies influences the efficiency of this surface in dimer formation. For reasons we will identify in the analysis of the ternary system, the results can be extended to systems with a finite but arbitrarily large number of binding energies types under quite general constraints. The general procedure for analyzing the ternary system will be the same as for the binary system (chapter 9), involving rate equations, effective rate equations and KMC simulations.

We extend the binary system by another kind of site with binding energy E_{W_3} and hopping energy E_{a_3}, still satisfying the condition for detailed balance $E_{W_i} - E_{a_i} = E_{W_j} - E_{a_j}$, $i, j = 1, 2, 3$. The total number of sites S now is made up by three parts: $S = S_1 + S_2 + S_3$. Without loss of generality we arrange the binding energies in such a way that $E_{W_1} < E_{W_2} < E_{W_3}$, and refer to them as

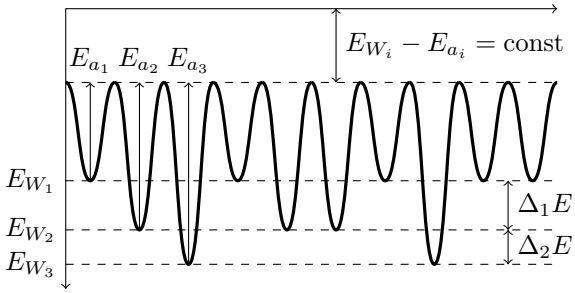

Figure 10.1: One-dimensional cut through the energy landscape of the three-type model, as indicated in 8.2.

'shallow', 'intermediate', and 'deep' sites, or type-1, -2, or -3 sites, respectively. A one-dimensional cut through such an energy landscape is sketched in figure 10.1.

10.1.1 Rate equations

From the qualitative discussion in section 9.2, we know what happens at the border between two sites with different binding energies at a given surface temperature. Either atoms are mobile or immobile on both types of sites, or — and that is the interesting case when $T_i^{\max} < T < T_{i+1}^{\max}$ — atoms are mobile on one type and immobile on the other. In the latter case, we have again the situation of a random walker on a lattice with traps. We analyzed this situation qualitatively and quantitatively in section 9.3.1 for the case of two different binding energies. Now we investigate the situation with three binding energies. This implies that type-2 sites must be considered as either shallow or deep — providing either mobility or trapping — depending on the temperature, while type-1 sites are always shallow (providing mobility) in the interesting temperature regime and type-3 sites always act as deep sites (trapping particles).

Following the argumentation in section 9.4 we find for the surface with three types of binding energies the following set of rate equations:

$$\begin{aligned}
\frac{\mathrm{d}N_1}{\mathrm{d}t} &= f(S_1 - N_1) - W_1 N_1 - A_1 N_1 (S_2 - N_2) - A_1 N_1 (S_3 - N_3) \\
&\quad - A_1 N_1 N_2 - A_1 N_1 N_3 - 2A_1 N_1^2 + A_2 N_2 (S_1 - N_1) \\
&\quad + A_3 N_3 (S_1 - N_1) - A_2 N_1 N_2 - A_3 N_1 N_3, \\
\frac{\mathrm{d}N_2}{\mathrm{d}t} &= f(S_2 - N_2) - W_2 N_2 - A_2 N_2 (S_1 - N_1) - A_2 N_2 (S_3 - N_3) \\
&\quad - A_2 N_1 N_2 - A_2 N_2 N_3 - 2A_2 N_2^2 + A_1 N_1 (S_2 - N_2) \\
&\quad + A_3 N_3 (S_2 - N_2) - A_1 N_1 N_2 - A_3 N_2 N_3, \\
\frac{\mathrm{d}N_3}{\mathrm{d}t} &= f(S_3 - N_3) - W_3 N_3 - A_3 N_3 (S_1 - N_1) - A_3 N_3 (S_2 - N_2) \\
&\quad - A_3 N_1 N_3 - A_3 N_2 N_3 - 2A_3 N_3^2 + A_1 N_1 (S_3 - N_3) \\
&\quad + A_2 N_2 (S_3 - N_3) - A_1 N_1 N_2 - A_2 N_2 N_3.
\end{aligned} \tag{10.1}$$

The structure of the equations is the same as in the binary case, but we have to account for hopping from and to two other types of sites for each site type.

Again, for transparency, we separated the hopping terms into hopping onto an empty site and hopping onto an occupied site (of either type). The mere hopping terms without reaction cancel upon addition of all three equations.

Solving for the stationary state, $\mathrm{d}N_i/\mathrm{d}t = 0$, we distinguish two temperature regimes in which we expect non-trivial behavior of the efficiency: $T_1^{\max} < T < T_2^{\max} < T_3^{\max}$ and $T_1^{\max} < T_2^{\max} < T < T_3^{\max}$.

- Case 1: $T_1^{\max} < T < T_2^{\max}$
  According to section 9.4, in the rate equation approach, we can neglect all terms proportional to A_2, A_3, W_2 and W_3, since the temperature is too low to allow hopping and single-particle desorption from the intermediate and deep sites. Also we assume $T > T_1^{\mathrm{up}}$ such that we can neglect homogeneous reaction terms $\propto N_1^2$ on shallow sites. Then the stationary rate equations are given by

$$\begin{aligned} 0 &= f(S_1 - N_1) - W_1 N_1 - A_1 N_1 (S_2 + S_3), \\ 0 &= f(S_2 - N_2) - W_2 N_2 + A_1 N_1 S_2 - 2A_1 N_1 N_2, \\ 0 &= f(S_3 - N_3) - W_3 N_3 + A_1 N_1 S_3 - 2A_1 N_1 N_3. \end{aligned} \tag{10.2}$$

  As the structure of the type-2 and type-3 equations is equal, we combine them to yield

$$\begin{aligned} 0 &= f(S_1 - N_1) - W_1 N_1 - A_1 N_1 (S_2 + S_3), \\ 0 &= f(S_2 + S_3 - (N_2 + N_3)) + A_1 N_1 (S_2 + S_3) \\ &\quad - 2A_1 N_1 (N_2 + N_3). \end{aligned} \tag{10.3}$$

  Now we rename $N_1 = N_{1,\mathrm{eff}}$, $N_2 + N_3 = N_{2,\mathrm{eff}}$, $S_1 = S_{1,\mathrm{eff}}$, $S_2 + S_3 = S_{2,\mathrm{eff}}$, and $A_1 = A_{1,\mathrm{eff}}$, leading to the two effective equations

$$\begin{aligned} 0 &= f(S_{1,\mathrm{eff}} - N_{1,\mathrm{eff}}) - W_1 N_{1,\mathrm{eff}} - A_{1,\mathrm{eff}} N_{1,\mathrm{eff}} S_{2,\mathrm{eff}}, \\ 0 &= f(S_{2,\mathrm{eff}} - N_{2,\mathrm{eff}}) + A_{1,\mathrm{eff}} N_{1,\mathrm{eff}} (S_{2,\mathrm{eff}}) - 2A_{1,\mathrm{eff}} N_{1,\mathrm{eff}} N_{2,\mathrm{eff}}. \end{aligned} \tag{10.4}$$

  Comparing this set of equations to the rate equations of the binary system (9.15), we find that the structure is identical. Therefore, we can use the solutions of the binary disorder case (for the plateau regime)

$$\begin{aligned} N_{1,\mathrm{eff}} &= \frac{f S_{1,\mathrm{eff}}}{V_{1,\mathrm{eff}} + A_{1,\mathrm{eff}} (S - S_{1,\mathrm{eff}})} \\ N_{2,\mathrm{eff}} &= (f + A_{1,\mathrm{eff}} N_{1,\mathrm{eff}}) \left(\frac{S_{2,\mathrm{eff}}}{V_{2,\mathrm{eff}} + 2A_{1,\mathrm{eff}} N_{1,\mathrm{eff}}} \right). \end{aligned} \tag{10.5}$$

  Inserting these effective expressions into the definition of the efficiency η, we find

$$\eta_{\mathrm{p}} = \frac{2}{S/S_{1,\mathrm{eff}} + 1}, \tag{10.6}$$

  where $S = S_{1,\mathrm{eff}} + S_{2,\mathrm{eff}} = S_1 + (S_2 + S_3)$ and sufficiently many (effectively) deep sites $S_{2,\mathrm{eff}}$ are assumed to be present on the surface. Thus we find the bridging effect also occurs in the ternary system, which is not astonishing as such. Also the combination of all sites of type i with $T_i^{\max} > T$ to one

effective type of site with the energy parameters of the original intermediate sites,

$$\begin{aligned} E_{\text{eff},W_2} = E_{W_2} &= \min_{\{i:T_i^{\max}>T\}} E_{W_i}, \\ E_{\text{eff},a_2} = E_{a_2} &= \min_{\{i:T_i^{\max}>T\}} E_{a_i}, \end{aligned} \tag{10.7}$$

seems natural, as on the sites considered deep in comparison with the system temperature, virtually no dynamic processes happen. The type-2 and type-3 sites act effectively in the same way, independent of their exact binding energy.

- Case 2: $T_2^{\max} < T < T_3^{\max}$
  Here, we can only neglect contributions proportional to A_3 and W_3, since only on these deep sites particles are trapped. But since now particles on type-1 *and* type-2 sites are highly mobile and tend to desorb very fast, we also can neglect terms proportional to N_1^2,N_2^2 and N_1N_2, yielding the following simplified stationary rate equations:

$$\begin{aligned} 0 &= f(S_1 - N_1) - W_1N_1 - A_1N_1(S_2 + S_3) + A_2N_2S_1, \\ 0 &= f(S_2 - N_2) - W_2N_2 - A_2N_2(S_1 + S_3) + A_1N_1S_2, \\ 0 &= f(S_3 - N_3) - W_3N_3 + (A_1N_1 + A_2N_2)S_3 \\ &\quad - 2(A_1N_1 + A_2N_2)N_3, \end{aligned} \tag{10.8}$$

where now the first and second equation are of the same structure. The solutions read

$$\begin{aligned} N_1 &= \frac{fS_1(V_2 + A_2S)}{(V_2 + A_2(S - S_2))(V_1 + A_1(S - S_1)) - A_1S_1A_2S_2}, \\ N_2 &= \frac{fS_2(V_1 + A_1S)}{(V_2 + A_2(S - S_2))(V_1 + A_1(S - S_1)) - A_1S_1A_2S_2}, \\ N_3 &= \frac{fS_3 + S_3(A_1N_1 + A_2N_2)}{f + 2(A_1N_1 + A_2N_2)}. \end{aligned} \tag{10.9}$$

Next we apply the approximations $V_1/a_1 \ll (S - S_1)/S < 1$, $V_2/a_2 \ll (S - S_2)/S < 1$ introduced in section 9.4.3 and valid for any reasonable amount of intermediate and deep sites to find

$$\begin{aligned} N_1 &\approx \frac{fS_1}{a_1(1 - (S - S_3)/S)}, \\ N_2 &\approx \frac{fS_2}{a_2(1 - (S - S_3)/S)}, \\ N_3 &\approx \frac{fS_3 + S_3/S(a_1N_1 + a_2N_2)}{f + 2/S(a_1N_1 + a_2N_2)}. \end{aligned} \tag{10.10}$$

At this point we rename

$$\begin{aligned} a_{1,\text{eff}}N_{1,\text{eff}} &= a_1N_1 + a_2N_2, \\ N_{2,\text{eff}} &= N_3, \\ S_{1,\text{eff}} &= S_1 + S_2, \\ S_{2,\text{eff}} &= S_3, \end{aligned} \tag{10.11}$$

identify $a_2 \equiv a_{1,\text{eff}}$, and express N_1 by N_2 using equation (10.10),

$$N_1 = \frac{a_2 S_1}{a_1 S_2} N_2. \tag{10.12}$$

We find for the effective shallow and deep sites

$$\begin{aligned} N_{1,\text{eff}} &= \frac{a_1}{a_2} N_1 + N_2 = \left(\frac{a_1 a_2 S_1}{a_2 a_1 S_2} + 1 \right) N_2 \\ &= \frac{S_1 + S_2}{S_2} N_2 = \frac{fS}{a_{1,\text{eff}}} \left(\frac{S}{S_3} - 1 \right), \\ N_{2,\text{eff}} &= \frac{S}{1 + 2(S/S_{2,\text{eff}} - 1)}. \end{aligned} \tag{10.13}$$

Now we can calculate the efficiency of this effective binary system:

$$\begin{aligned} \eta &= \frac{2R}{fS} = \frac{2 a_{1,\text{eff}} N_{1,\text{eff}} N_{2,\text{eff}}}{fS} \\ &= \frac{2}{1 + S/(S - S_3)}. \end{aligned} \tag{10.14}$$

Remembering that $S_{2,\text{eff}} = S_3$ and $S_{1,\text{eff}} = S_1 + S_2$, we recover again the plateau formula (9.18) of the binary system, now with $S_1 + S_2$ sites of binding energy $E_{W_1,\text{eff}} = E_{W_2}$ and S_3 sites of binding energy $E_{W_2,\text{eff}} = E_{W_3}$ as we can read off the nature of the effective shallow particles and sites from equation (10.12): the number of effectively shallow sites $N_{1,\text{eff}}$ is given by the number of original shallow and intermediate sites $S_1 + S_2$ multiplied by the density of particles on the intermediate sites $n_2 = N_2/S_2$. So it is clear why the effective shallow sites inherit their energy parameters from the intermediate sites. Their (average) number $N_{1,\text{eff}}$ is calculated by merging the original number of shallow sites to the intermediate ones and assuming that on these sites all particles act like on type-2 sites.

Thus, we can give a simple recipe, how to determine the recombination efficiency in a system with ternary disorder. Throughout, we have to assume that for all three types of sites, there are reasonable amounts present in the system. The idea of this mapping is depicted in figure 10.2. First, we determine how the temperature T relates to the temperatures of the efficiency maxima of the homogeneous systems $T_i^{\max}$ (corresponding to the binding energies present in the system). Then we add up all sites S_i with $T_i^{\max} < T$ and $T_i^{\max} > T$, respectively. In terms of energies this corresponds to a cutting of the binding energy distribution at the temperature-dependent cutting energy $E_{\text{cut}} = T \ln(\nu/f)$. To these two numbers of sites, called $S_{1,\text{eff}}$ and $S_{2,\text{eff}}$, the titles 'effectively shallow' and 'effectively deep' are assigned, respectively, and the binding energies of the two types are determined as follows. For the effectively shallow sites we determine the largest of the binding energies present in the group of sites that form the effectively shallow sites. For the effectively deep sites, we determine the smallest of the binding energies and assign these binding (and hopping) energies to the effective types of sites. Then we have a binary system and apply our knowledge from the last chapter 9. For the plateau formula to hold, the condition for plateau formation in the effective binary system has to be fulfilled, as discussed in 9.3.1 and 9.4.3, of course.

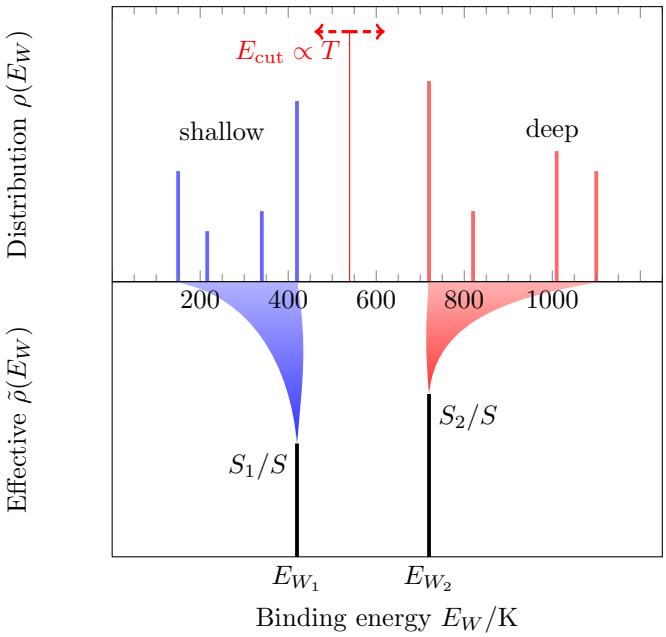

Figure 10.2: Idea of the mapping from the original system with discrete binding energies to an effective binary system. The translation between the temperature T and energies E_W is performed on the binding energy level: $E_{\mathrm{cut}} = T\ln(\nu/f)$ and we have to account for the regimes of validity as will be discussed in section 10.3 .

Combining the presented arguments and reasoning, we conclude that the binary system already shows all relevant mechanisms needed for explaining the observed recombination efficiency in the ternary system. Moreover, the recipe found above suggests its application to arbitrary discrete distributions of binding energies.

10.1.2 Kinetic Monte Carlo simulations

To complete and corroborate the picture of the rate equation approach, we performed KMC simulations of the full ternary system and of the effective binary system derived in the previous section 10.1.1. For the simulations we consider randomly distributed sites in the sense explained above, fixing the relative frequency of each kind of site and drawing the energies of sites randomly, according to this frequency. Additionally we mainly use 'longhop' dynamics in the KMC simulations for comparison with rate equations, as the influence of site arrangement has been studied extensively in the last chapter and is not covered by the rate equation approach.

According to the results of the rate equation approach, we find in the ternary system two temperature regimes of interest, $T_1^{\max} < T < T_2^{\max}$ and $T_2^{\max} < T < T_3^{\max}$. For these two regimes we find two different effective binary systems. In the first case we obtain the effective model by regarding the sites of type 3 as type-2 sites to form the effectively deep sites. The effectively shallow sites are identical to the original type-1 sites. In the second case we find the effective binary system by regarding the type-1 sites to type-2 sites and adding

them to the type-2 sites. The effectively deep sites consist of the type-3 sites.

For the simulations we used one ternary distribution with equally spaced site types of $\Delta_1 E = \Delta_2 E = 750\,\mathrm{K}$ and one distribution with $\Delta_1 E = 1000\,\mathrm{K}$ and $\Delta_2 E = 500\,\mathrm{K}$. For better comparison with the former results, we adopt the energy values of amorphous carbon for the shallow sites ($E_{W_1} = 658\,\mathrm{K}$, $E_{a_1} = 511\,\mathrm{K}$). The total number of sites on the quadratic square lattice with periodic boundary conditions is $S = 10000$. Now we have two parameters for fixing the amounts of sites of the different types of sites. We handle this for the plots by fixing, e.g., the number of shallow sites and varying the number of intermediate and deep sites, and vice versa. The frequencies of effectively deep sites are chosen such as to produce both, systems that reveal a full bridging and systems that do not have enough deep sites to show a full peak bridging.

First of all, in figure 10.3 we show that the simulation results with longhop dynamics and the numerical rate equation results coincide nicely for the full ternary system. From the figures 10.4 and 10.5 we see that for the lower and the higher temperature regime, the effective binary system reproduces the efficiency of the full ternary system almost perfectly. The temperature regimes considered are highlighted by the light green background color. The very pale regimes together with the more intense ones visualize the intervals $T_i^{\max} < T < T_{i+1}^{\max}$, while the smaller more intense color bars refer to the regime $T_i^{\max} < T < T_{i+1}^{\mathrm{low}}$. Additionally in figure 10.5 we show that indeed, in the regime $T_i^{\max} < T < T_{i+1}^{\mathrm{low}}$, the efficiency of the effective binary system reproduces the efficiency of ternary systems, as long as the numbers of sites for the effectively deep and shallow sites are matched. The distribution of these numbers of sites among the different binding energies does not play any role.

10.2 n types of binding energies

The simulations and rate equation results in the last section strongly suggest that the systematics of combining sites with a homogeneous system maximal temperature $T_i^{\max}$ smaller and larger than the actual system temperature T to an effective binary system also works for systems with $n > 3$ types of binding energies. Due to the generic structure of the reduced effective rate equations, the number of different binding energies does not affect the results. We now construct the mapping from a system with n different binding energies to an effective binary system for a given system temperature. The total number of sites is $S = \sum_{i=1}^{n} S_i$, the corresponding binding and hopping energies are given by E_{W_i} and E_{a_i}, and the temperature of maximal efficiency in a homogeneous system with sites of type i reads $T_i^{\max}$. For system temperature T the rate equations for the types of sites with $T_i^{\max} < T$ read

$$0 = f(S_i - N_i) - W_i N_i - A_i N_i (S - S_i) + S_i \sum_{j \neq i : T_j^{\max} < T} A_j N_j. \qquad (10.15)$$

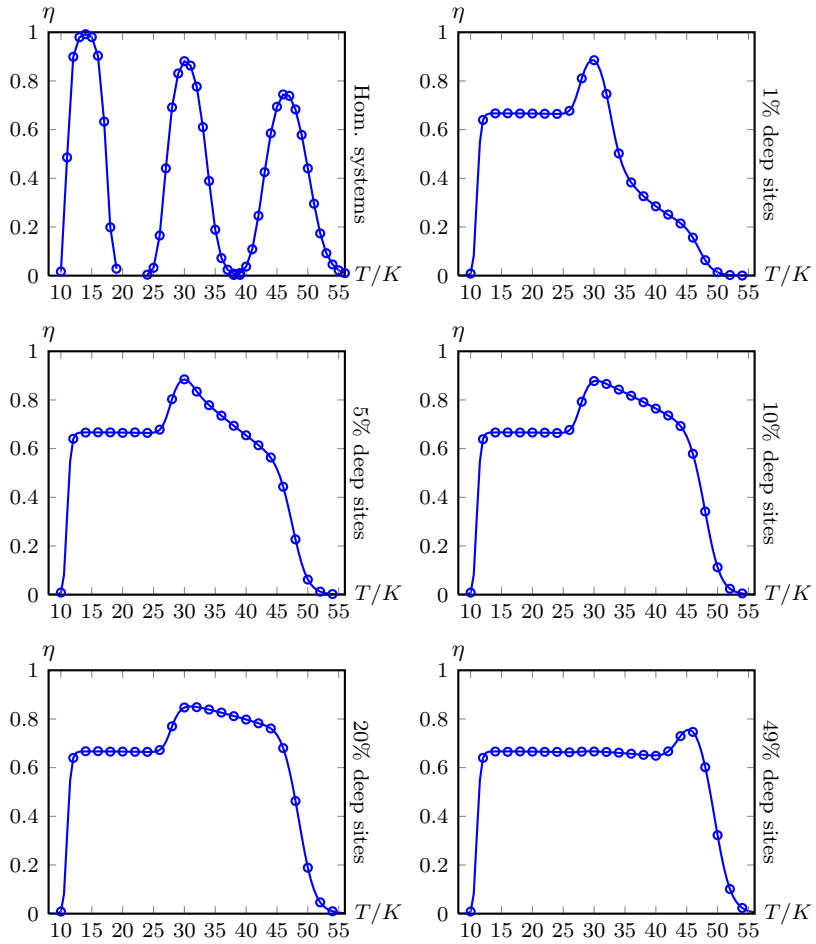

Figure 10.3: Comparison of KMC simulations with 'longhop dynamics' (open circles) and numerical solutions of the full rate equations (10.8) (solid lines) for a surface with three types of binding energies and 50% shallow sites. The number of deep sites is varied from 1% over 5%, 10%, 20%, to 49%, and the number of intermediate sites varies accordingly. The total number of sites is $S = 10000$, and the parameters chosen are the ones for H atoms on an amorphous carbon surface. The other binding energies are $E_{W_2} = E_{W_1} + 750K$, and $E_{W_3} = E_{W_1} + 1500K$, and $E_{W_i} - E_{a_i} = \text{const}$. We used the 'longhop' dynamics to generate the numerical data. As reference we also shown the efficiency curves of the three corresponding homogeneous systems in the upper leftmost of the pictures, as also displayed in figure 9.2.

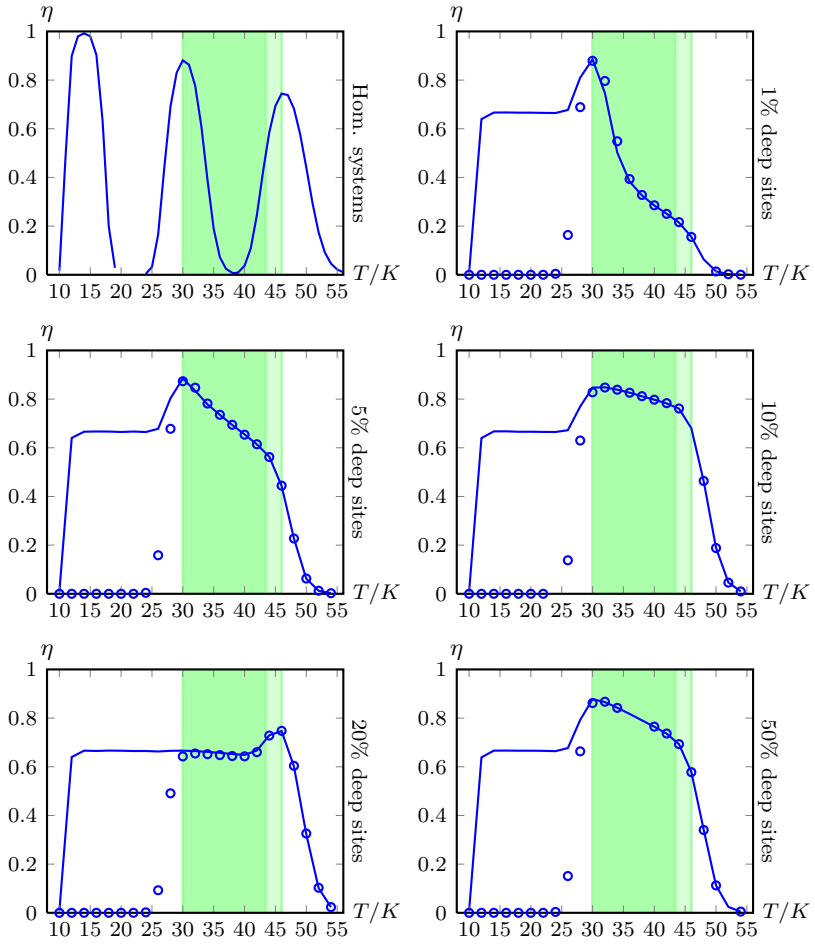

Figure 10.4: Simulation results for the temperature dependence of the efficiency of the full system (as in figure 10.3) with KMC 'longhop' dynamics (solid line) and the simulation results of the effective binary system. In the effective system the amount of shallow sites is added to the intermediate sites and give the amount of shallow sites in the effective system with the binding energy of the former intermediate sites. This simple comprising is valid for system temperatures between $T_2^{\max} < T < T_3^{\max}$ in terms of the original system (open circles). This temperature region is indicated by the light green color area in the plots. The frequency of shallow sites in the full system is kept at 50% which fixes the number of intermediate sites, while the (varying) frequency of deep sites is indicated for each of the plots. The binding energies of the three types are chosen as 658K, 1408K and 2158K for the shallow, intermediate and deep sites, respectively. All other parameters are chosen according to the standard values used so far.

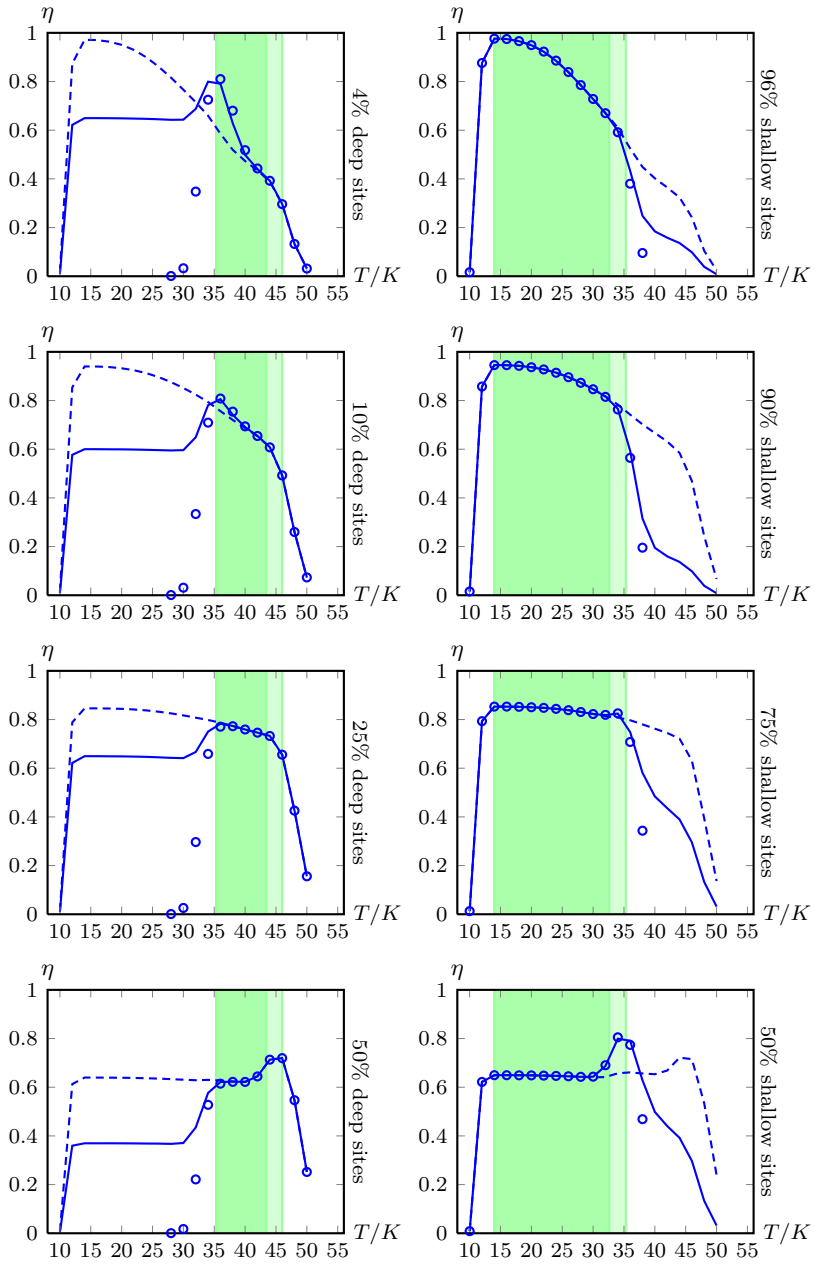

Figure 10.5: Efficiency of the full ternary and the effective binary systems. The greenish regions mark the temperatures for which the effective system is deduced. The intensely green region refer to temperatures $T_i^{\max} < T < T_{i+1}^{\text{low}}$ and the intense together with the pale region refers to $T_i^{\max} < T < T_{i+1}^{\max}$. The binding energies are: $E_{W_1} = 658$ K, $E_{W_2} = 1658$ K, and $E_{W_3} = 2158$ K. Open circles: KMC simulations of effective binary system. Left column: Solid lines: KMC simulations of the full ternary system with frequencies $(0.5, 0.45, 0.04)$, $(0.45, 0.45, 0.1)$, $(0.5, 0.25, 0.25)$, $(0.25, 0.25, 0.5)$ of type-1, -2, and -3 sites, respectively, from top to bottom. Dashed lines: KMC simulations of the full ternary system with frequencies $(0.95, 0.01, 0.04)$, $(0.89, 0.01, 0.1)$, $(0.74, 0.01, 0.25)$, $(0.49, 0.01, 0.5)$. Right column: Solid lines: KMC simulations of the full ternary system with frequencies $(0.96, 0.00, 0.04)$, $(0.96, 0.00, 0.1)$, $(0.96, 0.00, 0.25)$, $(0.96, 0.00, 0.5)$. Dashed lines: $(0.96, 0.01, 0.03)$, $(0.90, 0.01, 0.09)$, $(0.75, 0.01, 0.24)$, $(0.5, 0.01, 0.49)$. We stress, that the data displayed by lines is also obtained from 'longhop' simulations for discrete temperatures with a step widths of $\Delta T = 2$.

We combine the types of sites with $T_i^{\max} < T$ to the effective shallow sites and assign to them the binding and hopping energies

$$\begin{aligned} E_{W_1,\text{eff}} &= \max_{\{i:T_i^{\max}<T\}} E_{W_i} \\ E_{a_1,\text{eff}} &= \max_{\{i:T_i^{\max}<T\}} E_{a_i} \\ S_{1,\text{eff}} &= \sum_{i:T_i^{\max}<T} S_i \end{aligned} \tag{10.16}$$

where $S_{1,\text{eff}}$ is the number of effectively shallow sites. The same protocol is applied to the group of site types forming the effectively deep sites, where the rate equations have the structure

$$0 = f(S_i - N_i) + \Big(\sum_{j\neq i:T_j^{\max}<T} A_j N_j\Big)(S_i - 2N_i). \tag{10.17}$$

The corresponding energies are found by replacing the maxima with minimas:

$$\begin{aligned} E_{W_2,\text{eff}} &= \min_{\{i:T_i^{\max}>T\}} E_{W_i} \\ E_{a_2,\text{eff}} &= \min_{\{i:T_i^{\max}>T\}} E_{a_i} \\ S_{2,\text{eff}} &= \sum_{i:T_i^{\max}>T} S_i = S - S_{1,\text{eff}} \end{aligned} \tag{10.18}$$

The average numbers of particles on the effective site types are then given by

$$\begin{aligned} N_{1,\text{eff}} &= \Big(\sum_{i:T_i^{\max}<T} S_i\Big)\frac{N_{i^*}}{S_{i^*}} \\ N_{2,\text{eff}} &= \sum_{i:T_i^{\max}>T} N_i \\ &= (f + A_{1,\text{eff}} N_{1,\text{eff}}) \sum_{i:T_i^{\max}>T} \frac{S_i}{V_i + 2A_{1,\text{eff}} N_{1,\text{eff}}} \end{aligned} \tag{10.19}$$

where $i^* = \max_{\{i:T_i^{\max}<T\}} i$.

These equations can be evaluated using the approximation $V_i/a_i \ll (S - S_i)/S < 1$ for all types of sites and $V_i \approx f$ for the site types forming the effectively deep site type. We then arrive at the simple expressions

$$\begin{aligned} N_{1,\text{eff}} &= \frac{fS}{a_{1,\text{eff}}}\left(\frac{S}{S_{2,\text{eff}}} - 1\right) \\ N_{2,\text{eff}} &= \frac{S}{1 + 2(S/S_{2,\text{eff}} - 1)} \end{aligned} \tag{10.20}$$

for the number of particles on the effectively shallow and deep sites and can compute the efficiency of the system

$$\eta = \frac{2}{S/(S - S_{2,\text{eff}} + 1)}, \tag{10.21}$$

if in the effective system the condition for plateau formation $T_{\text{eq}} > T_{2,\text{eff}}^{\max}$ is satisfied. Otherwise, if $T_{\text{eq}} < T_{2,\text{eff}}^{\max}$, we have to revert to the original expression of the efficiency and calculate $\eta = 2A_{1,\text{eff}} N_{1,\text{eff}} N_{2,\text{eff}}/(fS)$.

10.3 Limits of validity

All results derived in this chapter are based on rate equations. Transferring them to real, spatially extended systems requires some caution as experienced in chapter 9. At least for temperatures $T_1^{\max} < T < T_2^{\max} (< T_n^{\max})$ with $n > 2$ the situation is simple. Since the absolute values of binding energies of the strong-binding sites do not matter, as particles cannot diffuse or desorb from them due to the low temperature, the combining of deep sites to the peak next to the actual temperature is straightforward and justified.

For the case of comprising different binding energies on which particles are mobile at the given system temperature T, the situation is not that clear. The larger the difference $T - T_i^{\max} (> 0)$, the quicker and easier particles desorb from these sites and the funneling mechanism to deep sites becomes less and less effective. Intuitively it is not clear, why combining sites providing mobility should work as well as combining sites trapping particles. Considering the situation $T_1^{\max} < T_2^{\max} < T (< T_n^{\max})$ with sufficiently well-separated homogeneous systems peaks at $T_1^{\max}$ and $T_2^{\max}$, we find the random walk length ℓ_{rw} on the different types of sites

$$\ell_{\mathrm{rw}} = \sqrt{\frac{a_i}{W_i}} = \exp\left(\frac{E_{W_i} - E_{a_i}}{2T}\right) = \exp\left(\frac{\text{const.}}{2T}\right) \tag{10.22}$$

to be independent of the disorder as discussed before (cf. section 9.1) and to decrease exponentially with growing temperature. To solve the problem on the rate equation level, we assumed above that $V_i/a_i = (W_i + f)/a_i \ll (S - S_i)/S < 1$ for all sites on which particles are mobile. For the random walk length on these sites this means

$$\ell_{\mathrm{rw}} \gg 1. \tag{10.23}$$

For the typical binding and hopping energies discussed here ($E_{W_i} - E_{a_i} = 147\mathrm{K}$), the temperature can reach quite high values ($\approx$ 70 K) before the random walk length drops below unity.[1] Hence, in the realm of physisorption, and for a sufficiently large number of deep sites, a particle on a shallow site always has a good chance to reach a deep site before desorption — in the well-mixed case or with 'longhop' dynamics. For surfaces with particular arrangements of binding sites, the validity of the rate equation solution will break down much earlier, as seen in the case of the binary distribution for the cluster distribution (figure 9.3).

Throughout the whole chapter, we implicitly assumed the sufficient separation of the binding energies. To quantify this vague formulation, we recall some findings of the binary system. The intermediate temperature regime of the binary system with the trapping mechanism dominating the surface's efficiency only exists, if the corresponding homogeneous peaks are separated well enough to exhibit an efficiency gap. The necessary amount of separation can be roughly estimated by demanding $T_1^{\max} < T_2^{\mathrm{low}}$. Then the plateau formula is valid for surface temperatures $T_1^{\max} < T < T_2^{\mathrm{low}}$. For binding energies that lie closer together, the efficiency has to be estimated using the full formula (9.14). Conveying these thoughts to the discrete distributions with n types of binding energies, we get a simple yet meaningful efficiency prediction for surface temperatures in regions $T_i^{\max} < T < T_{i+1}^{\mathrm{low}}$. We will revert to this discussion in section 11.7 when

[1] $T^{\max} = 70\mathrm{K}$ would correspond to a binding energy of $E_W \approx 3250\mathrm{K}$, which already belongs to the regime of chemisorption sites, as mentioned in section 9.3.

discussing this mapping together with an alternative one that will be derived in the next chapter in the context of continuous binding energy distributions.

10.4 Summary

Based on the findings of chapter 9 we were able to treat general discrete binding energy distributions based on the rate equations approach. The central finding of this chapter is the fact that even numerous different binding energies can be comprised into only two different types — effectively shallow and deep sites. The assignment of the original types of sites to the effective types 'shallow' and 'deep' is temperature-dependent, and requires a sufficiently large gap between the binding energies, namely $T_i^{\max} < T < T_{i+1}^{\text{low}}$. The energy assignment can be made quantitative by determining and grouping the types of sites with $T_i^{\max} < T$ and $T_i^{\max} > T$ and associate with them the largest and smallest binding and hopping energy present in their group, respectively. The numbers of sites of the effective types are determined by adding up all sites of either group. Then the results for the binary system derived in chapter 9 can be applied to the effective system. In the temperature regions around the efficiency windows of the corresponding homogeneous systems, more precisely for $T_i^{\text{low}} < T < T_i^{\max}$, the systems behavior is dominated by the behavior of the homogeneous system rather than the disorder.

The mapping is valid as long as even the particles on 'very shallow' sites have a chance of reaching a deep site within one step, which is expressed by demanding $\ell_{\text{rw}} \geq 1$.

For the ternary binding energy distribution, the rate equations were solved explicitly (section 10.1.1) and the results were confirmed by KMC simulations (section 10.1.2). In the KMC simulations we compared the efficiency as function of the temperature for the full ternary system and for the effective binary system corresponding to the temperature regime considered.

In the next chapter we will develop a mapping from continuous binding energy distributions to effective binary systems independent of the rate equations approach. In section 11.7, we will also apply this new mapping to the discrete distributions discussed here and verify, that both mappings predict the same efficiency for a given temperature within the realms of validity. Due to its simplicity, however, we expect the above presented rate equations based mapping to serve as a straightforward method to compare and fit the model to experiments.

Chapter 11

Continuous distributions of binding energies

So far, we discussed discrete distributions of binding energies. Nonetheless, also continuous distributions are of theoretical and applied interest [83, 63]. In this chapter we analyze the properties of systems with binding energies drawn from several kinds of continuous distributions that we believe to be relevant for applications and reveal the underlying mechanism of molecule formation on this type of surfaces. It turns out that such a kind of surface acts equal to an appropriately chosen binary one and thus we are able to define a mapping from the continuous to an effective binary system, thereby reproducing the efficiency as well as the coverage of the original system. We point out, that the mapping neither involves data obtained from simulations, nor does it depend on a special approach to the system (like the mapping based on rate equations in the last chapter 10). Instead we use KMC simulations again, to verify our analytical results.

11.1 The effective binary system

Encouraged by the possibility to map discrete binding energy distributions to effective binary systems, the central idea of our mapping for continuous binding

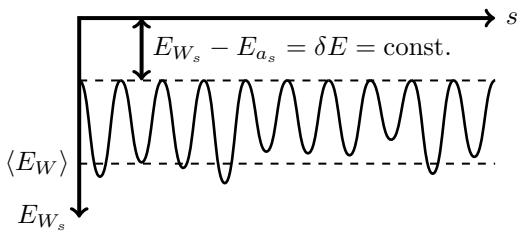

Figure 11.1: Cut through binding energy landscape with energies drawn from some continuous distribution with finite and known mean $\langle E_W \rangle$ and variance, as introduced in figure 8.2. Still detailed balance is included into the system by keeping $E_{W_s} - E_{a_s}$ constant for all sites s.

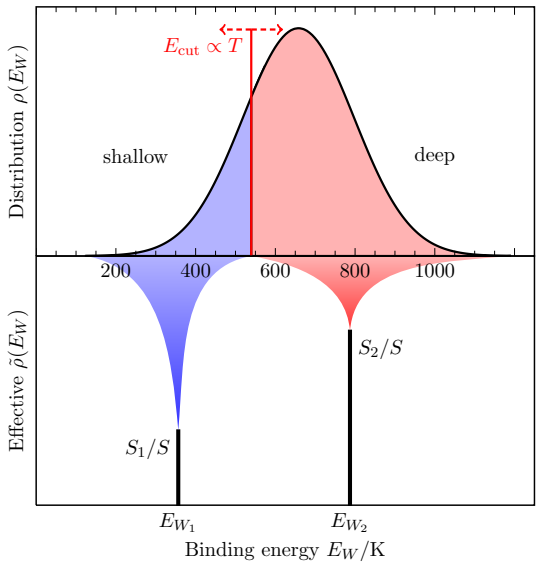

Figure 11.2: Basic idea of the mapping to the effective binary model.

energy distributions $\rho(E_W)$ is again that an energy landscape drawn from a continuous distribution of binding energies can be condensed to only two types of sites: The effectively "shallow" sites, which have low binding energy, and which provide particles with easy mobility and funnel them, namely into the effectively "deep" sites, which have high binding energy and which provide sufficient coverage. If this partition into shallow and deep sites is performed at the proper energy E_{cut}, and if the binding energies of the two effective types of sites are chosen appropriately, the original detailed binding energy of each individual site in a realization of the continuous case is irrelevant. Shallow sites in the effective model will reflect the overall mobility of particles on sites with energies smaller than E_{cut}. Deep sites in the effective model will capture the overall ability to bind particles strong enough to provide coverage on sites with energies larger than E_{cut}. Since both diffusion and desorption are thermally activated processes, it is obvious already at this stage that the threshold E_{cut} must increase with temperature.

Figure 11.2 depicts this central idea, the notation and further details will be described in the next section. Note that we always consider the effective binary system to be well-mixed—it is essential that deep sites are as easily accessible as possible from the shallow sites. This also ensures that the system is well described by rate equations, which we will also employ below. Moreover, we will focus on the case that there are still a reasonable number of both types of sites, or equivalently, that the continuous distribution is still sampled well on both sides of the threshold energy E_{cut}. The issue of rare events and sample-to-sample fluctuations will be returned to in 11.6. In the relevant case that these fluctuations are sufficiently small, our mapping is equivalent to a mapping from the entire continuous *distribution* of binding energies to a binary one. Unless specified otherwise, we will always refer to the latter mapping in the remainder.

11.2 Confirmation of mapping assumptions by simulations

The idea presented above has to be tested before we progress. To this end, we first introduce some additional notation and define the relevant quantities. We use subscripts ω for a realization of binding energies and s for a single site. Then $E_{\omega,s}$ is the binding energy of site s in realization ω (in this subsection, we will omit the subscript W for brevity). Further, $r_{\omega,s}$ denotes the steady-state (or time-averaged) fraction of all reaction events in realization ω that takes place on site s; we call $r_{\omega,s} \in [0,1]$ the *reactivity*. We denote by $u_{\omega,s}$ the steady-state fraction of (physical) time that site s in realization ω is occupied; $u_{\omega,s} \in [0,1]$ is called the *occupancy*.

We are interested in the relation between the binding energy of a certain site and its reactivity. On that account, we transform from the spatial distribution of reaction events to the distribution with respect to the local energy,

$$r_\omega(E) = \sum_s r_{\omega,s}\delta(E - E_{\omega,s}). \tag{11.1}$$

Obtained from a limited number of sites, $r_\omega(E)$ is obviously only a collection of S sample values from an imagined smoothed function. Gathering information from a set $\{\omega\}$ of realizations, we additionally have to weight this distribution for each single realization ω according to the efficiency η_ω of the latter, effectively accounting for the *number* of reaction events during a certain period of time: A site with given energy might be responsible for a much larger fraction in one realization simply because in distant parts of the surface the particular energy landscape results in fewer events. In this case the overall efficiency of this particular realization will be diminished, and rescaling by the efficiency removes this unwanted distortion. The result (which we still call "reactivity") reads

$$r_{\{\omega\}}(E) = \frac{\sum_\omega r_\omega(E) \cdot \eta_\omega}{\sum_\omega \eta_\omega}, \tag{11.2}$$

including proper normalization

$$\sum_E r_{\{\omega\}}(E) = \frac{\sum_\omega \eta_\omega \sum_s r_{\omega,s} \sum_E \delta(E - E_{\omega,s})}{\sum_\omega \eta_\omega} = \frac{\sum_\omega \eta_\omega \left(\sum_s r_{\omega,s}\right)}{\sum_\omega \eta_\omega} = 1. \tag{11.3}$$

The slightly clumsy notation is an artifact of the finite number of samples. In the limit considering the statistical ensemble of *all* possible realizations, the E sum becomes an integral, and functions of E become smooth.

For the occupancy of sites of a certain energy, we transform analogously to the above. Comprising several realizations does not need any weighting here, since the definition of the occupancy $u_{\omega,s}$ of a site does not relate to the total coverage in the realization. Normalization, however, implies we factor out the total number of particles in all realizations. Noting that the time-averaged total coverage in realization ω reads $N_\omega = \sum_s u_{\omega,s}$, we have

$$u_{\{\omega\}}(E) = \frac{\sum_\omega u_\omega(E)}{\sum_\omega N_\omega}, \tag{11.4}$$

again called "occupancy". Then

$$\sum_E u_{\{\omega\}}(E) = \frac{\sum_\omega \sum_s u_{\omega,s} \sum_E \delta(E - E_{\omega,s})}{\sum_\omega N_\omega} = \frac{\sum_\omega (\sum_s u_{\omega,s})}{\sum_\omega N_\omega} = 1. \qquad (11.5)$$

Figure 11.3 shows the occupancy and the reactivity as functions of the binding energy, comprised from KMC simulations for 10 realizations. We have chosen the paradigmatic example of the normal distribution here, with a relative width of $\tilde{\sigma} = 30\%$, and for several temperatures. The unprocessed functions $u_{\{\omega\}}(E)$ and $r_{\{\omega\}}(E)$ are *not* shown, as they exhibit strong fluctuations (we return to this issue in section 11.6). Instead, we present better approximations of the smooth ensemble averages, which we denote by $u(E)$ and $r(E)$. These approximations are obtained by a sliding average, in which the function's value at each sample energy E is replaced by the average of all points within a certain energy neighborhood. This is preferable to an average over a fixed number of neighboring points, since samples are not equally spaced on the energy scale. In our plots we use an energy interval of 4% of the total range of energies sampled. The original distribution of binding energies is drawn as a thin line for orientation. In order that the plots can be easily compared, we have rescaled this distribution to have a maximum value of unity. Likewise, we have rescaled $u(E)$ and $r(E)$ by a constant factor such that $u(E)$ attends a maximal value of unity as well.

Whenever sample-to-sample fluctuations become small, both occupancy and reactivity very clearly distinguish two types of sites according to their energy, with a fairly steep "step" between them. For lower energies there is little to no activity, and we identify these sites as effectively shallow. The sites with higher energies, however, provide nearly all the coverage and reaction events, and are effectively deep. Moreover on both sides of this border, the precise energy of the individual sites does no longer play any role.

The threshold energy E_{cut} separating both types of sites moves to higher energies as the temperature increases, as expected. For very high temperatures, only very few sites from the distribution tail still contribute coverage and reactions. On the other hand, we checked that the cut is largely independent of the shape and width of the distribution. Again, this is compatible with our earlier thoughts and will be substantiated in the next subsection. Figure 11.4 gives one example for the exponential and the uniform distribution, respectively, qualitatively similar to the results for the normal distribution. For the exponential distribution, high-energy tails decay more slowly than for the normal one, leading to a picture for $T = 30$ K which resembles those for lower temperatures in the normal-distribution case (with deep sites still over a large range of energies). The plot for the uniform distribution at $T = 10$ K hardly shows fluctuations in the (smoothed) occupancy and reactivity, compared with the normal distribution. This is due to the fact that there are no high-energy tails, so that energies are roughly equally (and "densely") spaced up to their maximum, and hence few outliers do not affect the smoothed plot at all.

Lastly, we find the agreement between the graphs for occupancy and reactivity remarkable in all instances. This shows that exactly the highly-occupied sites are those on which reactions take place, just as in the genuinely binary model. Together we thus have numerical proof of the arguments we have presented in section 11.1.

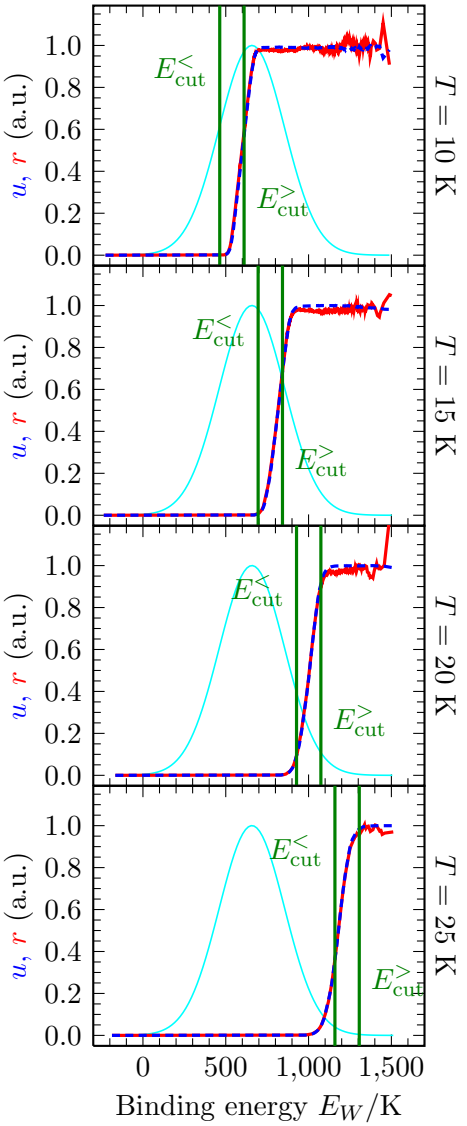

Figure 11.3: (Rescaled) occupancy $u(E_W)$ (blue, dashed) and reactivity $r(E_W)$ (red) versus binding energy E_W of the sites, for the normal distribution of relative width $\tilde{\sigma} = 30\%$ and at temperatures $T = 10, 15, \ldots, 25$ K (top to bottom). The rescaled PDF (thin cyan line) is shown for reference. The vertical green lines mark two specific choices for E_{cut} to be defined in 11.3.

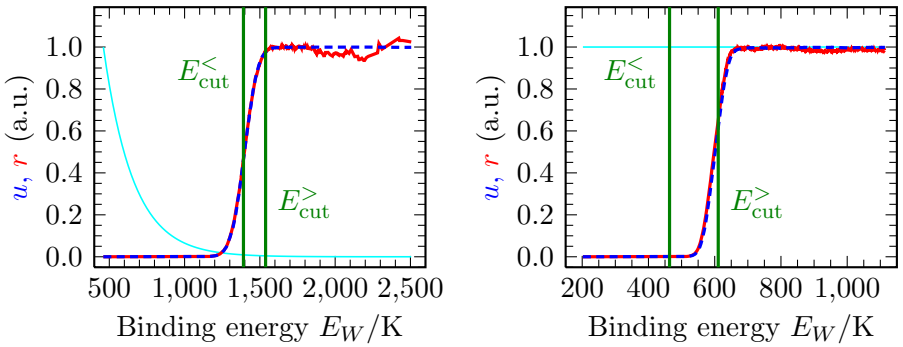

Figure 11.4: As in figure 11.3, $u(E_W)$ (blue, dashed) and $r(E_W)$ (red), for an exponential distribution with $\tilde{\sigma} = 30\%$ at $T = 30$ K (left), and for a uniform distribution with $\tilde{\sigma} = 40\%$ at $T = 10$ K (right). Rescaled PDF's (thin cyan line) shown for reference.

11.3 Heuristic derivation of the mapping

In principle, there are many strategies to find a mapping from the continuous to a binary model that reproduces the efficiency and coverage. It is even possible to find a mapping from the continuous to an effective homogeneous system, if all parameters of the system can be chosen arbitrarily. But this is not the aim of our work, since we are interested in understanding the underlying relevant physics. In our approach, we try to retain as many features of the continuous-distribution model as possible, altering only a minimal subset of parameters—thereby minimizing the arbitrariness of the mapping.

From a physics point of view it stands to reason to restrict changes only to the binding energy distribution itself. We will find a system, where only the binding energy of the sites is changed. Concretely, this implies that we keep f, T, S and ν fixed.

Note that we speak of a mapping of the binding energies E_W throughout, but the hopping barriers E_a are of similar importance. In the continuous case they are fixed by demanding constant $\delta E = E_W - E_a$ for all sites, which guarantees detailed balance, and implies a constant ratio W/a. We stick to this choice (particularly for the detailed-balance argument), using the same δE for the binary distribution.

Consequently, there are three quantities left that define the mapping: the discrete binding energies E_{W_1} and E_{W_2} of shallow and deep sites in the effective model, respectively, and the number of both types of sites. The latter can be conveniently parametrized by a *cutting energy* E_{cut} at which we split the continuous distribution of binding energies.

The discrete binary distribution has to capture the essential features of the original continuous one. The two most obvious properties of a distribution are the mean binding energy $\langle E_W \rangle$ and the standard deviation σ. To keep the arbitrariness as low as possible, we demand that the effective binary distribution has the same mean and standard deviation. [1] Once given the number of shallow

[1] Other choices have been tested to set E_{W_1} and E_{W_2} once S_1 and S_2 are known. But they all introduce additional arbitrariness without improving (but often detracting from) the quality of the mapped model predictions.

and deep sites, S_1 and S_2, the discrete binding energies are fixed and read

$$E_{W_1} = \langle E_W \rangle - \sigma\sqrt{S_2/S_1}, \qquad E_{W_2} = \langle E_W \rangle + \sigma\sqrt{S_1/S_2}. \tag{11.6}$$

Recall our earlier assumption that both S_1 and S_2 are not too small, and in particular that the binary model does not degenerate to a homogeneous model in the regime of our interest.

It only remains to choose E_{cut}, which governs how many sites are regarded as shallow and deep. As the simplest choice, we assume that this energy is independent of the shape and parameters of the distribution.

To find the appropiate E_{cut}, we now first consider the limiting regime of high temperature. There are many shallow and few deep sites, regardless of the precise form of E_{cut}. The limiting factor for the efficiency is lack of coverage on the deep sites, while mobility on shallow sites (to quickly funnel atoms to the deep ones) is a given. Hence, we have to split the binding energy distribution at an E_{cut} such that at this and at higher energies, sites are sufficiently occupied. This energy is set by $f = W|_{E_W = E_{\mathrm{cut}}}$, such that without any reactions, we would have half-filling on average. This means

$$E_{\mathrm{cut}} = E_{\mathrm{cut}}^{<} := T \ln(\nu/f) \quad (\text{high } T). \tag{11.7}$$

Mobility on the shallow sites is then guaranteed by $a|_{E_W \leq E_{\mathrm{cut}}} \geq a|_{E_W = E_{\mathrm{cut}}} \gg W|_{E_W = E_{\mathrm{cut}}} = f$.

For low temperatures, the overall surface coverage is high and there are lots of deep but only a few shallow sites. In this regime, the efficiency is limited by a lack of mobility instead of a lack of coverage. Particles have to hop at least as frequently as new ones arrive, or else LH rejection will curtail the efficiency. Therefore, the maximal energy of "working" shallow sites is set by $f = a|_{E_W = E_{\mathrm{cut}}}$, and sites at lower energies have $a > f$. Re-writing the condition using $E_a = E_W - \delta E$ we obtain

$$E_{\mathrm{cut}} = E_{\mathrm{cut}}^{>} := T \ln(\nu/f) + \delta E \quad (\text{low } T). \tag{11.8}$$

On the deep sites, we then have $f \geq a|_{E_W \geq E_{\mathrm{cut}}} \gg W$, so high coverage there is guaranteed.

In the figures 11.3 and 11.4 for the energy-resolved occupancy and reactivity, the two choices for E_{cut} are shown as vertical lines. Also the figures themselves suggest a reasonable choice for E_{cut}, at e.g. the energy at which the occupancy or reactivity reach half of their maximal value. Comparing this choice with $E_{\mathrm{cut}}^{<}$ and $E_{\mathrm{cut}}^{>}$, we find E_{cut} to always between the former two. And indeed we find in the simulations our heuristic derivations confirmed: the suggested cutting energy moves closer to the upper energy $E_{\mathrm{cut}}^{>}$ for low temperatures, whereas it comes closer to the lower energy $E_{\mathrm{cut}}^{<}$ for higher temperatures.

The shift of δE between the two choices reflects the fact that in the above arguments, for high temperatures the distribution of *binding energies* is cut in two, while at low temperatures the distribution of *diffusion barriers* is cut. These results are indeed independent of the shape, mean, and width of the distribution, as suggested above.

The limiting temperature regimes correspond to finite temperatures (not to $T \to 0$ and $T \to \infty$, that is), hence the transition between them involves additional temperature scales (describing location and width). These quantities

evidently have to depend on the shape and width of the distribution, which we will confirm by simulation results (see below). We have not found a convincing theoretical argument to determine these scales. In practice, it is still straightforward to determine the appropriate choice for E_{cut}. Sites with energies in the range $[E_{\mathrm{cut}}^{<}, E_{\mathrm{cut}}^{>}]$ provide coverage *and* mobility, and could be labeled *either* deep or shallow, depending on this choice. The proper choice of E_{cut} in the limits of low and high temperature regards these sites to provide the scarce property which limits the efficiency, respectively. The "opposite" choice misinterprets their role and leads to substantially lower efficiency.[2] Summing up, in both limits, one chooses E_{cut} such that it leads to the *highest possible efficiency in the effective model*. It is then plausible to stick with this prescription for intermediate temperatures as well.

In principle, cutting the distribution at E_{cut} provides real values for the numbers S_i of sites of a given type. To stay true to the idea that we replace the whole energy landscape by an effective one, we round to the nearest integer values for S_i, when the effective system has physically sensible parameters throughout. In the case where the system is sufficiently large and still has a substantial number of both shallow as well as deep sites, the difference to the nearest integer values is negligible anyway.

11.4 Comparison to KMC simulations

We have introduced the mapping to an effective binary model, and we have reviewed earlier (cf. chapter 9) how this model is described and solved using rate equations. We will now compare its predictions with the outcome of KMC simulations. For each temperature and distribution shape and width, we simulated 10 realizations as described in section 9.3. Figure 11.5 shows that overall, agreement between the KMC results and the prediction of the effective model is very good, for both the coverage and the efficiency. Most importantly, the temperature range of efficient reaction is reproduced with very good accuracy in most circumstances—this is the truly valuable information, compared with minor deviations in the efficiency itself. There is some discrepancy between KMC and effective model results in the high-temperature tail for the normal and the exponential distribution. The rate equation solution of the effective model describes hops between *any* two sites of the lattice, such that spatial correlations are switched off entirely. If we include such "long hops" in the KMC simulations, the efficiency also increases (as checked in several test runs, and as previously found and explained for the binary system [89]), and it then agrees even better with the effective model results.

The system now shows a broad temperature window of high efficiency, different from the homogeneous system, but also from the binary case, as far as the slow decay to higher temperatures is concerned (cf. figures 9.2 and 9.7). Likewise, we observe a smooth monotonic transition from full coverage to an empty system, in stark contrast to the binary case—this illustrates once more that the effective

[2] For narrow exponential and uniform distributions ($\tilde{\sigma} = 10\%$), this statement is not strictly true: There is a very small range of low temperatures at which the "high-T" model has *marginally higher* efficiency, starting where it is still degenerate (no shallow sites) and ending just after it features both effectively shallow *and* deep sites. This is an artifact of the simple mapping prescription, and in any case, such narrow distributions are not the focus of this work.

binary model we map to changes its structure with temperature. It is also evident that sample-to-sample fluctuations are a subordinate effect throughout, even on the critical flanks of the efficiency and for the long-tailed exponential distribution. We will return to this issue in section 11.6.

Of special interest is the range of validity of the mapping idea. As emphasized before, it relies on the presence of both types of sites, shallow and deep, in the effective model. This is no longer satisfied at very low temperatures, when all sites are effectively deep ($S_1 = 0$), and at very high temperatures, when all sites are effectively shallow ($S_2 = 0$). Obviously, these limits are reached at less extreme temperatures for narrower distributions (upper rows), and in the absence of distribution tails, as exemplified by the uniform and (to lower energies) the exponential distribution. The effective model degenerates to a homogeneous system then, with the binding energy given by the mean of the distribution. For the figure, we correspondingly replaced the numerical solution of the effective binary model by the analytical results for the homogeneous case.

For very low temperatures, the examples studied here show essentially full coverage and zero efficiency, which is trivially reproduced by the homogeneous rate equation results. The support of the exponential and the uniform distribution is bounded to low energies. Therefore, the transition to the $S_1 = 0$ regime is not smooth, which manifests itself in the discontinuous derivative of coverage and efficiency. For high temperatures, the situation is more subtle. The normal and the exponential distribution, which both have tails to high energies, are still accurately described at very high temperatures: For most of the panels shown, $S_2 = 0$ is reached eventually, but only after the KMC efficiency has vanished completely. Up to this temperature, there are still *some* deep sites in the effective model owed to the distribution tail (not visible in the plots due to limited resolution), and they are sufficient to reproduce KMC results. At still higher temperatures, the effective homogeneous system trivially reproduces zero coverage and efficiency. For the uniform distribution, however, KMC results show a fast (but by no means abrupt) decay of the efficiency with increasing temperature. Due to the lack of high-energy tails (which could still provide a few deep sites), the effective model now degenerates ($S_2 = 0$) at a temperature low enough that KMC results still exhibit some efficiency. For a very narrow distribution ($\tilde{\sigma} = 10\%$) this happens so early ($T \approx 18$ K) that the resulting effective model (homogeneous with binding energy $\langle E_W \rangle$) still shows the high-temperature flank seen in figure 8.3. For all wider distributions the switch to the degenerate effective model occurs at temperatures where the homogeneous system has no efficiency left, while the KMC results still have residual efficiency, most likely due to the mere fact that there *is* a distribution of different binding energies (in part exceeding $\langle E_W \rangle$) and possibly some spatial correlations.

11.5 Tail shape and analytical expressions

For a homogeneous system, the tail shape of the efficiency $\eta(T)$ (fairly symmetric to low and high temperatures) is well understood (cf. chapter 8.2): The efficiency decays exponentially with the temperature in both cases, since all rates are

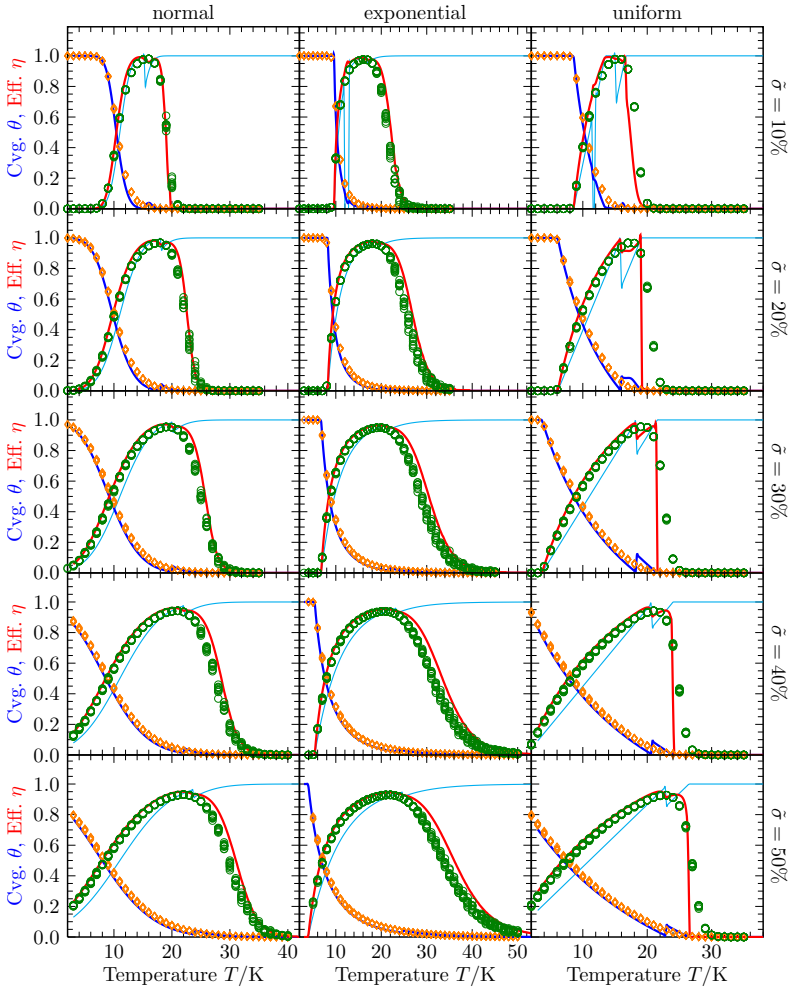

Figure 11.5: Coverage θ (orange diamonds, blue lines) and efficiency η (green circles, red lines) versus temperature T, of the continuous-distribution system from KMC simulations (marks, one per realization), and as obtained for the effective binary model via rate equations (lines). Also shown is the fraction S_1/S of shallow sites in the effective model (thin cyan line). Columns (left to right) for normal, exponential, and uniform distribution, rows for several relative widths $\tilde{\sigma} = \sigma/\langle E_W \rangle$ as indicated. The spikes seen at an intermediate temperature, most notably for S_1/S, are a result of the switch of E_{cut} between $E_{\mathrm{cut}}^{>}$ and $E_{\mathrm{cut}}^{<}$.

thermally activated. From the rate equation efficiency (8.11) one finds

$$\begin{aligned} \eta &\simeq 2\frac{a}{f} = 2\frac{\nu}{f}\,\mathrm{e}^{-E_a/T} && \text{(low-}T\text{ tail)}, \\ \eta &\simeq 2\frac{fa}{W^2} = 2\frac{f}{\nu}\,\mathrm{e}^{(2E_W-E_a)/T} && \text{(high-}T\text{ tail)}, \end{aligned} \tag{11.9}$$

which mirrors the temperature bounds (8.12) and (8.13). The tail *shapes* for the binary system are the same as for the homogeneous system, since for each tail only reaction on one type of site is important.

For continuously distributed binding energies, however, the situation is different. There are many similar binding energies acting almost but not exactly the same (at a certain temperature). This is reflected by the slower decay of the efficiency. We now use the mapping to the effective binary model to derive an analytical expression for the (low-temperature) tail shape.

As alluded to in chapter 8.2, the binary system exhibits a plateau of the efficiency $\eta(T)$ between the two peaks of the corresponding homogeneous systems in certain conditions. More precisely, one needs enough deep binding sites—depending on the temperature, flux and the difference in the binding energies of the two types of sites. Following [89], we let T^{eq} denote the temperature below which the random walk length (on shallow sites), $\ell_{\mathrm{rw}} = \sqrt{a_1/W_1}$, exceeds the average hopping length before encountering a trap [66, 32], $\ell_{\mathrm{trap}} \simeq \sqrt{S/(\pi S_2)\cdot \ln S}$: At lower temperatures, particles typically end in deep sites. If $T^{\mathrm{eq}} > T_2^{\max}$ we find a plateau, with an efficiency of [89]

$$\eta_{\mathrm{p}} \approx \frac{2}{1+S/S_1}. \tag{11.10}$$

Now in the effective binary model, the energies and numbers of both types of sites are functions of E_{cut} and thus depend on the temperature T. For the low temperature tail of all shown distributions, we have sufficiently many deep sites S_2 in the effective model, such that the condition $T^{\mathrm{eq}} > T_2^{\max}$ is satisfied—the effective model (for the given temperature) features a plateau. One also finds that $T_1^{\max} < T < T_2^{\max}$, such that we evaluate the model *on* this plateau, and the formula (11.10) applies. The fraction of shallow sites S_1/S in the effective model is given by the cumulative distribution function $\Phi(E_{\mathrm{cut}}) := \int_{-\infty}^{E_{\mathrm{cut}}} \rho(E_W)\,\mathrm{d}E_W$. Lastly, since we are in the low-temperature tail, we have (cf. 11.3) $E_{\mathrm{cut}} = E_{\mathrm{cut}}^{>} = T\ln(\nu/f) + \delta E$, leading to

$$\eta \approx \frac{2}{1+\Phi(T\ln(\nu/f)+\Delta E)^{-1}} \quad \text{(low } T\text{)}. \tag{11.11}$$

This expression shows a much weaker dependence on temperature compared with the homogeneous and (genuinely) binary cases with their exponential decay. It also explains that the broader tails of the efficiency do not necessarily originate from tails of the underlying distribution $\rho(E_W)$ (provided there still *are* both deep and shallow sites). Rather, the decisive factor is that the mapping introduces a T-dependent split into shallow and deep sites via the cutting energy E_{cut}—without thermally activated rates playing any role. Moreover, this implies a lower temperature bound of efficient reaction (where $\eta = 1/2$) given by

$$\Phi(T^{\mathrm{low}}\ln(\nu/f)+\delta E) = \frac{1}{3}. \tag{11.12}$$

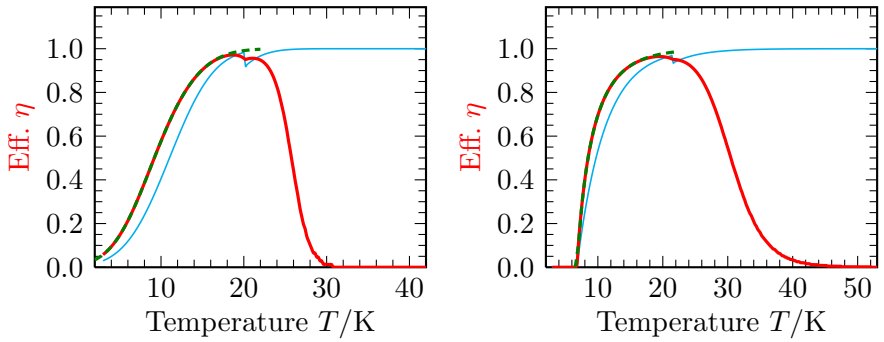

Figure 11.6: Efficiency η versus temperature T in the effective binary model, evaluated using the numerical solution of rate equations (red, as in figure 11.5) and as given by the analytical expression (11.11) (green, dashed), for a normal distribution with $\tilde{\sigma} = 30\%$ (left), and for an exponential distribution with $\tilde{\sigma} = 30\%$ (right). For reference, the fraction S_1/S of shallow sites in the effective model is shown again (thin cyan line).

Figure 11.6 shows that indeed the low-temperature expression (11.11) is extremely accurate up to intermediate temperatures around the efficiency peak temperature. This corresponds to the fact that the plateau in the binary model breaks down only at rather low fraction S_2/S (depending on $E_{W_2} - E_{W_1}$). We have checked that these statements hold true for all parameters used in figure 11.5.

For the high-temperature tail, the situation is more subtle. Here, the effective binary model only has few deep sites, and they are far from the mean energy $\langle E_W \rangle$ (cf. equation (11.6)). Even a fixed such model has no efficiency plateau then, but a T-dependent efficiency drop between the "homogeneous peaks" [89, Figure 5]. We do not have an illuminating analytical expression for this dependence, wherefore the upper temperature bound T^{up} remains inaccessible as well.

11.6 Realization dependence

We first comment on the effect of the quenched nature of disorder at the *microscopic* level. In any particular realization of the system, sites with similar binding energy may live in a very different local neighborhood. Therefore, they can differ strongly in the occupancy u and the reactivity r. This is very prominent in the raw simulation data, and the variability was intentionally reduced in figures 11.3 and 11.4 by using a sliding average. The site-to-site variability only vanishes in passing to the ensemble of all realizations (or infinite system size $S \to \infty$), whereas purely stochastic fluctuations decrease with increasing simulation time. We have confirmed this distinction by comparison with KMC simulations in which spatial correlations are suppressed ("long hops" between all sites are included, cf. section 11.4). This indeed removes the major part of the variability in occupancy and reactivity.

Interestingly, site-to-site variations are much more pronounced for the reactivity than for the occupancy. The reason for this is as follows: Consider the system dynamics over a certain period of time, and we are only concerned with effectively deep sites, where essentially all coverage and reaction events are concentrated. The number of such events on a given site is (to a good approximation) Poisson-distributed, with a rate parameter depending on the

local surroundings. Together with statistical fluctuations, this gives rise to the variability seen in the reactivity r. For the occupancy u, individual occupation times of a site are added up and compared with the total time passed. Since only a reaction event empties the site (hopping and desorption from deep sites is negligible), there are as many individual occupation times as there are reaction events on this site. This strongly anticorrelates the number of such events with the length of individual occupation times—if particles arrive more frequently, single occupation times are shorter. Therefore the number of reaction events (and hence, the reactivity) can strongly differ between two sites of similar energy, yet the fraction of time they are occupied (the occupancy) will differ far less. Note that the reduced variability in the occupancy versus the reactivity immediately translates to that of the total coverage versus the efficiency between different realizations.

We now turn to this dependence of *global* quantities on the realization. The overall system size in this article is large enough not to expect a noticeable dependence of the coverage and the efficiency on the realization. This is confirmed in figure 11.5 for the lower-temperature regime of both the coverage and the efficiency. For the high-temperature decay of the efficiency, however, such a dependence is clearly seen in the vertical spread of symbols referring to different realizations, both in the case of the normal and the exponential distribution. Somewhat counterintuitively, the variability between realizations *decreases* with increasing disorder strength (width of the distribution).

The mapping to an effective model explains if and why we see significant sample-to-sample variations of the efficiency. As explained at the end of section 11.5, for high temperatures the effective binary model has few deep sites, far from the mean binding energy. We know (from both simulations and numerical solutions of the rate equations), that in this regime the efficiency of the binary system is very sensitive to the exact number of deep sites [89]. This is perfectly intuitive, since there are so few of them, yet they are very important for the reaction. Applying the mapping to *different realizations* of the finite continuous-distribution system, the number of *effectively* deep sites also varies, and because there are few in any case, the variations relatively matter a lot. The sensitivity of the effective binary model to their number (at fixed T) thus explains the realization dependence of the KMC efficiency of the continuous system (figure 11.5), and why it only shows on the high-temperature flank. Moreover, it is more pronounced for narrower distributions of the binding energy, since steeper flanks of the PDF lead to larger relative variations in the small number of effectively deep sites. The coverage is already very small in this regime, such that its realization dependence is not visible in figure 11.5.

It is an interesting feature that, though part of a nominally large system, the smallness of one crucial component (the number of deep sites) is enough to imply a strong realization dependence of a key quantity such as the efficiency. This constitutes an *effective small-system regime*, in the sense that the realization dependence will still vanish as usual upon increasing the total system size S. In this context, the mapping to an effective model concisely explains that depending on the temperature, we are in different regimes as to the effect of disorder. The asymmetry between shallow and deep sites (i.e., why is there no strong sensitivity when there are only few of the former?) is easily resolved. At temperatures so low that there are very few effectively shallow sites only, $S_1/S \ll 1$, application of the plateau formula (11.10) (as justified in section 11.5) yields $\eta_\mathrm{p} \approx 2S_1/S \ll 1$.

Therefore, whatever sample-to-sample variability there is in the efficiency cannot be seen in figure 11.5. On the other hand, the sensitivity of the coverage to the realization is much weaker anyway, as shown above.

11.7 Connection to discrete-distribution mapping

During the analysis of disordered surfaces we derived two different mapping to effective systems with binary disorder. In chapter 10, a general discrete distribution with n types of binding energies was mapped onto an effective system using rate equations. In this chapter here, we mapped continuous distributions to effective binary ones using only the distribution and a well-defined cutting energy. The mapping from the continuous distributions does not explicitly depend on the continuous character of the distribution. Rather, we implicitly showed that it is also applicable to discrete distributions by confirming its validity by comparisons to KMC simulations (for finite system sizes). In general on application to a discrete distribution, the mappings will result in two effective binary systems with different sets of shallow and deep binding energies. To assure that nevertheless both mappings result in the same efficiency prediction when applied to a discrete distribution with n types, we now take a detailed look at both mappings.

The essential feature of the binary system is the energy- and temperature-independence of the efficiency for intermediate temperatures — if the system possesses enough deep sites. The plateau efficiency is solely determined by the relative amount of sites. Under the premise of sufficiently many deep sites in the effective systems, we have to assure that — within the validity limits of both mappings — the effective models provide the same number of shallow and deep sites. We can perceive the premise on the number of deep sites as a constraint on the system temperature T.

First we calculate the effective binary distribution for a discrete distribution with n types of binding energies E_{W_i}. The probability density for the discrete distribution can be written as

$$P(E)dE = \sum_{i=1}^{n} \frac{S_{E_{W_i}}}{S} \delta_{E,E_{W_i}} \tag{11.13}$$

with the Kronecker-Delta $\delta_{E,E_{W_i}}$. The number of shallow and deep sites for given a temperature is determined by the integrals

$$\begin{aligned} S_1 &= S \cdot \int_{-\infty}^{E_{\mathrm{cut}}} P(E)\, dE = \sum_{E_{W_i} < E_{\mathrm{cut}}} S_{E_{W_i}} \\ S_2 &= S \cdot \int_{E_{\mathrm{cut}}}^{\infty} P(E)\, dE = \sum_{E_{W_i} > E_{\mathrm{cut}}} S_{E_{W_i}} = S - S_1. \end{aligned} \tag{11.14}$$

And thus, S_1 and S_2 together with their assigned energies (11.6) are piecewise constant, whenever $E_{W_{i^*}} < E_{\mathrm{cut}} < E_{W_{i^*+1}}$, where i^* and $i^* + 1$ indicate the next-lying energies to E_{cut}.

We remember that E_{cut} refers to a cutting energy of the binding energy distribution for high temperatures and a cutting energy of the hopping energy distribution for low temperatures. We showed in section 11.5 that, as long as

the low temperature expression is adequate, the plateau formula is applicable to the effective binary system.

As long as the different binding energies of the original discrete distribution are well-separated such that $E_{W_i} < E_{a_{i+1}}$ (or $T_i^{\max} < T_{i+1}^{\text{low}}$ in the temperature formulation), the shift in the cutting energy for low and high temperatures has no effect on the number of effectively shallow and deep sites. Simultaneously, this ordering in the characteristic temperatures of the corresponding homogenous systems (to the occurring energies in the discrete distribution) allows the utilization of the plateau formula in the effective binary system, as discussed in section 10.3 in the context of the discrete-distribution mapping. Then the plateau formula gives a correct efficiency prediction for all temperatures $T_i^{\max} < T < T_{i+1}^{\text{low}}$ (assuming the effective system develops a plateau).

Concluding, we can say that both mappings result in the same efficiency prediction (but from different effective binary systems), if the binding energies in the original discrete distribution fulfill the condition $E_{W_i} < E_{a_{i+1}}$. Thereby we always restrict to the case of a fulfilled plateau condition in the effective binary systems. We illustrate the different mappings using the example of a ternary system in figure 11.7.

If the ordering condition in the binding and hopping energies is locally *not* fulfilled, the mappings can be applied nonetheless. Then we also have to take care of the individual mapping properties. Consider the case of $E_{W_i} > E_{a_{i+1}}$ for some binding energy of the discrete distribution with a system temperature so low that for the continuous-distribution mapping the choice $E_{\text{cut}}^{>}$ has to be employed. Then the numbers of shallow and deep sites in both effective systems differ, but the effective system of the continuous distribution still develops a plateau and the plateau formula is applicable here, while for the effective system of the discrete-distribution mapping this is not the case (as discussed in section 10.3). For the two other cases, namely $E_{W_i} > E_{a_{i+1}}$ without plateau formation in the effective system, and $E_{W_i} < E_{a_{i+1}}$ without plateau formation, the relative amounts of shallow and deep sites in the effective systems become the same again, but the full efficiency expression (9.14) has to be evaluated.

11.8 Conclusions

We studied the effect of continuous binding energy distributions on the efficiency of a disordered surface. The surface sites can play two roles in this scenario, as verified in simulations: if the binding energy is low enough, sites provide mobility of particles to traverse the surface. If their binding energy is strong enough, they instead provide coverage by trapping particles for a long time. As a result, we can map the continuous-distribution model to an effective binary model of these shallow and deep sites, which is well understood and easily solved (cf. chapter 9). The precise form of the mapping has been derived heuristically and does not depend on any fitting parameters or approaches like the rate equations. As shown in section 11.4, the model yields results for the coverage and the reaction efficiency which are in good agreement with simulations. Compared with the case of discrete distributions studied before, the model shows a markedly different behavior, with the temperature range of efficient reaction broadened and the tails decaying much slower. The mapping explains this slower decay for low temperatures, as well as the sample-to-sample fluctuations found for the high-

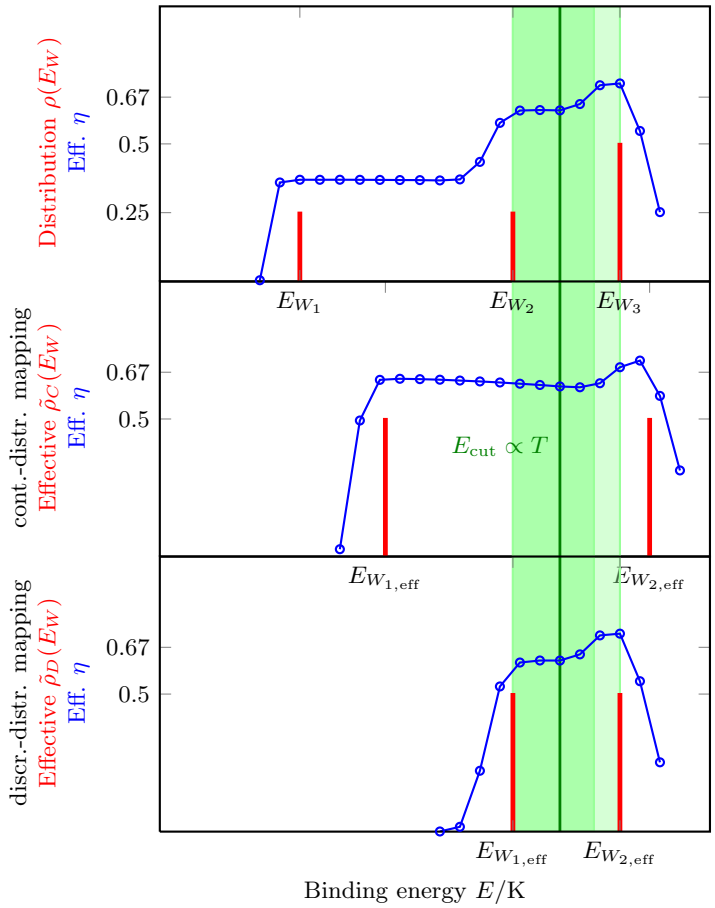

Figure 11.7: Illustration of the different mappings for a ternary system with 25% shallow and intermediate sites and 50% deep sites with energies $E_{W_1} = 658K$, $E_{W_3} = 1658K$, and $E_{W_3} = 2158K$, respectively. Blue circles: Efficiency from KMC simulations for each of the depicted binding energy distribution. The upper picture is showing the original distribution, the effective binary system of the continuous-distribution mapping is shown in the middle, and the low picture displays the results of discrete-distribution mapping. The system temperature T, with $T_2^{\max} < T < T_3^{\max}$, is indicated by the green vertical line. The theoretically predicted efficiency value of $\eta_{\text{p}} = 2/3$ is not perfectly reached by the KMC simulations for nearest-neighbor hopping, as explained in section 9.3, but all three systems show the same efficiency at the system temperature. Moreover, in the whole temperature regime $T_2^{\max} < T < T_3^{\text{low}}$, indicated by the light green background color, the efficiency in the three systems is (approximately) the same.

temperature decay of the reaction efficiency.

Additionally, we showed that the application of the continuous-distribution mapping to a discrete distribution results in the same efficiency predictions as the ones from the earlier derived rate equation based mapping (chapter 10). It has become clear that the mechanism of sites either providing mobility or acting as traps is the fundamental mechanism determining the behavior of all analyzed systems with quenched disorder on the surface.

The particular model studied here is paradigmatic for applications in astrophysics and in heterogeneous surface catalysis. Moreover, the existence of a simple mapping from a highly complex to a simple effective model is of great theoretical value.

Here we end our investigations on single-species reactions on surfaces with rate disorder. We think this issue is adequately covered by the presented work.

Chapter 12

Different particle species on a surface

In this last chapter we present our modest efforts in understanding the interplay between different (competing) reaction channels in multiple-species systems systematically. When it comes to the more realistic situation of reactions between several particle species, the systems to be analyzed become significantly more complex. And starting a thorough analysis of multiple species reactions would open up a completely new field. The so-far studied fundamental and important single-species reactions give us the opportunity to understand the influence of disorder on the reaction process. However, in the ISM also more complex molecules are built (both in the gas phase and on the dust grain surfaces) and understanding the formation of the latter is crucial — not least to have a correct input for the complex chemical network models that try to emulate (parts of) the whole chemistry of a molecular cloud.

The existence of several pathways for the formation of larger molecules makes the situation even more complicated. Water (H_2O), which is highly abundant in the ISM, is a prominent example. It can be produced both in the gas phase and on surfaces. Tielens and Hagen [82] first proposed the water formation on dust grain surfaces and by now it is known, that even for this comparably small molecule different pathways exist to form water on the surfaces [49, 23, 72] and experimental evidence for water formation on surfaces under interstellar conditions has been given [28]. At low temperatures, the water even stays on the surfaces and forms an icy mantles that contain most of abundant water [18], bringing us back to the surfaces with (quasi) quenched disorder. Some other very important reaction networks worth studying are the formation of CO_2, CH_4 (methan), and CH_4O (methanol). For all of them strong evidence exists, that a considerable amount of molecules is produced on interstellar surfaces [36, 60].

In order to get a tractable description of systems with one particle species, the introduction of detailed balance in the hopping rates on the surface, implemented in our case by a constant value $E_W - E_a$ (for all sites), was a crucial ingredient to get the correct equilibrium state for vanishing incoming particle flux. To preserve such a condition also for more than one species, we can demand detailed balance to hold for each of the species. But since each species has its own individual desorption and hopping energies (for one surface material), we can in

general not arrange for a global difference $E_{W_\alpha} - E_{a_\alpha} = \text{const.}$ for all particle types α. However, if $\text{const}_\alpha = \text{const.}$ for all types α, then the corresponding single-species systems' efficiency peaks of all particle types are of same width. As a treatment by kinetic Monte Carlo simulations would involve the development of a completely new simulation code, in this chapter we make use of rate equations only. Taking into account that for all former investigations simulations and rate equations coincided very well, as long as the system size and the occupation numbers are large enough, the missing simulations should be no drawback.

We start with the rate equation analysis of a generic two-species system in section 12.1. In section 12.1.1 we discuss how efficiency can be defined for arbitrary multiple- species systems. Afterwards, we present our analytical and numerical findings in section 12.2, before ending this discussion by an outlook in section 12.3.

12.1 Rate equations

Here, we concentrate on a generic system consisting of two particle species a and b with binding energies $E_{W_a} < E_{W_b}$. We refer to them as 'weakly-bound' and 'strongly-bound' species, respectively. We assume that in the system three kinds of dimers can be formed: $a + a \to a_2$, $b + b \to b_2$ and $a + b \to ab$, all with a probability depending only on the chance of the involved reactants to meet. Also, the products of the reactions are assumed to leave the surface immediately, so we do not account for second and higher order reaction of types like $a_2 + b \to a_2 b$.

A real system showing these three kinds of reaction channels is the formation of H_2, HD, and D_2 from atomic hydrogen and deuterium. Lipshtat et al. study in [62] the formation of the three molecules on small grains with physisorption sites using the master equation approach. They find a low formation rate of D_2 and a decrease in the production of all three molecule types with decreasing grain size. The emphasis of the work of Caseaux et al. [20] also lies on the grain size dependence, but they study a model that includes physi- and chemisorbed sites by means of rate equations. In their model they find an enhanced production rate of HD and D_2 because the H-atoms mainly populate the chemisorbed sites, while the D-atoms mainly populate the physisorption sites. In our language this corresponds to deuterium being the weakly-bound and hydrogen being the strongly-bound species.

Sticking to the hitherto employed philosophy of improving the qualitative understanding of elementary processes, we now analyze the rate equations corresponding to the introduced generic system. They can be written down straightforwardly

$$\begin{aligned} \frac{\mathrm{d}N_a}{\mathrm{d}t} &= f_a(S - N_a - N_b) - W_a N_a - A_a N_a N_b - A_b N_a N_b - 2A_a N_a^2, \\ \frac{\mathrm{d}N_b}{\mathrm{d}t} &= f_b(S - N_a - N_b) - W_b N_b - A_b N_a N_b - A_a N_a N_b - 2A_b N_b^2, \end{aligned} \tag{12.1}$$

where f_a, f_b are the incoming particle fluxes, A_a, A_b denote the hopping rates and W_a, W_b the desorption rates for each species, respectively. Again, we include LH-rejection and assume the system to be large enough such that the approximate description by rate equations as well as the approximation of the sweeping rate $A_\alpha = a_\alpha / S$ is valid. The number of particles of each species can

vary from 0 to S, the number of surface sites, and the meeting of two particles on the same site by hopping leads to instantaneous dimer formation.

For simplicity, we assumed the probabilities for dimer formation not to depend on the kind of dimer, but merely on the chance of meeting a particle of either type. To keep it even more simple, we adopt the choice $E_{W_a} - E_{a_a} = E_{W_b} - E_{a_b} = \text{const}$. For any realistic system, this strongly restricts the choice of particles. The rate equations for steady state can — in principle — be solved analytically but do in general not provide instructive solutions that improve the qualitative understanding of the system. Therefore, we rather opt for solving the full rate equations numerically and search for effective analytical expressions in certain temperature or parameter regimes. Next, we discuss the analytical results we found for this system. For not mentioned temperature regimes, we were not able to find a simple but meaningful solution, yet.

We start by considering the case of low temperatures $T \ll T_a^{\max} < T_b^{\max}$, where $T_a^{\max}$, $T_b^{\max}$ correspond to the temperatures of maximal efficiency in the corresponding homogeneous systems. At low temperature $W_b \ll W_a$, $A_b \ll A_a$, $W_a \ll A_a$ and $W_a, A_a \ll 1$ hold, so we neglect all terms $\propto W_b, A_b$, and keep in the solution of (12.1) only the flux terms and terms $\propto A_a, W_a$. Then the only positive and real solution we get from (12.1) is

$$N_a = 0, \quad N_b = S, \tag{12.2}$$

which is not surprising at all. Since the particle number of each species can vary from 0 to S and a-particles are more likely to leave the surface (either via desorption or recombination) than b-particles, the sites will all eventually become occupied by b-particles.

For very high temperatures, $(T_a^{\text{up}} <) T_b^{\text{up}} < T$, desorption dominates the behavior of the particles, the surface is nearly empty $N_a \approx N_b \approx 0$, and the efficiency drops to zero, too. So we turn our attention to the intermediate temperature regime $T_a^{\max} < T < T_b^{\max}$.

In the case of two species with well-separated homogenous system peaks and equal incoming particle fluxes, we can find a simple solution for the temperature regime $T_a^{\text{up}} < T < (<) T_b^{\text{low}}$. To be more specific in the case $W_b \ll f_b \ll 1$, $A_a \gg A_b$, $W_a \gg W_b$, and $f_a = f_b \equiv f$, the rate equations can be substantially simplified. Since the temperature is high with respect to the weakly bound species, the average number of type-a particles on the surface will be low and we can neglect all terms $\propto N_a^2$. Additionally, the temperature is so low that the strongly bound species does not move substantially, so we also neglect the terms $\propto A_b$. With $W_i + f_i = V_i$, we arrive at the following set of equations

$$\begin{aligned} 0 &= f(S - N_b) - V_a N_a - A_a N_a N_b, \\ 0 &= f(S - N_a) - V_b N_b - A_a N_a N_b. \end{aligned} \tag{12.3}$$

With the approximation $V_b = W_b + f \approx f$, we again find

$$N_a = 0, \quad N_b = S. \tag{12.4}$$

This trivial result reflects the fact, that as long as (the least) hopping for the type-b particles is not activated, in the stationary state they cover the complete surface and prevent the occurrence of any recombination event. Obviously, we can extend these findings to the case $f_b > f_a$. If even more than half of the

impinging particles are of the strongly-bound type, the stationary state has to be a surface completely covered with type-b particles.

In contrast to the single-species systems with rate disorder, excluding LH-rejection from the model, would change the result dramatically. Then, especially in the whole temperature region $T_a^{\text{low}} < T < T_b^{\text{low}}$, a-particles could impinge on sites occupied by a b-particle and take it away by forming a ab-dimer, leaving an empty site on the surface that could be occupied by another impinging a-particle and thus facilitating ab-dimer formation by two impinged particles.

Only when hopping of type-b particles is activated, the surface coverage by the b-particles drops below unity and allows the impingement of a-particles, which then leads to formation of ab- and b_2-dimers. Unfortunately, we found no meaningful analytical rate equation solutions in these temperature regimes. Concluding we can say that for multiple-species models with $f_b \geq f_a$, the temperature window of efficient molecule production is determined by the energy parameters of the strongly bound species, solely. It turns out, that the case $f_a > f_b$ is much more subtle to analyze and we have to invest further effort.

The only case, that can be solved in a closed form, is the degenerated case of two species with exactly the same binding and hopping energies. Constraining to the case of equal fluxes $f_a = f_b \equiv f$, we find the following highly symmetric set of rate equations for the stationary state

$$\begin{aligned} 0 &= f(S - N_a - N_b) - WN_a - AN_aN_b - AN_aN_b - 2AN_a^2, \\ 0 &= f(S - N_a - N_b) - WN_b - AN_aN_b - AN_aN_b - 2AN_b^2, \end{aligned} \tag{12.5}$$

where we abbreviated $A_a = A_b = A$ and $W_a = W_b = W$. Since the fluxes, hopping and desorption rates are equal for both species are equal, also the solution has to reflect this symmetry and we can conclude $N_a = N_b \equiv N$ with

$$0 = fS - (W + 2f)N - 4AN^2. \tag{12.6}$$

This corresponds to a homogeneous system (see equation (8.8)) with particle number $\tilde{N} = 2N$, a desorption rate $\tilde{W} = W/2$ and a hopping rate $\tilde{A} = A/2$ and we can read of the solution

$$\begin{aligned} N &= -\frac{W + 2f}{8A} + \frac{W + 2f}{8A}\sqrt{1 + \frac{16fa}{(W + 2f)^2}}, \\ \eta &= \frac{2AN^2}{fS} = \frac{1}{2} - \frac{(W + 2f)^2}{16fa}\left(\sqrt{1 + \frac{16fa}{(W + 2f)^2}} - 1\right), \end{aligned} \tag{12.7}$$

where η is the efficiency of all three reactions of a_2-, b_2- and ab-formation. We will see, that the here anticipated formula of η is in this special case independent of the choice of the efficiency. The possible choices of η will be discussed in the next section 12.1.1. The solution (12.7) is confirmed by numerical calculations in section 12.2.

We can even go a step further and expand to the case $f_a \neq f_b$. The steady state rate equations for this case read

$$\begin{aligned} 0 &= f_a(S - N_a - N_b) - WN_a - 2AN_aN_b - 2AN_a^2, \\ 0 &= f_b(S - N_a - N_b) - WN_b - 2AN_aN_b - 2AN_b^2. \end{aligned} \tag{12.8}$$

As the activation energies of both species are the same, the amount of particles of either species is determined by the incoming particle fluxes and their relation dictates that of the particle numbers, such that $N_a/N_b = f_a/f_b$. Inserting this relation into (12.8) we find an effective homogeneous system for the particle number $\tilde{N} = N_a(f_a + f_b)/f_a = N_a + N_b$,

$$0 = f_a(S - \tilde{N}) - \tilde{W}\tilde{N} - 2\tilde{A}\tilde{N}^2, \tag{12.9}$$

with desorption rate $\tilde{W} = Wf_a/(f_a + f_b)$ and hopping rate $\tilde{A} = Af_a/(f_a + f_b)$. Using the solution of the homogeneous system we find for the particle numbers of the two species the following expression

$$\begin{aligned} N_a &= \frac{f_a}{f_a + f_b}\tilde{N} \\ &= \frac{f_a}{f_a + f_b}\frac{W + f_a + f_b}{8A}\left(-1 + \sqrt{1 + \frac{f_a + f_b}{f_a}\frac{8f_a a}{(W + f_a + f_b)^2}}\right), \\ N_b &= \frac{f_b}{f_a + f_b}\tilde{N} \\ &= \frac{f_b}{f_a + f_b}\frac{W + f_a + f_b}{8A}\left(-1 + \sqrt{1 + \frac{f_a + f_b}{f_a}\frac{8f_a a}{(W + f_a + f_b)^2}}\right). \end{aligned} \tag{12.10}$$

The efficiency of the effective homogeneous system, given by $\eta_{\text{e.h.s.}} = 2\tilde{A}\tilde{N}/(f_a S)$, yields in terms of W and $a = AS$

$$\begin{aligned} \eta_{\text{e.h.s.}} = 1 &- \frac{f_a}{f_a + f_b}\frac{(W + f_a + f_b)^2}{4f_a a} \cdot \\ &\cdot \left(-1 + \sqrt{1 + \frac{f_a + f_b}{f_a}\frac{8f_a a}{(W + f_a + f_b)^2}}\right) \end{aligned} \tag{12.11}$$

We will discuss the efficiency values (and their relation) of the three possible reactions in section 12.2 after the discussion on possible definitions, which we will turn to now.

12.1.1 Efficiency definitions

While for the single-species systems, the definition of the efficiency was straightforward, the situation is more involved for multiple-species systems. In the single-species case, the efficiency is obtained by relating the particle number leaving the surface as part of a molecule to the total incoming particle flux. For multiple reactions, we can choose to define an efficiency for each process separately or for the whole surface. Both definitions are meaningful and which one to choose depends on the imposed questions.

It is possible to define the *total* efficiency of the whole surface by relating the sum over all reaction rates to the sum over all incoming fluxes,

$$\eta_{\text{tot}} = \frac{2\sum_i R_i}{S\sum_j f_j} = \sum_i \frac{2R_i}{S\sum_j f_j}, \tag{12.12}$$

where $\sum_i R_i$ sums over all possible reaction rates of the system and $\sum_j f_j$ is the total incoming particle flux. Then we get a quantity with values between

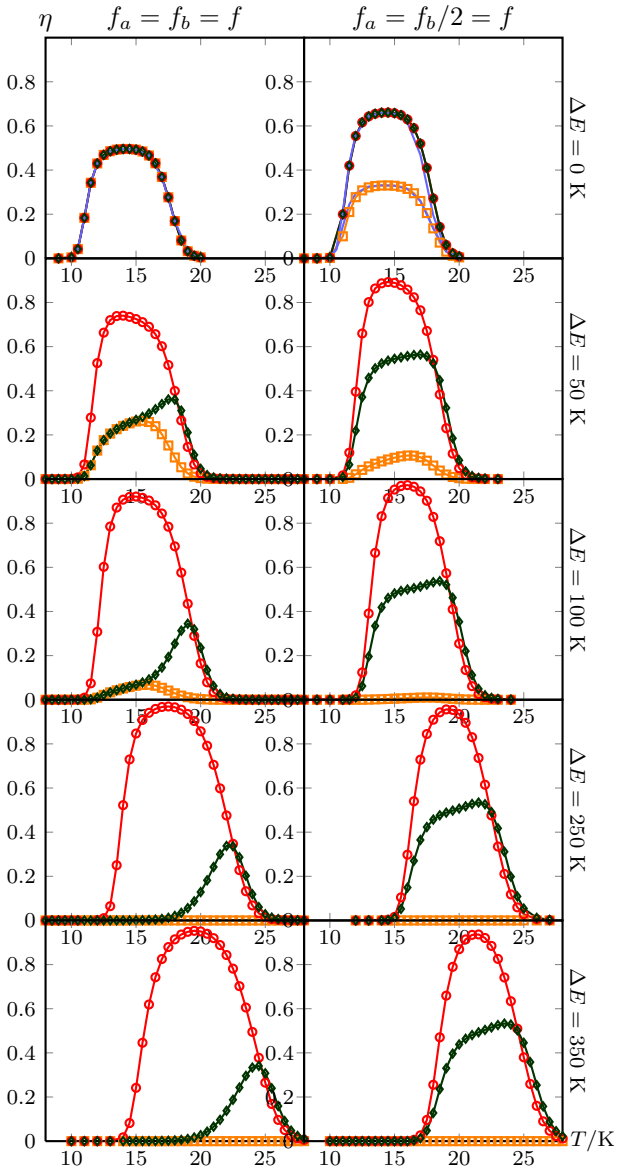

Figure 12.1: Temperature-dependence of the efficiency for different particle fluxes: homogeneous reactions between particles of type a: $a + a \rightarrow a_2$ (orange, squares), homogeneous reactions between particles of type b: $b + b \rightarrow b_2$ (darkgreen, diamonds), and heterogeneous reactions $a+b \rightarrow ab$ (red, circles), for changing values of $E_{W_b} - E_{W_a} =$ (0K, 50K, 100K, 250K, 350K) from top to bottom. For species a, the standard parameters for hydrogen on amorphous carbon are adopted. For species b, only binding and hopping energies are changed, all other parameters are identical to species a, so especially $E_{W_\alpha} - E_{a_\alpha} =$ const. here. The columns refer to $f_a = f_b = f \equiv 7.3 \times 10^{-9}/s$ (left column) and $f_a = f_b/2 = f$ (right column). We used the relative efficiency assignment throughout (see section 12.1.1). In the graphic for the energetically degenerated systems (upper left and upper right) also the analytical solution is plotted (blue line), which coincides perfectly with the numerical results.

zero and unity, indicating what fraction of the incoming particles react on the surface regardless of their type and the reactions. The individual summands of this definition can be interpreted as the relative frequency with which molecules of a specific type are produced on the surface.

The alternative approach is to assign a *relative* efficiency, that is an efficiency for each of the reactions, separately. It gives information about how efficient a single reaction is, compared to the individual maximal amount of molecules that can be produced under the given flux constraints. For each reaction this efficiency is defined as the reaction rate divided by product of the minimal individual flux of the involved species, the number of species, and the number of surface sites.

$$\eta_{\mathrm{rel},\alpha\beta} = \frac{2R_{\alpha\beta}}{Sh \min_{i\in\{\alpha,\beta\}} f_i}, \tag{12.13}$$

where h is the number of species involved in the reaction (so $h = 1$ for single-species reactions and $h = 2$ for reactions involving two species). The fact that several reactions may compete for one particle species is reflected in the efficiency values of this definition. But the definition does not reflect the possibility that not all impinging particles can participate in the reaction due to a difference in the particle flux relations and the stoichiometric particle relations of the product(s).

The two efficiency choices coincide if all incoming particle fluxes are equal.

12.2 Numerical results

To solve the full rate equation system (12.1), we opted for a direct numerical solver using `python` and `mathematica`. In principle, the system can straightforwardly be extended to any number and kind of different reactions among the species. The results are displayed in figure 12.1 for the standard parameters of hydrogen atoms on amorphous carbon and another generic species with a different binding (and hopping) energy but same parameters else.

For $\Delta E = E_{W_b} - E_{W_a} \geq 250\mathrm{K}$ we see that no dimers of type a_2 are formed on the surface, whereas for smaller binding energy differences at least a small amount is produced. This is due to the fact that for the very small binding energy differences, hopping of type-b particles is activated before $T_a^{\max}$ is reached, so there is a temperature regime, where both species are mobile and a sufficient quantity of both is present on the surface because the coverage of the strongly bound species drops significantly below unity. The formation of b_2-molecules is suppressed (compared to the formation ab-dimers) because at temperatures where the b-particles are mobile, the a-particles impinging on the empty lattice sites react with the b-particles due to their very high mobility. The more mobile the b-particles become, the more b_2-molecules can form before the b-particles are taken away by the type-a particles. This dynamic is only limited by the growing desorption rate of the b-particles, reflected by the alignment of the green (b_2-dimers) to the red (ab-dimers) curve for high temperatures. The numerical results for the completely degenerated system coincide with the analytical calculations from equation (12.7).

In the plots we used the *relative* efficiency definition. So, an efficiency value of unity indicates that all particles from the species with the lowest incoming flux are consumed in the reaction. A diminished maximal efficiency value indicates

that different reactions compete for one of the species such that not all available particles of that species are channeled to the considered reaction.

We can estimate the critical binding energy difference at which no more a_2-dimers are produced. Considering the characteristic temperatures of the corresponding homogeneous systems, the ΔE where the efficiency of the strongly bound species reaches zero for low temperatures $\eta_{b_2} \approx 0$ (which is for the parameters employed here roughly at $T_{\eta_b=0} = T_b^{\text{low}} - 1\text{K}$) determines this threshold. Namely, when $T_{\eta_{b_2}=0} = T_a^{\max}$ no more dimers of type a_2 are produced because the b-particles occupy the whole surface at temperatures where the a-particles would be mobile and their single-species coverage would be sufficiently high. For the here employed energy values of amorphous carbon, this corresponds to $\Delta E \approx 250$ K. We can confirm the rate equation results (12.4) stating that with growing ΔE, the whole efficiency window of molecule production (no matter what type) is shifted to higher temperatures and is determined by the binding and hopping energies of the strongly bound species alone. In particular, the width of the efficiency window is determined by $E_{W_b} - E_{a_b}$. For $f_a \leq f_b$, the relative amounts of molecules produced (of either type) depend on the ratio of the incoming particle fluxes.

For the energetically degenerated case the relation between the efficiency values of the three reactions can be estimated by a simple argument. As the energy parameters of both species are identical, we argued in section 12.1 that the relation of the particles numbers of the species is (for activated hopping!) determined by the relation of their fluxes, $N_a/N_b = f_a/f_b$, only. Inserting this into the (relative) efficiency definitions yields $\eta_{\text{rel},a_2} = 2AN_a^2/(f_aS)$, $\eta_{\text{rel},b_2} = \eta_{\text{rel},a_2} \cdot f_a/f_b$, and $\eta_{\text{rel},ab} = \eta_{\text{rel},a_2} \cdot f_a/f_b = \eta_{\text{rel},b_2}$. To determine the efficiency η_{rel,a_2}, we remember, that the particle numbers N_a and N_b were computed using the solution of a homogeneous surface with $\tilde{N} = N_a(f_a + f_b)/f_a$ particles, flux f_a, hopping rate $\tilde{A} = A/2$ and desorption rate $\tilde{W} = W/2$. We already calculated the efficiency $\eta_{\text{e.h.s.}}$ of this effective homogeneous system in equation (12.11). Combining all the relations this yields for the efficiencies of a_2-, b_2-, and ab-dimer production

$$\begin{aligned}
\eta_{\text{rel},a_2} &= \frac{f_a}{f_a + f_b}\eta_{\text{e.h.s.}}, \\
\eta_{\text{rel},b_2} &= \frac{f_b}{f_a + f_b}\eta_{\text{e.h.s.}}, \\
\eta_{\text{rel},ab} &= \frac{f_b}{f_a + f_b}\eta_{\text{e.h.s.}}.
\end{aligned} \tag{12.14}$$

Evaluating these expressions for the parameters employed in the left and right upper plots of figure 12.1 we gain for the efficiencies at the single-species system's maximum temperature $T^{\max}$ in the case $f_a = f_b = f$

$$\eta_{\text{rel},a_2}^{\max} = \eta_{\text{rel},b_2}^{\max} = \eta_{\text{rel},ab}^{\max} = \frac{1}{2}, \tag{12.15}$$

and for $2f_a = f_b = 2f$ the efficiencies yield

$$\eta_{\text{rel},a_2}^{\max} = \frac{1}{3}, \quad \eta_{\text{rel},b_2}^{\max} = \frac{2}{3}, \quad \eta_{\text{rel},ab}^{\max} = \frac{2}{3}. \tag{12.16}$$

These results are fully confirmed by the numerical solutions.

12.3 Conclusions and outlook

The short analysis of a generic multiple-species scenario reveals a highly complex system, that can in principle be solved analytically on the level of rate equations. In contrast to the single-species systems with quenched disorder in the rates, here no general temperature regimes with a meaningful simple analytical solution can be identified in the case $f_a \leq f_b$. Only two special cases are amenable to simple argumentations: the (trivial) regime of low temperatures where none or only one of the species is mobile and in the stationary state the surface is covered completely by the strongly-bound species, and the energetically degenerated system, where both species possess the same activation energies. For this latter case, we gave a closed solution by using the analogy to a single-species homogeneous system.

As we have seen, the relative amounts of molecules produced strongly depend on the system parameters. Thus it seems reasonable to concentrate first on important realistic system like the production of H_2O, CO_2, CH_4 or CH_4O . For all four molecules evidence exists, that a considerable amount of them is produced on interstellar surfaces [36, 60].

Concerning the methods, rate equations can in principle be used to find reaction efficiencies. As illustrated, the number of equations needed to describe such systems grows with the number of reactants. Garrod et. al. [36] use modified rate equations to compute the formation of methanol. Cuppen et. al. [24] use Monte Carlo simulations for a specific multiple-species system including layering effects on the surface. Also a master equation approach on a moderately complex level has been employed to solve a small reaction network based on H, D, O and CO [78, 77].

For large reaction networks with a lot of reactants, the moment equations method is well-suited and has already been used to investigate on the methanol network [5]. In the moment equations approach only $2n$ equations have to be solved for n reactant species in the system. For small networks also the multiplane method can be used [61], which disassembles the whole network into smaller non-connected subnetworks.

To find an analytic description for application-relevant, non-generic reactions, it will be necessary to include also higher order reactions into the rate equations, where the product of one reaction is an educt of another reaction.

Additionally it will be interesting to see the system's behavior in a non-stationary state, when at low temperatures the system is not completely covered with the species bound most strongly. KMC simulations could serve as a good reference for all the mentioned methods.

From our point of view, it should be possible to include rate disorder into multiple-species systems without facing fundamental problems.

Conclusions

Part I: Robustness in quasispecies models. We analyzed the effect of robustness against deleterious mutations on the mean fitness of quasispecies populations. Concentrating on permutation-invariant fitness landscapes, the hypercubic phase space was mapped onto the one-dimensional Hamming space. Robustness was then modeled as a plateau-shaped fitness landscape. With the help of a large deviations ansatz we found a correspondence between the populations stationary state equation and a Schrödinger-type equation. Exploiting this analogy, we derived a formula for the mean fitness in the limit of infinite sequence length and finite size correction terms. The results hold for both, smooth and non-smooth fitness landscapes and improve the agreement between numerical and analytical solutions significantly. In principle it is possible to extend this analysis to more than first order in the sequence length. Furthermore we showed, that the fitness regime predicted by Gerland and Hwa [39] does not exist. Applying our findings to the question of the optimal plateau shape for finite sequence lengths, we find that a broad plateau can provide a higher mean fitness to the population than a smaller but higher one. In the literature this phenomenon is often referred to as "survival of the flattest".

In addition to the mesa-shaped fitness landscapes, which can be considered as an extreme kind of epistasis, a more general class of epistatic fitness landscapes concerning the error threshold existence was analyzed. Here, we could improve on a result by Wiehe [86] by application of the earlier findings. As a result, we find diminishing epistasis to be necessary but not sufficient to ensure the error threshold existence.

Recently, Ancliff and Park [1] developed a new approach using spin coherent state representations. The simplicity of this method — compared to the existing ones — is promising, moreover as the derivation of finite size corrections emerges naturally and the path integral formulation is suited for the description of the population dynamics.

Part II: Molecule formation on interstellar dust grain surfaces with quenched disorder The question of disorder enhancing a surface's efficiency in molecule production has been answered satisfactorily. The employed minimalistic model was analyzed by means of rate equations and kinetic Monte Carlo simulations. We started with the analysis of a system with binary disorder. It turned out, that the mixing of different binding energies on one surface enhances it's efficiency in temperature regions where the corresponding homogeneous systems do not perform well at all. The reason lies in the different roles that are assigned to the two types of sites. The shallow sites provide mobility to the particles, while the deep sites trap particles and thus increase the surface

coverage. Then dimers are formed by a particle hopping from a shallow onto a deep site and recombining with a particle that has already been trapped there. Depending on the energies of the sites and their quantity, this mechanism leads to a uniformly high efficiency in the whole intermediate temperature regime. We gave an analytical formula for the efficiency value of this plateau. It turned out that this concept of mobility and trapping can be extended to the other binding energy distributions investigated. As a result we provide (temperature-dependent) mappings from discrete and continuous binding distributions to effective binary systems that reproduce the efficiency of the original one.

Concerning the discrete distributions, this mapping involved the validity of a rate equation description and well-separated binding energies. Yet, under these constraints, the mapping is easy and quick to apply.

For the continuous binding energy distributions we even went a step further and could define a mapping to an effective binary system using the system temperature and the distribution only. Thereby the energies are also grouped into effectively shallow and deep wells by a cutting energy. As we showed, this mapping is as well applicable to the discrete distributions.

Nevertheless, the contribution of our findings to astrophysical applications depends on estimating binding energies and topologies of relevant surfaces under (simulated) interstellar conditions. The energy values we used for the KMC simulations and numerical solutions are believed to be astrophysically relevant. The output of our models in terms of temperature-dependent efficiency points into the right direction with broader temperature windows of high efficiency and at higher temperatures compared to the homogeneous system results (with the same parameters).

The question of rate disorder on surfaces is closely related to that of geometric effects. Lattice distortion has been studied [65], as well as a different coordination number, but nevertheless the system's translational symmetry has always been sustained. In addition to rate disorder effects, it would be interesting to see the influence of disorder in the connectivity of the sites. The surface can then be interpreted as a network of binding sites of integer or fractal dimension. In this way it can be accounted for e.g. holes that can be accessed from more than four or six sites or for sites that cannot be accessed from all direct neighbors.

Additionally, we took a brief look on a generic multispecies system. It turned out, that the numerical solution of the rate equations is delicate and susceptible to small numerical errors. Clearly, more research in this direction need to done. Solving multispecies reactions on surfaces will be a great improvement in understanding interstellar molecule formation in general since the surface products re-enter the gas chemistry network as educts and thus have a strong influence on the solution of the whole gas-grain system.

Research on the multispecies systems should be continued as the majority of chemical reactions involves more than one particle species. The results will not only be of importance for interstellar molecule formation. The rate equations approach seems to be promising, at least for large grains and sufficiently high fluxes. It is accessible to direct numerical solvers and all kinds of reactions can be included straightforwardly. Nevertheless other promising approaches like moment equations exist that are well-suited for large reaction networks.

Regarding the analysis of homogeneous dimer formation on disordered surfaces we feel that we have substantially contributed to the theory. The main mechanism for molecule formation has been identified and quantitative results for different

binding energy distributions have been derived, that are in accordance with previous suggestions.

General remarks. We have exemplified that reaction-diffusion systems appear in very different contexts. In the quasispecies model, the reaction-diffusion character appeared on the level of effective model description, while for the problem of interstellar molecule formation the diffusion and reactions naturally appear on the microscopic level. The solvability of reaction-diffusion systems strongly depends on the exact shape of the reaction term, as encountered in this thesis. Though we only analyzed two applications, the systems considered here already proved their relevance and we hope to see some of the open questions, especially on the multispecies systems, pursued in the future.

Part III

Additional material

Appendix A

Appendix

A.1 The large deviations approach

We start by symmetrizing the eigenvalue problem (2.18). The discrete analogue of the transformation (3.3) is

$$Q_k = \binom{L}{k}^{1/2} P_k^*, \tag{A.1}$$

which leads to

$$\begin{aligned} \Lambda Q_k = (w_k - \gamma) Q_k + \mu \sqrt{(L-k)(k+1)}\, Q_{k+1} \\ + \mu \sqrt{(L-k+1)k}\, Q_{k-1}. \end{aligned} \tag{A.2}$$

Following [73], we now perform the continuum limit by making a large deviations ansatz for Q_k,

$$Q_k = Q_{xL} = \psi(x) = \exp[-\epsilon^{-1} u(x)] \tag{A.3}$$

with $\epsilon = 1/L$. Inserting this into (A.2) one finds

$$(\Lambda - f(x) + \gamma)\psi = 2\gamma \sqrt{x(1-x)}\, \cosh[u']\psi. \tag{A.4}$$

Cancelling ψ on both sides yields a Hamilton-Jacobi equation for the 'action' $u(x)$, with $u' = du/dx$ playing the role of a canonical momentum [73]. In order to cast (A.4) into the form of a Schrödinger equation, we expand the momentum-dependent factor to quadratic order, $\cosh(u') \approx 1 + (u')^2/2$, and make use of the relation

$$(u')^2 = \epsilon^2 \psi^{-1} \frac{d^2\psi}{dx^2}, \tag{A.5}$$

which follows from (A.3) to leading order in ϵ. Inserting this into (A.4) results in (3.11).

A.2 Singular-value decomposition

The singular-value decomposition is a decomposition of an arbitrary real or complex $m \times n$ matrix A into three matrices of the shape

$$A = U D V^T \ .$$

The matrix D is symmetric and diagonal, and U and V are unitary matrices. If A is invertible, then

$$A^{-1} = UD^{-1}V^T \ .$$

The entries of D are called the singular values and give informations about the characteristics of the matrix A, similar to the eigenvalues.
The condition number, calculated by `Octave`, is the product of the largest singular values of A and A^{-1}. This is the same as the ratio of the largest and the smallest singular value of A itself. The condition number is a measure for the magnitude of mixing of the numerical scales. The bigger the condition number is, the more are different scales mixed, and the more likely errors in the calculation occur. Thus, the condition number is a measure of stability of a matrix towards slight pertubations of matrix elements. Stability becomes important when the matrix has to be diagonalised numerically. Numerical methods use iterative procedures. As more iterations are needed the more off-diagonal elements exist, the bigger they are and the farer they are away from the diagonal, stability of the matrix is essential for an exact numeric result.

A.3 Alphabet sizes $\mathcal{A} > 2$

The results presented in the main part are all valid for an alphabet size of $\mathcal{A} = 2$. We here want to illustrate, how these results can be generalized to arbitrary alphabet sizes in the case of a uniform mutation rate μ and a fitness that depends only on the (generalized) Hamming distance to the wild type. For the mutation rate this especially means, that any letter at any site is changed into any other one with the same overall rate, and for the fitness it means, that it does not matter into which direction (into which letter) the mutation occured. As a consequence, sequences differing at a certain position can have the same Hamming distance to the wild type. Again, this is an oversimplifying model, but suffices for our purpose of sketching the main idea. More sophisticated mutation schemes can e.g. be found in [38]. For an alphabet size of $\mathcal{A}$, the eigenvalue problem of the Crow-Kimura equation (2.18) then reads

$$\Lambda P_k^* = \left[w_k - (\mathcal{A}-1)\gamma \left(L - k + \frac{k}{\mathcal{A}-1} \right) \right] P_k^* . \tag{A.6}$$

For large $L \to \infty$ this problem has been solved by [2, 38, 37], and we find the largest eigenvalue given by the generalized maximum principle

$$\Lambda = \max_{x\in[0,1]} \left\{ f(x) - (\mathcal{A}-1)\gamma \left[\left(1 - \frac{(\mathcal{A}-2)x}{\mathcal{A}-1} \right) - \frac{2}{\sqrt{\mathcal{A}-1}} \sqrt{x(1-x)} \right] \right\} . \tag{A.7}$$

Applying this formula to a mesa landscape with relative mesa width x_0, we find the critical plateau height for population localization

$$w_0^c = \gamma(\mathcal{A}-1) \left[\left(1 - \frac{(\mathcal{A}-2)x_0}{\mathcal{A}-1} \right) - \frac{2}{\sqrt{\mathcal{A}-1}} \sqrt{x_0(1-x_0)} \right] . \tag{A.8}$$

Hardly surprising, we find the critical plateau height to increase with the alphabet size (x_0 fixed) and to decrease with x_0 (fixed $\mathcal{A}$) until $w_0^c = 0$ at $x_0 = 1 - 1/\mathcal{A}$. For $\mathcal{A} = 2$ we regain the earlier presented results of section 2.5.

Glossary

Part I

Quasispecies models: description of very large (infinite) population of asexual (self-replicating) individuals. In the long-time limit the quasispecies corresponds to the localized eigenvector of the system, specified by the fitness and mutation probability/rate.

mutation: in general, mutation means the alteration of a genomic sequence due to copying errors during replication. There are different types of mutations, e.g. point mutations (also called substitutions), where only one letter is changed, insertion, where additional letters are inserted into the sequence, or deletions, encoding the opposite process of insertion.

selection: the favorization of certain genotypes concerning the number of offspring. The better adapted to the environment, the more offspring an individual of a population produces during replication.

genetic drift: finite population size effect: the frequency of the different types of information sequences in the population varies due to random sampling (in the reproduction phase).

recombination: During sexual reproduction the offspring gets a new combination of information strings by exchanges between the latter.

gene expression: During the expression of a gene (special part of the DNA), the information encoded in the gene is processed to a functional product like proteins or RNA.

CK model (parallel model): Quasispecies model formulated in continuous time, in which mutations and selection occur parallel to each other. Can be derived from the →Eigen model by sending the generation time to zero.

Eigen model (coupled model): Quasispecies model in discrete time (that is generation time) for haploid asexual organisms in which mutations only occur as copying errors during replication.

fitness landscape: gives the degree of adaptation to the environment (typically measured by the amount of offspring produced by an individual) as function of the information sequence.

permutation invariant (fitness landscape): the degree of adaptation only depends on the →Hamming distance to the best adapted sequence. Hence permutation invariant fitness landscapes are effectively onedimensional

epistasis: the interplay of different mutations: the number of mutations away from the wildtype influences the amount of fitness reduction, the next mutation will produce. Epistasis refers to both decreasing and increasing functions of the number of mutations.

robustness: The resiliance of a population to the influence of mutation.

haploid/diploid: individuals of an haploid population possess one copy of their genome (e.g. bacteria - except special types), whereas in diploid populations, the individuals carry two copies of their genetic information (e.g. mammals).

asexual/sexual populations: in asexual population all individuals are equal and every individual can reproduce on its own (e.g. via cell division), whereas in sexual populations, two kinds of individuals exist (male and female) and both of them together are needed to produce offspring.

Hamming distance: number of letters in which an individuals sequence differs from the best adapted sequence, the so-called wildtype.

ancestral population distribution: equilibrium population distribution of the backwards time process (given population evolution model).

Part II

interstellar medium (ISM): matter between the star systems of a galaxy. The densest parts of the ISM are called *molecular clouds*.

physisorption: binding of atoms/molecules onto a surface by means of the van-der-Waals force.

chemisorption: chemical binding of atoms/molecules to a surface. Typically binding energies are higher for chemisorbed particles than for physisorbed ones.

NESS: non-equilibrium stationary state.

Langmuir-Hinshelwood rejection (LH-rejection): effect that particles from the gas cannot impinge onto lattice sites already occupied by another particle.

Frequently used symbols

Part I

symbol	meaning
$\sigma(s_1, .., s_L)$	information string (sequence) of an individual
$s_i \in \mathcal{A}$	letters of the sequence σ
$\mathcal{A}$	alphabet from which the letters are drawn
μ	mutation rate
μ_{tr}	error threshold
μ_{s}	selection threshold
$\gamma = \mu L$	mutation rate per sequence
L	sequence length
k	(absolute) Hamming distance
$x = k/L$	relative Hamming distance
k_0, x_0	absolute and relative plateau width
$P_\sigma(t)$, P_k, $P(x)$	population distribution depending on sequence and time, abs. Hamming distance, and rel. Hamming distance, respectively
P^*_σ, P^*_k, $P(x)^*$	equilibrium population distributions
a_k, $a(x)$	ancestral distribution
a^*_k, $a(x)^*$	ancestral distribution in equilibrium
$f(\sigma)$, f_k	Wrightian fitness function, depending on the sequence or the Hamming distance, respectively
$w(\sigma)$, w_k	Malthusian fitness function, depending on the sequence or the Hamming distance, respectively

Part II

symbol	meaning
T	temperature of the grain surface / lattice
T^{low}	temperature where the efficiency starts to become non-zero for a homogeneous surface with given binding energy
T^{up}	temperature where the efficiency drops to zero again for a homogeneous surface with given binding energy
T^{max}	temperature where the efficiency reaches its maximum for a homogeneous surface with given binding energy
f	flux onto each lattice site (of a grain)
L_1, L_2	side lengths of the lattice
$S = L_1 \cdot L_2$	number of sites on the grain/lattice
N	(mean) number of particles on the grain/lattice
S_i	number of sites of a certain type of sites
N_i	(mean) number of particles on type of sites i
N_a	(mean) number of particles of species a
ν	attempt frequency (for hopping and desorption) of the particles
η	efficiency of the grain/lattice
R	reaction rate
E_{a_i}	energy needed for hopping from site i
E_{W_i}	energy needed for desorption from site i also called binding energy
a_i	hopping rate for lattice site i
W_i	desorption rate for lattice site i
$A_i = a_i/S$	sweeping rate
$\Delta E = E_{W_j} - E_{W_i}$	difference in binding energy for different types of sites
$\ell_{\mathrm{rw}} = \sqrt{a_i/W_i}$	(continuous time) random walk length on sites of type i

Bibliography

[1] M. Ancliff and J.-M. Park. Spin Coherent State Representation of the Crow-Kimura and Eigen Models of Quasispecies Theory. *J. Stat. Phys.*, 143:636–56, 2011.

[2] E. Baake, M. Baake, A. Bovier, and M. Klein. An asymptotic maximum principle for essentially linear evolution models. *J. Math. Biol.*, 50:83–114, 2005.

[3] E. Baake and W. Gabriel. Biological evolution through mutation, selection, and drift: An introductory review. *arXiv:cond-mat*, 9907372v1, 1999.

[4] E. Baake and H.-O. Georgii. Mutation, selection, and ancestry in branching models: a variational approach. *J. Math. Biol.*, 54:257, 2007.

[5] B. Barzel and O. Biham. Efficient Simulations of Interstellar Gas-Grain Chemistry using Moment Equations. *ApJ Lett.*, 658(1):L37–40, March 2007.

[6] B. Barzel and O. Biham. Efficient stochastic simulations of complex reaction networks on surfaces. *J. Chem. Phys.*, 127(14):144703, 2007.

[7] W. Bateson. Mendel's principles of heredity. *Cambridge Univ. Press*, 1909.

[8] D. ben Avraham and S. Havlin. *Diffusion and Reactions in Fractals and Disordered Systems*. Cambridge University Press, 2000.

[9] J. Berg, S. Willmann, and M. Lässig. Adaptive evolution of transcription factor binding sites. *BMC Evolutionary Biology*, 4:42, 2004.

[10] S. Bershtein, M. Segal, R. Bekerman, N. Tokuriki, and D. S. Tawfik. Robustness-epistasis link shapes the fitness landscape of a randomly drifting protein. *Nature*, 444:929–932, 2006.

[11] O. Biham, I. Furman, N. Katz, V. Pirronello, and G. Vidali. H_2 formation on interstellar grains in different physical regimes. *Mon. Not. R. Astron. Soc.*, 296(4):869–872, 1998.

[12] O. Biham, I. Furman, V. Pirronello, and G. Vidali. Master equation for hydrogen recombination on grain surfaces. *ApJ*, 553(2):595–603, 2001.

[13] O. Biham, J. Krug, A. Lipshtat, and T. Michely. Reaction kinetics in a tight spot. *Small*, 1(5):502–504, 2005.

[14] O. Biham and A. Lipshtat. Exact results for hydrogen recombination on dust grain surfaces. *Phys. Rev. E*, 66(5):056103, November 2002.

[15] J. Bloom, Z. Lu, D. Chen, R. Alpan, O. Venturelli, and F. Arnold. Evolution favors protein mutational robustness in sufficiently large populations. *BMC Biology*, 5:29, 2007.

[16] V. Buch and R. Czerminski. Eigenstates of a quantum-mechanical particle on a topologically disordered surface: H(D) atom physisorbed on an amorphous ice cluster $(H_2O)_{115}$. *J. Chem. Phys.*, 95(8):6026–6038, October 1991.

[17] C. Burch and L. Chao. Evolvability of an RNA virus is determined by its mutational neighbourhoud. *Nature*, 406:625–28, 2000.

[18] P. Caselli, E. Keto, L. Pagani, Y. Aikawa, U. A. Yıldız, F. F. S. van der Tak, M. Tafalla, E. A. Bergin, B. Nisini, C. Codella, E. F. van Dishoeck, R. Bachiller, A. Baudry, M. Benedettini, A. O. Benz, P. Bjerkeli, G. A. Blake, S. Bontemps, J. Braine, S. Bruderer, J. Cernicharo, F. Daniel, A. M. di Giorgio, C. Dominik, S. D. Doty, P. Encrenaz, M. Fich, A. Fuente, T. Gaier, T. Giannini, J. R. Goicoechea, Th. de Graauw, F. Helmich, G. J. Herczeg, F. Herpin, M. R. Hogerheijde, B. Jackson, T. Jacq, H. Javadi, D. Johnstone, J. K. Jørgensen, D. Kester, L. E. Kristensen, W. Laauwen, B. Larsson, D. Lis, R. Liseau, W. Luinge, M. Marseille, C. McCoey, A. Megej, G. Melnick, D. Neufeld, M. Olberg, B. Parise, J. C. Pearson, R. Plume, C. Risacher, J. Santiago-García, P. Saraceno, R. Shipman, P. Siegel, T. A. van Kempen, R. Visser, S. F. Wampfler, and F. Wyrowski. Water vapor toward starless cores: The Herschel view. *Astronomy and Astrophysics*, 521:L29, October 2010.

[19] S. Cazaux and A. G. G. M. Tielens. H_2 formation in the interstellar medium. *ApJ Lett.*, 575:L29–L32, 2002.

[20] S. Cazeaux, P. Caselli, V. Cobut, and J. Le Bourlot. The role of carbon grains in the deuteration of H2. *Astronomy and Astrophysics*, 348:495–508, 2008.

[21] M. Cencini, C. Lopez, and D. Vergni. Reaction-diffusion systems: Front propagation and spatial structures. *Lect. Notes Phys.*, 636:187, 2003.

[22] H. M. Cuppen and E. Herbst. Monte Carlo simulations of H_2 formation on grains of varying surface roughness. *Mon. Not. R. Astron. Soc.*, 361:565–576, 2005.

[23] H. M. Cuppen, S. Ioppolo, C. Romanzin, and H. Linnartz. Water formation at low temperatures by surface O2 hydrogenation II: the reaction network. *Physical Chemistry Chemical Physics*, 12:12077, 2010.

[24] H. M. Cuppen, E. F. van Dishoeck, E. Herbst, and A. G. G. M. Tielens. Microscopic simulation of methanol and formaldehyde ice formation in cold dense cores. *Astronomy and Astrophysics*, 508:275–287, December 2009.

[25] A. Dalgarno and J.H. Black. Molecule formation in the interstellar gas. *Rep. Prog. Phys.*, 39:573–612, 1976.

[26] J. A. G. M. de Visser et al. Perspective: Evolution and detection of genetic robustness. *Evolution*, 57:1959–1972, 2003.

[27] B. Drossel. Biological evolution and statistical physics. *Advances in Physics*, 50:209–295, March 2001.

[28] F. Dulieu, L. Amiaud, E. Congiu, J.-H. Fillion, E. Matar, A. Momeni, V. Pirronello, and J. L. Lemaire. Experimental evidence for water formation on interstellar dust grains by hydrogen and oxygen atoms. *Astronomy and Astrophysics*, 512:A30, March 2010.

[29] W. Ebeling, A. Engel, B. Esser, and R. Feistel. Diffusion and reaction in random media and models of evolution processes. *J. Stat. Phys.*, 37(3/4):369, 1983.

[30] M. Eigen. Selforganization of matter and the evolution of biological macromolecules. *Naturwissenschaften*, 58:465, 1971.

[31] A. Einstein. Über die von der molekularkinetischen Theorie der Wärme geforderte Bewegung von in ruhenden Flüssigkeiten suspendierten Teilchen. *Annalen der Physik*, 17:549–560, 1905.

[32] J. W. Evans and R. S. Nord. Random walks on finite lattices with multiple traps: Application to particle-cluster aggregation. *Phys. Rev. A*, 32(5):2926–2943, November 1985.

[33] R. A. Fisher. *The Genetical Theory of Natural Selection*. Claredon Press, Oxford, 1930.

[34] R. A. Fisher. The wave of advance of advantageous genes. *Ann. Eugenics*, 7:353, 1937.

[35] R.A. Fisher. The correlation between relatives on the supposition of mendelian inheritance. *Trans. R. Soc. Edinburgh*, 3:399–433, 1918.

[36] R. T. Garrod and T. Pauly. On the formation of CO2 and other interstellar ices. *The Astrophysical Journal*, 735:15, July 2011.

[37] T. Garske and U. Grimm. Maximum principle and mutation thresholds for four-letter sequence evolution. *J. Stat. Mech.*, page P07007, 2004.

[38] T. Garske and U. Grimm. A maximum principle for the mutation-selection equilibrium of nucleotide sequences. *Bull. Math. Biol.*, 66:397, 2004.

[39] U. Gerland and T. Hwa. On the selection and evolution of regulatory DNA motifs. *J. Mol. Evol.*, 55:386–400, 2002.

[40] R. J. Gould and E. E. Salpeter. The interstellar abundance of the hydrogen molecule. I. Basic processes. *ApJ*, 138(2):393–407, August 1963.

[41] N. J. B. Green, T. Toniazzo, M. J. Pilling, D. P. Ruffle, N. Bell, and T. W. Hartquist. A stochastic approach to grain surface chemical kinetics. *A&A*, 375:1111–1119, 2001.

[42] J. B. S. Haldane. A mathematical theory of natural and artificial selection. part v: Selection and mutation. *Proc. Camb. Phil. Soc.*, 23:838, 1928.

[43] E. Herbst. Chemistry in the interstellar medium. *Annu. Rev. Phys. Chem.*, 46:27–53, 1995.

[44] J. Hermisson, O. Redner, H. Wagner, and E. Baake. Mutation-selection balance: Ancestry, load, and maximum principle. *Theor. Pop. Biol.*, 62:9–46, 2002.

[45] H. G. Hixson, M. J. Wojcik, M. S. Devlin, and J. P. Devlin. Experimental and simulated vibrational spectra of H_2 absorbed in amorphous ice: Surface structures, energetics, and relaxations. *J. Chem. Phys.*, 97(2):753–767, July 1992.

[46] D. Hollenbach and E. E. Salpeter. Surface adsorption of light gas atoms. *J. Chem. Phys.*, 53:79–86, 1970.

[47] D. Hollenbach and E. E. Salpeter. Surface recombination of hydrogen molecules. *ApJ*, 163(1):155–164, January 1971.

[48] D. J. Hollenbach, M. W. Werner, and E. E. Salpeter. Molecular hydrogen in H_1 regions. *ApJ*, 163(1):165–180, January 1971.

[49] S. Ioppolo, H. M. Cuppen, C. Romanzin, E. F. van Dishoeck, and H. Linnartz. Water formation at low temperatures by surface O2 hydrogenation i: characterization of ice penetration. *Physical Chemistry Chemical Physics*, 12:12065, 2010.

[50] M. Kimura J. F. Crow. *An Introduction to Population Genetics Theory.* Harper and Row, New York, 1970.

[51] K. Jain and J. Krug. Adaptation in simple and complex fitness landscapes. In U. Bastolla, M. Porto, H. E. Roman, and M. Vendruscolo, editors, *Structural approaches to sequence evolution: Molecules,networks and populations.* Springer, Berlin, 2007.

[52] N. Katz, I. Furman, O. Biham, V. Pirronello, and G. Vidali. Molecular hydrogen formation on astrophysically relevant surfaces. *ApJ*, 522:305–312, 1999.

[53] M. Kimura and J. F. Crow. Evolution in asexual and sexual populations. *Am. Nat.*, 99:439, 1965.

[54] A.N. Kolmogorov, I. Petrovskii, and N. Piskunov. A study of the diffusion equation with increase in the amount of substance and its application to a biology problem. *Moskow Univ. Bull. Math. A*, 1:1, 1937.

[55] D. C. Krakauer and J. B. Plotkin. Redundancy, antiredundancy, and the robustness of genomes. *Proc. Nat. Acad. Sci. USA*, 99:1405–1409, 2002.

[56] J. Krug. Reaction kinetics in confined geometries: Lonely adatoms in space. *Phys. Rev. E*, 67:065102(R), 2003.

[57] I. Langmuir. The adsorption of gases on plane surfaces of glass, mica and platinum. *J. Am. Chem. Soc.*, 40(9):1361–1403, 1918.

[58] A. Lederhendler and O. Biham. Validity of rate equation results for reaction rates in reaction networks with fluctuations. *Phys. Rev. E*, 78(4):041105, 2008.

[59] I. Leuthäusser. Statistical mechanics of Eigen's evolution model. *J. Stat. Phys.*, 48:343, 1987.

[60] A. Lipshtat and O. Biham. Moment equations for chemical reactions on interstellar dust grains. *A&A*, 400(2):585–593, 2003.

[61] A. Lipshtat and O. Biham. Efficient simulations of gas-grain chemistry in interstellar clouds. *Phys. Rev. Lett.*, 93(17):170601, October 2004.

[62] A. Lipshtat, O. Biham, and E. Herbst. Enhanced production of HD and D2 molecules on small dust grains in diffuse clouds. *MNRAS*, 348:1055–1064, 2004.

[63] I. Lohmar. *Diffusion, Nucleation and Recombination in Confined Geometries.* PhD thesis, University of Cologne, 2009.

[64] I. Lohmar and J. Krug. The sweeping rate in diffusion-mediated reactions on dust grain surfaces. *Mon. Not. R. Astron. Soc.*, 370(2):1025–1033, 2006.

[65] I. Lohmar and J. Krug. Diffusion-limited reactions and mortal random walkers in confined geometries. *J. Stat. Phys.*, 134(2):307, January 2009.

[66] E. W. Montroll. Random walks on lattices. III. Calculation of first-passage times with application to exciton trapping on photosythetic units. *J. Math. Phys.*, 10:753, 1969.

[67] J. M. Park and M. W. Deem. Schwinger boson formulation and solution of the Crow-Kimura and Eigen models of quasispecies theory. *J. Stat. Phys.*, 125:975, 2006.

[68] L. Peliti. Quasispecies evolution in general mean-field landscapes. *Europhysics Letters*, 57:745, 2002.

[69] H. B. Perets, O. Biham, G. Manicó, V. Pirronello, J. Roser, S. Swords, and G. Vidali. Molecular hydrogen formation on ice under interstellar conditions. *ApJ*, 627:850–860, 2005.

[70] P. C. Phillips, S. P. Otto, and M. C. Whitlock. Beyond the average: The evolutionary importance of gene interactions and variability of epistatic effects. In J. B. Wolf, E. D. Brodie III, and M. J. Wade, editors, *Epistasis and the evolutionary process.* Oxford University Press, Oxford, 2000.

[71] H. Rollnik. *Quantentheorie I.* Vieweg, Wiesbaden, 1995.

[72] C. Romanzin, S. Ioppolo, H. M. Cuppen, E. F. van Dishoeck, and H. Linnartz. Water formation by surface o3 hydrogenation. *The Journal of Chemical Physics*, 134:084504, 2011.

[73] D. B. Saakian. A new method for the solution of model of biological evolution: Derivation of exact steady-state distributions. *J. Stat. Phys.*, 128:781–798, 2007.

[74] D. B. Saakian and C.-K. Hu. Exact solution of the Eigen model with general fitness functions and degradation rates. *Proc. Nat. Acad. Sci. USA*, 103:4935–4939, 2006.

[75] P. Schuster and J. Swetina. Stationary mutant distributions and evolutionary optimization. *Bulletin of Mathematical Biology*, 50:635–660, 1988.

[76] T. Stantcheva, P. Caselli, and E. Herbst. Modified rate equations revisited. a corrected treatment for diffusive reactions on grain surfaces. *A&A*, 375(2):673–679, 2001.

[77] T. Stantcheva and E. Herbst. Deuterium fractionation on interstellar grains studied with the direct master equation approach. *Mon. Not. R. Astron. Soc.*, 340(3):983–988, April 2003.

[78] T. Stantcheva, V. I. Shematovich, and E. Herbst. On the master equation approach to diffusive grain-surface chemistry: The H, O, CO system. *A&A*, 391:1069–1080, 2002.

[79] P. Tarazona. Error thresholds for molecular quasispecies as phase transitions: From simple landscapes to spin-glass models. *Phys. Rev. A*, 45:6038, 1992.

[80] C. J. Thompson and J. L. McBride. On Eigen's theory of the self-organization of matter and the evolution of biological macromolecules. *Mathematical Biosciences*, 21:127, 1974.

[81] A. G. G. M. Tielens. unpublished, 1995.

[82] A. G. G. M. Tielens and W. Hagen. Model calculations of the molecular composition of interstellar grain mantles. *A&A*, 114:245–260, October 1982.

[83] G. Vidali, J. Roser, G. Manicó, V. Pirronello, H. B. Perets, and O. Biham. Formation of molecular hydrogen on analogues of interstellar dust grains: experiments and modeling. *J. Phys.: Conf. Ser.*, 6:36–58, 2005.

[84] A. F. Voter. Introduction to the Kinetic Monte Carlo method. In Kurt E. Sickafus, Eugene A. Kotomin, and Blas P. Uberuaga, editors, *Radiation Effects in Solids*, volume 235 of *Nato Science Series II: Mathematics, Physics And Chemistry*. Springer, 2007.

[85] M C Whitlock, P. C. Phillips, F. B. Moore, and S. J. Tonsor. Multiple fitness peaks and epistasis. *Annual Review of Ecology and Systematics*, 26:601–629, November 1995.

[86] T. Wiehe. Model dependency of error thresholds: the role of fitness functions and contrasts between the finite and infinte sites models. *Genet. Res. Camb.*, 69:127–136, 1997.

[87] C. O. Wilke, J. L. Wang, C. Ofria, R. E. Lenski, and C. Adami. Evolution of digital organisms at high mutation rates leads to survival of the flattest. *Nature*, 412:331–333, 2001.

[88] A. Wolff and J. Krug. Robustness and epistasis in mutation-selection models. *Phys. Biol.*, 6:036007, 2009.

[89] A. Wolff, I. Lohmar, Y. Frank, J. Krug, and O. Biham. Diffusion-limited reactions on a two-dimensional lattice with binary disorder. *Phys. Rev. E*, 81:061109, 2010.

[90] A. Wolff, I. Lohmar, J. Krug, and O. Biham. Diffusion-limited reactions on a two-dimensional lattice with continuous distributions of binding energies. *J. Stat. Mech.*, P10029, 2011.

[91] S. Wright. The shifting balance theory and macroevolution. *Ann. Rev. Genet.*, 16:1, 1982.

Danksagung

Ganz besonders möchte ich mich bei meinem Doktorvater Prof. Dr. Joachim Krug für seine hervorragende Betreuung bedanken. Er hat diese Arbeit immer wieder mit Ideen und Ratschlägen vorangetrieben und hatte stets ein offenes Ohr für Fragen und Probleme.
Mein Dank geht an Prof. Dr. Johannes Berg, der bereitwillig die Aufgabe des Zweitgutachters übernommen hat.
Weiterhin bedanke ich mich bei Prof. Dr. Ofer Biham für sein Interesse an meiner Arbeit.
Mein herzlicher Dank geht an Ingo Lohmar für die produktive Zusammenarbeit und seine permanente Diskussionsbereitschaft.
Und nicht zuletzt möchte ich mich bei meinen Freunden und Kollegen, die durch ihre fachliche oder anderweitige Unterstützung direkt oder indirekt zur Entstehung dieser Dissertation beigetragen haben, bedanken.

Diese Arbeit wurde von der DFG im Rahmen des SFB/TR 12 und durch die Bonn-Cologne Graduate School of Physics and Astronomy unterstützt.

Erklärung

Ich versichere, dass ich die von mir vorgelegte Dissertation selbständig angefertigt, die benutzten Quellen und Hilfsmittel vollständig angegeben und die Stellen der Arbeit – einschließlich Tabellen, Karten und Abbildungen –, die anderen Werken im Wortlaut oder dem Sinn nach entnommen sind, in jedem Einzelfall als Entlehnung kenntlich gemacht habe; dass diese Dissertation noch keiner anderen Fakultät oder Universität zur Prüfung vorgelegen hat; dass sie – abgesehen von unten angegebenen Teilpublikationen – noch nicht veröffentlicht worden ist sowie, dass ich eine solche Veröffentlichung vor Abschluss des Promotionsverfahrens nicht vornehmen werde.
Die Bestimmungen der Promotionsordnung sind mir bekannt. Die von mir vorgelegte Dissertation ist von Herrn Prof. Dr. Joachim Krug betreut worden.

Teilpublikationen:

A. Wolff, J. Krug, Robustness and epistasis in mutation-selection-models, Physical Biology **6**, 036007, (2009)

A. Wolff, I. Lohmar, Y. Frank, J. Krug, O. Biham, Diffusion-limited reactions on a two-dimensional lattice with binary disorder, Phys. Rev. E **81**, 061109, (2010)

A. Wolff, I. Lohmar, J. Krug, O. Biham, Diffusion-limited reactions on disordered surfaces with continuous distributions of binding energies, J. Stat. Mech. **10**, P10029, (2011)